
Patient-specific bone marrow dosimetry in
Lu-177-based radionuclide therapy: investigation of
efficient data acquisition protocols and a clinical Monte
Carlo dosimetry workflow for 3D absorbed dose
modelling

Astrid Gosewisch



25.09.2019

Klinik und Poliklinik für Nuklearmedizin
der Ludwig-Maximilians-Universität München
Vorstand: Prof. Dr. med. Peter Bartenstein

Patient-specific bone marrow dosimetry in
Lu-177-based radionuclide therapy: investigation of
efficient data acquisition protocols and a clinical Monte
Carlo dosimetry workflow for 3D absorbed dose
modelling

Dissertation
zum Erwerb des Doktorgrades der Naturwissenschaften
an der Medizinischen Fakultät der
Ludwig-Maximilians-Universität zu München

vorgelegt von
Astrid Gosewisch
aus
Augsburg



2019

Mit Genehmigung der Medizinischen Fakultät
der Universität München

Betreuer:

PD Dr. rer. nat. Guido Böning

Zweitgutachter:

PD Dr. med. Dr. rer. nat. Christian Thieke

Dekan:

Prof. Dr. med. dent. Reinhard Hickel

Tag der mündlichen Prüfung:

06.04.2020

Eidesstattliche Versicherung

Gosewisch, Astrid

Ich erkläre hiermit an Eides statt,
dass ich die vorliegende Dissertation mit dem Titel

Patient-specific bone marrow dosimetry in Lu-177-based radionuclide therapy: investigation of efficient data acquisition protocols and a clinical Monte Carlo dosimetry workflow for 3D absorbed dose modelling

selbständig verfasst, mich außer der angegebenen keiner weiteren Hilfsmittel bedient und alle Erkenntnisse, die aus dem Schrifttum ganz oder annähernd übernommen sind, als solche kenntlich gemacht und nach ihrer Herkunft unter Bezeichnung der Fundstelle einzeln nachgewiesen habe.

Ich erkläre des Weiteren, dass die hier vorgelegte Dissertation nicht in gleicher oder in ähnlicher Form bei einer anderen Stelle zur Erlangung eines akademischen Grades eingereicht wurde.

Astrid Gosewisch

München, 25.09.2019

List of publications

The following publications underlie the presented cumulative dissertation, in agreement with the promotion regulation for natural sciences of the medical faculty of the Ludwig-Maximilians-University Munich.

A. Gosewisch, A. Delker, S. Tattenberg, H. Ilhan, A. Todica, J. Brosch, L. Vomacka, A. Brunegraf, F. J. Gildehaus, S. Ziegler, P. Bartenstein, and G. Böning. "Patient-specific image-based bone marrow dosimetry in Lu-177-[DOTA0, Tyr3]-Octreotate and Lu-177-DKFZ-PSMA-617 therapy: investigation of a new hybrid image approach". In: *EJNMMI research* 8.1 (2018), p. 76

A. Gosewisch, H. Ilhan, S. Tattenberg, A. Mairani, K. Parodi, J. Brosch, L. Kaiser, F. J. Gildehaus, A. Todica, S. Ziegler, P. Bartenstein, and G. Böning. "3D Monte Carlo bone marrow dosimetry for Lu-177-PSMA therapy with guidance of non-invasive 3D localization of active bone marrow via Tc-99m-anti-granulocyte antibody SPECT/CT". in: *EJNMMI research* 9.1 (2019), p. 76

Conference abstracts

All investigations of this thesis were additionally presented on national and international conferences.

A. Gosewisch, A. Delker, L. Vomacka, W. Fendler, A. Brunegraf, F. J. Gildehaus, A. Mairani, K. Parodi, P. Bartenstein, and G. Böning. "Estimation of local photon dose to active bone marrow in Lu-177 PSMA PRRT therapy using patient-specific Monte Carlo simulations". In: *European journal of nuclear medicine and molecular imaging* 42.Suppl. 1 (2015)

A. Gosewisch, A. Delker, L. Vomacka, W. Fendler, A. Brunegraf, F. J. Gildehaus, F. Botta, A. Mairani, K. Parodi, P. Bartenstein, and G. Böning. "Monte Carlo basierte Risikoabschätzung der Photonendosis auf das aktive Knochenmark bei der Lu-177-DKFZ-PSMA-617 Therapie". In: *Nuklearmedizin* 55.02 (2016)

A. Gosewisch, A. Delker, S. Tattenberg, L. Vomacka, A. Brunegraf, F. J. Gildehaus, P. Bartenstein, and G. Böning. "Investigation of a hybrid image approach and a reduction in the number of blood samples for a decreased clinical workload for patient-specific bone marrow dosimetry in Lu-177-DKFZ-PSMA-617 therapy". In: *European journal of nuclear medicine and molecular imaging* 43.Suppl. 1 (2016)

A. Gosewisch, A. Delker, S. Tattenberg, L. Vomacka, H. Ilhan, F. J. Gildehaus, A. Brunegraf, P. Bartenstein, and G. Böning. "Entwurf eines effizienten Messprotokolls zur patienten-spezifischen Knochenmarksdosimetrie in der Lu-177-PSMA-DKFZ-617 Therapie". In: *Nuklearmedizin* 56.02 (2017)

A. Gosewisch, L. Ermoschkin, H. Ilhan, A. Todica, L. Vomacka, P. Bartenstein, and G. Böning. "Patient-specific pharmacokinetics and dosimetry over multiple therapy cycles during Lu-177-based radionuclide therapy: a study for Lu-177-DOTATATE and Lu-177-PSMA". in: *European journal of nuclear*

medicine and molecular imaging 44.Suppl. 2 (2017)

A. Gosewisch, L. Ermoschkin, H. Ilhan, A. Todica, L. Vomacka, P. Bartenstein, and G. Böning. "Patienten-Spezifische Pharmakokinetik und Dosimetrie über multiple Therapiezyklen bei der Lu-177-PSMA oder Lu-177-DOTATATE Radionuklidtherapie". In: *Nuklearmedizin* 57.02 (2018)

A. Gosewisch, H. Ilhan, C. Zach, A. Todica, J. Brosch, L. Vomacka, P. Bartenstein, and G. Böning. "Relevance of kidneys and bone marrow as dose-limiting organs during Lu-177-PSMA-DKFZ-617 therapy for patients with high bone tumor burden". In: *European journal of nuclear medicine and molecular imaging* 45.Suppl. 1 (2018)

A. Gosewisch, M. Cachovan, H. Ilhan, P. Bartenstein, A. H. Vija, and G. Boening. "Investigation of the effect of patient motion onto 3D dose estimates in Lu-177-PSMA therapy using Siemens xSPECT Quant reconstruction with integrated motion correction and Dosimetry Research Tool". In: *European journal of nuclear medicine and molecular imaging* 45.Suppl. 1 (2018)

A. Gosewisch, H. Ilhan, C. Zach, J. Brosch, L. Kaiser, A. Todica, P. Bartenstein, and G. Böning. "Relevanz von Nieren und Knochenmark als Risikoorgane bei der Lu-177-PSMA Therapie für Patienten mit hoher Tumorlast". In: *Nuklearmedizin* 58.02 (2019)

A. Gosewisch, M. Cachovan, H. Ilhan, P. Bartenstein, A. H. Vija, and G. Böning. "Untersuchung des Effekts von Patientenbewegung auf die 3D Dosimetrie für die Lu-177-PSMA Therapie mittels Siemens xSPECT Quant mit integrierter Bewegungskorrektur sowie Siemens Dosimetry Research Tool". In: *Nuklearmedizin* 58.02 (2019)

A. Gosewisch, H. Ilhan, A. Todica, J. Brosch, L. Kaiser, P. Bartenstein, and G. Boening. "The role of kidneys and bone marrow as critical organs during Lu-177-PSMA-DKFZ-617 therapy depending on the patient-specific tumor load". In: *Journal of Nuclear Medicine* 60.supplement 1 (2019)

Other related publications

Further publications relevant to the overall topic of this thesis are listed below.

A. Delker, W. P. Fendler, C. Kratochwil, A. Brunegraf, A. Gosewisch, F. J. Gildehaus, S. Tritschler, C. G. Stief, K. Kopka, U. Haberkorn, P. Bartenstein, and G. Böning. "Dosimetry for 177 Lu-DKFZ-PSMA-617: a new radiopharmaceutical for the treatment of metastatic prostate cancer". In: *European journal of nuclear medicine and molecular imaging* 43.1 (2016), pp. 42–51

A. Gosewisch, H. Ilhan, L. Vomacka, and G. Böning. "Dosimetrie bei der Radionuklidtherapie mit Lu-177". In: *Der Nuklearmediziner* 41.01 (2018), pp. 69–80

L. Fiedler, M. Kellner, A. Gosewisch, R. Oos, G. Böning, S. Lindner, N. Albert, P. Bartenstein, H.-J. Reulen, R. Zeidler, and F. J. Gildehaus. "Evaluation of 177Lu[Lu]-CHX-A-DTPA-6A10 Fab as a radioimmunotherapy agent targeting carbonic anhydrase XII". in: *Nuclear medicine and biology* 60 (2018), pp. 55–62

H.-J. Reulen, E. S. Molina, R. Zeidler, F. J. Gildehaus, G. Böning, A. Gosewisch, and W. Stummer. "Intracavitary radioimmunotherapy of high-grade gliomas: present status and future developments". In: *Acta neurochirurgica* 161.6 (2019), pp. 1109–1124

S. Rudisile, A. Gosewisch, V. Wenter, M. Unterrainer, G. Böning, F. J. Gildehaus, W. P. Fendler, C. J. Auernhammer, C. Spitzweg, P. Bartenstein, A. Todica, and H. Ilhan. "Salvage PRRT with 177 Lu-DOTA-octreotate in extensively pretreated patients with metastatic neuroendocrine tumor (NET): dosimetry, toxicity, efficacy, and survival". In: *BMC cancer* 19.1 (2019), pp. 1–9

H. Ilhan, A. Todica, S. Lindner, G. Boening, A. Gosewisch, C. Wängler, B. Wängler, R. Schirmacher, and P. Bartenstein. "First-in-human 18 F-SiFAlin-TATE PET/CT for NET imaging and theranostics". In: *European journal of nuclear medicine and molecular imaging* (2019), pp. 1–2

Other related conference abstracts

Further conference abstracts relevant to the overall topic of this thesis are listed below.

A. Delker, A. Gosewisch, S. Rieger, H. Ilhan, W. Fendler, F. Gildehaus, P. Bartenstein, and G. Boening. "Dosimetry for Lu-177-PSMA therapy of patients with mCRPC: A comparison of 3D SPECT and 2D planar methods". In: *European Journal of Nuclear Medicine and Molecular Imaging* 43.Suppl. 1 (2016)

L. Vomacka, A. Delker, A. Gosewisch, W. Fendler, F. J. Gildehaus, A. Brunegraf, P. Bartenstein, and G. Böning. "Automatic image segmentation for efficient 3D dosimetry with reduced influence of registration-errors and noise in Lu-177 DKFZ- PSMA-617 therapy using a robust cluster algorithm on sequential SPECT data and subsequent voxel-wise re-scaling". In: *European journal of nuclear medicine and molecular imaging* 43.Suppl. 1 (2016)

L. Vomacka, A. Delker, A. Gosewisch, W. Fendler, P. Bartenstein, and G. Boening. "Automatische Bildsegmentierung für die 3D Dosimetrie unter Verwendung eines robusten Cluster Algorithmus auf 4D SPECT Daten bei der Therapie von Patienten mit kastrationsresistentem metastasierten Prostatakarzinom mit Lu-177 DKFZ-PSMA-617". In: *Nuklearmedizin* 55.02 (2016)

L. Vomacka, A. Gosewisch, A. Delker, W. Fendler, P. Bartenstein, and G. Boening. "Automatic image segmentation for 3D dosimetry in Lu-177 DKFZ-PSMA-617 therapy of castrate-resistant metastatic prostate cancer using a robust cluster algorithm on 4D SPECT data". In: *Journal of Nuclear Medicine* 57.supplement 2 (2016)

A. Delker, A. Gosewisch, S. Rieger, H. Ilhan, W. Fendler, F. J. Gildehaus, P. Bartenstein, and G. Böning. "Dosimetrie bei der Lu-177-PSMA Therapie von Patienten mit metastasiertem kastrationsresistentem Prostatakarzinom: Ein Vergleich von 3D SPECT und 2D planaren Szintigraphien". In: *Nuklearmedizin* 56.02 (2017)

L. Fiedler, M. Kellner, A. Gosewisch, G. Böning, S. Lindner, P. Bartenstein, R. Zeidler, and F. Gildehaus. "Evaluation of Lu-177 Labelled 6A10 Fab as Carbonic Anhydrase 12 Targeting Agent". In: *European journal of nuclear medicine and molecular imaging* 44.Suppl. 2 (2017)

J. F. Brosch, A. Gosewisch, A. Delker, L. Vomacka, P. Bartenstein, A. Todica, H. Ilhan, and G. Boening.

“Investigation of a simplified quantitative yttrium-90 bremsstrahlung SPECT reconstruction by usage of background compensation and patient-specific calibration factors for yttrium-90 SIRT dosimetry”. In: *European journal of nuclear medicine and molecular imaging* 45.Suppl. 1 (2018)

J. F. Brosch, A. Gosewisch, A. Delker, L. Vomacka, P. Bartenstein, H. Ilhan, A. Todica, and G. Boening. “Comparison of a simplified quantitative yttrium-90 bremsstrahlung SPECT reconstruction with yttrium-90 PET in terms of quantification for dosimetry of SIR-therapy in the liver”. In: *European journal of nuclear medicine and molecular imaging* 45.Suppl. 1 (2018)

S. Rudisile, A. Gosewisch, F. J. Gildehaus, G. Boening, C. Auernhammer, P. Bartenstein, A. Todica, and H. Ilhan. “Effectivity and Toxicity of Salvage PRRT with Lu-177 DOTATATE in patients with progressive, metastasized NET”. in: *Journal of Nuclear Medicine* 59.supplement 1 (2018)

H. von Zimmermann, A. Gosewisch, J. Brosch, L. Kaiser, C. Zach, F. J. Gildehaus, P. Bartenstein, and G. Böning. “Einfluss von Läsionsgröße und Tumor-zu Hintergrundverhältnis auf die quantitative Lutetium-177 SPECT Bildgebung für die Dosimetrie”. In: *Nuklearmedizin* 58.02 (2019)

J. Brosch, A. Gosewisch, H. von Zimmermann, L. Kaiser, P. Barstenstein, A. Todica, H. Ilhan, and G. Böning. “Evaluation von Yttrium-90-PET und Yttrium-90-SPECT Phantommessungen angepasst an Messbedingungen von 20 SIRT Patienten”. In: *Nuklearmedizin* 58.02 (2019)

J. Brosch, A. Gosewisch, L. Kaiser, P. Bartenstein, H. Ilhan, A. Todica, and G. Boening. “3D image-based dosimetry for Yttrium-90 SIR-therapy of HCC: comparison of three different techniques”. In: *Journal of Nuclear Medicine* 60.supplement 1 (2019)

Contents

Eidesstattliche Versicherung	v
List of publications	vii
Contents	xii
Nomenclature	xiii
Abstract	xv
Zusammenfassung	xvii
1 Introduction to radionuclide therapy	1
2 Basics of nuclear medicine imaging and internal dosimetry	5
2.1 Nuclear medicine imaging devices	5
2.1.1 Basics of Lutetium-177 imaging for internal dosimetry	5
2.1.2 Gamma camera imaging	6
2.1.3 Image-degrading effects	6
2.1.4 SPECT reconstruction	8
2.1.5 Quantitative imaging	9
2.1.5.1 SPECT attenuation correction	10
2.1.5.2 SPECT scatter correction	10
2.1.5.3 SPECT collimator-detector-response compensation	11
2.1.5.4 SPECT calibration	11
2.1.5.5 Accuracy of SPECT quantification	12
2.1.5.6 Planar image quantification and comparison to quantitative SPECT	13
2.1.6 Positron-Emission-Tomography	14
2.2 Internal Dosimetry	15
2.2.1 MIRD scheme	15
2.2.2 Patient-specific 3D internal dosimetry	16
2.2.3 State-of-the-art bone marrow dosimetry	18
3 Studies	21
3.1 Motivation and objectives of this thesis	21
3.2 Objective 1	22
3.2.1 Preceding investigation of the feasibility of single-SPECT kidney and lesion dosimetry	22
3.2.2 Studies on an efficient data acquisition for clinical bone marrow internal dosimetry	25
3.3 Objective 2	28
3.3.1 Preceding study on the relevance of kidneys and bone marrow for high-lesion load mCRPC patients	28
3.3.2 Investigation of a clinical 3D Monte-Carlo-based bone marrow dosimetry workflow	30

4 Discussion & outlook	35
Bibliography	51
List of Figures	54
List of Tables	55
5 Original publication 1	57
6 Original publication 2	75
Danksagung	91

Nomenclature

CT	Computed-Tomography
CDR	Collimator-detector-response
F-18	Fluor-18
Ga-68	Gallium-68
ID	Internal dosimetry
Lu-177	Lutetium-177
mCRPC	Metastasized castration-resistant prostate cancer
MAP	Maximum-a-posteriori
MIP	Maximum-intensity-projection
MIRD	Medical-Internal-Radiation-Dose
MLEM	Maximum-likelihood-expectation-maximization
NET	Neuroendocrine tumor
OAR	Organ(s)-at-risk
OSEM	Ordered-subset-expectation-maximization
PET	Positron-Emission-Tomography
p. i.	Post injection (i. e. post end of injection)
PRRT	Peptide-receptor-radionuclide-therapy
PSMA	Prostate-specific-membrane-antigene
RC	Recovery
ROB	Remainder-of-the-body
RT	Radionuclide therapy
SPECT	Single-Photon-Emission-Computed-Tomography
sstr	Somatostatin-receptor
TAC	Time-activity-curve
Tc-99m	Technetium-99m
VOI	Volume(s)-of-interest

Abstract

Aim: Internal dosimetry is recommended during radionuclide therapy to primarily avoid toxicity of organs-at-risk (OAR). State-of-the-art internal dosimetry is simplistic and based on tabulated absorbed dose conversion factors (S-values), while sequential quantitative imaging is the preferred method to determine the patient-specific time-activity-curve (TAC) in OAR and lesions. The hematologically active bone marrow is an important OAR during Lu-177-PRRT of advanced neuroendocrine tumors (NET), and Lu-177-PSMA therapy of metastasized castration-resistant prostate cancer (mCRPC). While for non-marrow OAR and lesions sequential quantitative SPECT imaging is advisable, classical bone marrow dosimetry requires additional sequential whole-body planar imaging in combination with excreta collection, and blood sampling to derive the TAC in all relevant accumulating regions. These multiple examinations cause a large patient burden and a high clinical workload, which limits routine bone marrow dosimetry in clinical practice. On the other hand, classical S-value dosimetry was initially developed regarding organ dosimetry during daily radiation protection, and thus includes only a very simplified lesion concept. The applicability of S-value bone marrow dosimetry is limited particularly for mCRPC patients, who usually present with excessive skeletal metastases, and as skeletal radiopharmaceutical uptake can cause a substantial bone marrow cross-irradiation. Skeletal metastases can further initiate bone marrow displacement processes, which cannot be handled via tabulated S-values. Starting from these limitations, the aim of this thesis was to optimize clinical bone marrow dosimetry. In a first step, an efficient and patient-friendly measurement scheme for routine bone marrow internal dosimetry was defined. The overall dosimetry scheme aims to allow for SPECT-based dosimetry for lesions and non-marrow OAR, and bone marrow dosimetry within a clinically acceptable uncertainty. Further, a clinical Monte-Carlo-based internal dosimetry workflow was established, to in particular provide an improved patient-specific concept regarding bone marrow dosimetry for mCRPC patients with high skeletal lesion load.

Material & methods: In a preceding study, a TAC model for efficient single-SPECT kidney and lesion dosimetry applicable to selected therapy cycles was investigated. This single-SPECT TAC model was then extended to allow for bone marrow dosimetry via single whole-body planar and sequential abdominal SPECT imaging. This hybrid SPECT-planar model is based on a function decaying mono-exponentially with the effective wash-out of the abdominal activity, scaled with a single uptake measurement at either 24, 48, or 72 h post infusion. Further, for a sub-cohort of patients, SPECT-based whole-body planar image calibration was compared to classical net-activity calibration to skip the need for patient excreta counting. A clinically feasible blood sampling scheme based on five blood probes was developed, using the identical sub-cohort of patients with available extended blood sampling at 20, 30, 40, 60, and 80 min and 24, 48, and 72 h post start of infusion.

For 14 mCRPC patients (3.7-6 GBq Lu-177-DKFZ-PSMA-617) the relevance of the kidneys, representing an important non-marrow OAR, and of the active bone marrow was studied in dependence upon the patient-specific skeletal lesion load. Conventional S-value-based dosimetry was used, in combination with sequential abdominal SPECT imaging, and the optimized bone marrow measurement protocol.

Based on these preceding results, a template-based Monte Carlo bone marrow dosimetry workflow was developed and applied to 11 mCRPC patients of varying bone lesion load. The patient-specific information from pre-therapeutic Ga-68-PSMA-11 PET/CT whole-body imaging and therapeutic Lu-177 quantitative TAC measurements was condensed into a patient-specific accumulation template, including full consideration of the 3D lesion distribution. A weighting-based model was implemented into the FLUKA Monte Carlo code to simulate the absorbed dose deposition solely within the active bone marrow. Different models regarding active bone marrow localization were investigated, i. e. without and with complete bone marrow displacement by PSMA-avid lesions (methods MC1 and MC2), and with usage of exemplarily performed patient-specific active bone marrow localization via Tc-99m-anti-granulocyte SPECT/CT. These Monte-Carlo-based results were further compared to the respective values from classical S-value dosimetry (SMIRD), and all absorbed doses were evaluated with regard to the course of blood element counts.

Results: Single-SPECT dosimetry for both, lesions and kidneys, was found to be feasible, particularly if SPECT imaging is performed at 72 h post infusion. Mean deviations compared to sequential SPECT imaging were found to be below 10 % for Lu-177-PRRT and Lu-177-PSMA therapy. Similarly, bone marrow dosimetry based on single whole-body planar imaging at 72 h p. i. showed the smallest differences compared to sequential imaging, i. e. on average 2 ± 2 % and 3 ± 2 % for Lu-177-PRRT and Lu-177-PSMA therapy, respectively. The proposed hybrid SPECT-planar bone marrow protocol includes SPECT-based whole-body planar image calibration and blood sampling at 20 and 60 min, and at 24, 48, and 72 h post infusion. Both methods showed an average deviation of 5.7 ± 4.8 % and 5.0 ± 5.6 % compared to the reference.

Regarding Lu-177-PSMA therapy, increasing bone marrow absorbed doses were verified with increasing skeletal lesion load ($r=0.8$, $p<0.05$), while a significant opposite trend was observed for the kidney absorbed dose ($r=-0.9$, $p<0.05$). These results indicate that the active bone marrow is the relevant OAR for high-lesion-load mCRPC patients, with initial S-value dosimetry resulting in an average absorbed dose of 16 ± 10 mGy/GBq (range: 6-36 mGy/GBq). Patient-specific 3D Monte Carlo bone marrow dosimetry yielded on median 17-fold to four-fold higher bone marrow absorbed doses (median: MC1: 130 mGy/GBq; MC2: 37 mGy/GBq; SMIRD: 11 mGy/GBq). Image-based active bone marrow localization as available for two mCRPC patients resulted in intermediate absorbed doses between MC1 and MC2 (approximately 40 % reduction with respect to MC1). A preliminary correlation with nadir-to-baseline ratios of blood element counts resulted in a significant correlation with the course of platelet counts for all models, while highest correlation was obtained for MC2 ($r=-0.7$).

Conclusion: Optimization of quantitative measurements for bone marrow dosimetry is feasible within uncertainties of 5-10 %, which are well acceptable regarding the overall uncertainty of state-of-the-art bone marrow internal dosimetry. These deviations might be further well acceptable for non-risk patients, i. e. low-lesion-load mCRPC patients and NET patients. By contrast, for high-lesion-load mCRPC patients critical bone marrow absorbed doses should be expected, and patient-specific 3D Monte-Carlo-based bone marrow dosimetry in combination with image-based active bone marrow localization is advisable to obtain realistic absolute values. Future studies shall aim at further identifying all relevant hematological risk factors, which is a main step to make bone marrow dosimetry predictive for hematological toxicities and to appropriately stratify risk patients.

Zusammenfassung

Zielsetzung: Die Dosimetrie ist ein elementarer Bestandteil der Radionuklidtherapie, um speziell die Strahlenbelastung der Therapie-typischen Risikoorgane möglichst niedrig zu halten. Derzeit erfolgt die Dosimetrie in der Radionuklidtherapie mittels einfachen und vorberechneten Dosiskonversionsfaktoren (S-Werte), wobei die Bestimmung der Patienten-spezifischen Zeit-Aktivitäts-Kurven (TAC) in Risikoorganen und Läsionen vorzugsweise mittels sequenzieller quantitativer Bildgebung erfolgt. Das blutbildende Knochenmark ist ein bedeutendes Risikoorgan, sowohl in der Lu-177-PRRT des fortgeschrittenen Neuroendokrinen Tumors (NET), als auch in der Lu-177-PSMA Therapie des metastasierten kastrations-resistenten Prostatakarzinoms (mCRPC). Während für eine robuste Dosimetrie in Risikoorganen und Läsionen in der Regel die sequenzielle SPECT-Bildgebung zu empfehlen ist, erfordert die Knochenmarksdosimetrie derzeit eine zusätzliche sequenzielle Ganzkörperbildgebung, samt Bestimmung der ausgeschiedenen Aktivitätsmenge, sowie mehrfache Blutentnahmen, um die TAC aller relevant anreichernden Körperregionen zu ermitteln. Diese Vielzahl an Untersuchungen führt zu einer hohen Patientenbelastung und klinischen Auslastung, und limitiert folglich die regelmäßige Knochenmarksdosimetrie im klinischen Alltag. Da die S-Wert-basierte Dosimetrie zudem zur Organdosimetrie im alltäglichen Strahlenschutz entwickelt wurde, besteht nur ein sehr vereinfachtes Konzept zur Berücksichtigung von Tumoren. Die Aussagekraft der S-Wert-basierten Dosimetrie ist folglich besonders hinsichtlich Prostatakarzinom-Patienten limitiert, da diese oftmals eine ausgeprägte Skelettmetastasierung zeigen, deren Aktivitätsanreicherung eine signifikante Bestrahlung des umliegenden aktiven Knochenmarks verursachen kann. Eine vorhandene Skelettmetastasierung kann zudem eine Verdrängung des aktiven Knochenmarks auslösen, die jedoch nicht mittels vorberechneten S-Werten berücksichtigt werden kann.

Ausgehend von dieser Situation lag die Zielsetzung dieser Arbeit in der Optimierung der klinischen Knochenmarksdosimetrie. Zunächst wurde ein effizientes und patientenfreundliches Messschema entwickelt, um die routinemäßige Knochenmarksdosimetrie im klinischen Alltag zu ermöglichen. Speziell soll eine Knochenmarksdosimetrie mit ausreichender Genauigkeit, als auch eine SPECT-basierte Dosimetrie von Tumoren und weiteren Risikoorganen verfügbar sein. Im zweiten Schritt wurde eine klinisch anwendbare Monte-Carlo-basierte Knochenmarksdosimetrie entwickelt, um speziell für Prostatakarzinom-Patienten mit ausgeprägter Skelettmetastasierung eine verbesserte Berücksichtigung der Patienten-spezifischen Gegebenheiten zu gewährleisten.

Material & Methoden: In einer Vorstudie wurde ein TAC-Modell zur Tumor- und Nierendosimetrie mittels eines SPECT-Zeitpunkts im Hinblick auf ausgewählte Therapiezyklen entwickelt. Dieses Einzelzeitpunktmodell wurde im weiteren Verlauf zur Knochenmarksdosimetrie mittels einer einzelnen Ganzkörperbildgebung und einer sequenziellen SPECT-Bildgebung des Abdomens erweitert. Das genannte Hybridmodell skaliert im Speziellen die als mono-exponentiell angenommene effektive Aktivitätsabnahme im Abdomen mit der Ganzkörperanreicherung 24, 48 oder 72 h nach Injektion. Für eine Subkohorte an Patienten wurde zudem eine SPECT-basierte Kalibration der Ganzkörperbildgebung mit dem bisherigen Verfahren basierend auf Messung der Aktivitätsausscheidungen verglichen.

Zudem wurde ein klinisch anwendbares Schema zur Blutentnahme entwickelt, basierend auf der selbigen Patientenkohorte, für die eine Vielzahl an Blutentnahmen zu den Zeitpunkten 20, 30, 40, 60 und 80 Minuten, sowie 24, 48 und 72 h nach Injektion verfügbar war.

Für 14 Prostatakarzinom-Patienten (3.7-6 GBq Lu-177-DKFZ-PSMA-617) wurde im Weiteren die Relevanz des Knochenmarks, sowie der Nieren als bedeutendes weiteres Risikoorgan untersucht, im Hinblick auf die Abhängigkeit der absorbierten Dosen von der Patienten-spezifischen Knochentumorlast. Die Dosimetrie erfolgte dabei S-Wert-basiert, sowie unter Verwendung einer sequenziellen SPECT-Bildgebung und des optimierten Messschemas zur Knochenmarksdosimetrie. Basierend auf den Ergebnissen dieser Vorstudie wurde ein Template- und Monte-Carlo-basiertes Verfahren zur Knochenmarksdosimetrie entwickelt, sowie auf 11 Prostatakarzinom-Patienten angewendet. Alle Patientengegebenheiten der prä-therapeutischen Ga-68-PSMA-11 PET/CT Diagnostik, als auch der therapeutischen Messungen der Lu-177-Anreicherung wurden dabei zu einem Template des Patienten-spezifischen Anreicherungsmusters kombiniert, das die 3D Verteilung der Tumorlast vollständig berücksichtigt. Die Simulation der Dosisdeposition speziell im aktiven Knochenmark erfolgte mittels FLUKA, sowie einem implementierten Gewichtungsmodell. Die Simulationsstudie beinhaltete verschiedene Modelle zur aktiven Knochenmarksverteilung: keine als auch die komplette Verdrängung des aktiven Knochenmarks durch PSMA-exprimierende Tumoren (Methoden MC1 und MC2), sowie die Bild-basierte Knochenmarkslokalisation mittels Tc-99m-Anti-Granulozyten SPECT/CT. Ergebnisse der Monte Carlo und S-Wert (SMIRD) Knochenmarksdosimetrie wurden miteinander verglichen und hinsichtlich des Verlaufs der Blutparameter beurteilt.

Ergebnisse: Sowohl für die Lu-177-PRRT als auch für die Lu-177-PSMA Therapie erwies sich die Nieren- und Tumordosimetrie mittels eines SPECT-Zeitpunkts als möglich, insbesondere unter Verwendung eines späten Messpunktes 72 h nach Injektion. Dabei ergab sich eine mittlere Abweichung von weniger als 10 % im Vergleich zur sequenziellen Bildgebung. Ebenfalls zeigte die Knochenmarksdosimetrie basierend auf einer einzelnen Ganzkörperszintigrafie 72 h nach Injektion die geringste Abweichung zur sequenziellen Bildgebung, sowohl für die Lu-177-PRRT ($2 \pm 2 \%$), als auch für die Lu-177-PSMA Therapie ($3 \pm 2 \%$). Das entwickelte Hybridmodell wurde mit einer SPECT-basierten Kalibration kombiniert, als auch mit einem Blutentnahmeschema 20 und 60 Minuten, sowie 24, 48 und 72 h nach Injektion. Für beide Methoden ergab sich eine Abweichung von $5.7 \pm 4.8 \%$ und $5.0 \pm 5.6 \%$ zur Referenz.

Im Hinblick auf die Lu-177-PSMA Therapie zeigte sich eine Zunahme der absorbierten Knochenmarksdosis mit steigender Tumormasse im Skelett ($r=0.8$, $p<0.05$), während die absorbierte Nierendosis einen gegensätzlichen Trend aufwies ($r=-0.9$, $p<0.05$). Diese Ergebnisse bestätigen das aktive Knochenmark als relevantes Risikoorgan für Prostatakarzinom-Patienten mit hoher Knochentumorlast. Die mittlere S-Wert-basierte absorbierte Knochenmarksdosis ergab sich dabei zu 16 ± 10 mGy/GBq (6-36 mGy/GBq). Eine weitergehende Monte-Carlo-basierte Patienten-spezifische 3D Knochenmarksdosimetrie ergab um 17-fach, sowie vierfach erhöhte absorbierte Knochenmarksdosen (Median: MC1: 130 mGy/GBq; MC2: 37 mGy/GBq; SMIRD: 11 mGy/GBq). Die Bild-basierte Lokalisation des aktiven Knochenmarks ergab beispielhaft für zwei Patienten eine Reduktion der absorbierten Dosis um 40 % im Vergleich zu MC1, resultierte jedoch in höhere Werte als MC2. Eine erste Korrelation der Knochenmarksdosimetrie mit dem Verlauf der Blutparameter zeigte eine signifikante Korrelation mit der Thrombozytenabnahme für alle Modelle, während die stärkste Korrelation für MC2 beobachtet wurde ($r=-0.7$).

Schlussfolgerung: Eine Optimierung der Knochenmarksdosimetrie ist im Rahmen einer Unsicherheit von 5-10 % möglich, die besonders im Hinblick auf die generelle Unsicherheit der Knochenmarksdosimetrie akzeptabel ist. Hierbei erlaubt das entwickelte Hybridmodell eine effiziente Knochenmarkdosime-

trie für Prostatakarzinom-Patienten mit niedriger Knochentumorlast, sowie NET-Patienten. Im Gegensatz dazu sollte die Knochenmarksdosimetrie für Prostatakarzinom-Patienten mit hoher Tumorlast um eine Patienten-spezifische 3D Monte Carlo Dosimetrie unter Verwendung einer Bild-basierten Knochenmarkslokalisation erweitert werden, um realistische Absolutwerte zu erhalten. In weiterführenden Studien sollen relevante hämatologische Risikofaktoren identifiziert werden, um die Vorhersagbarkeit der Knochenmarksdosimetrie hinsichtlich des Therapieverlaufs zu verbessern, sowie um eine angemessene Stratifizierung von Risikopatienten zu ermöglichen.

1 | Introduction to radionuclide therapy

Over the past decades, radionuclide therapy (RT) evolved as a promising therapy approach for progressed or inoperable cancer disease. Beginning with radio-iodine therapy for benign or malignant thyroid disease approximately 70 years ago [18, 93, 96], in the meanwhile more and more radiopharmaceuticals were investigated and introduced for nuclear medicine therapy. Glass or resin microspheres labelled with Yttrium-90 evolved as promising option for metastatic liver disease [77, 103, 111], while Lutetium-177-labelled compounds (Lu-177) were extensively studied for the treatment of inoperable or metastasized neuroendocrine tumors (NET) (peptide-receptor-radionuclide-therapy (PRRT) via, e. g., Lu-177-[DOTA0,Tyr3]-Octreotate) [122], or metastasized castration-resistant prostate cancer (mCRPC) (e. g. Lu-177-DKFZ-PSMA-617 or Lu77-PSMA-I&T) [9, 40, 101, 102] (Figure 1.1). In the last years, common radiopharmaceuticals have been more and more used in combination with Actinium-225, to benefit from the superior biological and thus therapeutical effectiveness of alpha particle emitters [25, 80]. Radium-223-dichloride therapy (Alpharadin) is a possible option regarding the treatment of skeletal metastases [97].

To ensure a safe and efficient therapy, the radiopharmaceutical has to be trapped within the malignant tissue. Therefore, the radiopharmaceutical can be either manually delivered in close proximity to the tumor cells (e. g. delivery via catheters into the tumor blood supply during Yttrium-90 therapy of liver metastases), or transported to the tumor cells via molecular processes (e. g. bone metabolism during Alpharadin therapy). Most of the radiopharmaceuticals make use of carrier molecules, specifically designed to target binding sites which are ideally solely located on, but at least overexpressed by the tumor cells. For example, Lu-177-PRRT is designed to target somatostatine receptors (sstr) typically expressed by NET cells, while Lu-177-DKFZ-PSMA-617 or Lu-177-PSMA-I&T bind to the prostate-specific membrane antigene (PSMA), located predominantly on mCRPC cells. Further, diagnostic Gallium-68-, Fluor-18-, or Technetium-99m-labelled compounds targeting sstr-expression or PSMA were developed, to allow for pre-therapeutic disease staging and for monitoring of the therapy effect via Positron-Emission-Tomography (PET) or Single-Photon-Emission-Computed-Tomography (SPECT) within a theranostic concept (Figure 1.1) [1, 2, 8, 73, 74, 81].

After injection into the blood stream, carrier-based radiopharmaceuticals distribute in the patient body over time according to the patient-specific and compound-dependent pharmacokinetic. Besides the desired uptake in malignant tissues, a compound accumulation is commonly also observed for organs-at-risk (OAR), which either express respective binding sites, or which are affected via excretion or other metabolic mechanisms. This non-target uptake leads to an undesired radiation effect to healthy tissues. Further, the active bone marrow is a standard OAR during RT due to its severe relevance for the hematological system, pronounced radiation sensitivity, and as it can be exposed to radiation in multiple ways (e. g. blood activity circulation) [70]. For Lu-177-PRRT, liver, spleen, kidneys, and the pituitary gland show normal tissue uptake, while the kidneys and hematological active bone marrow are considered as most important OAR [65, 110]. For Lu-177-PSMA therapy, kidneys and the active bone marrow likewise represent the relevant OAR, in combination with the PSMA-positive salivary glands, lacrimal glands, and intestine [33, 40] (Figure 1.2). Thus, patient-specific dosimetry is highly recommended to in

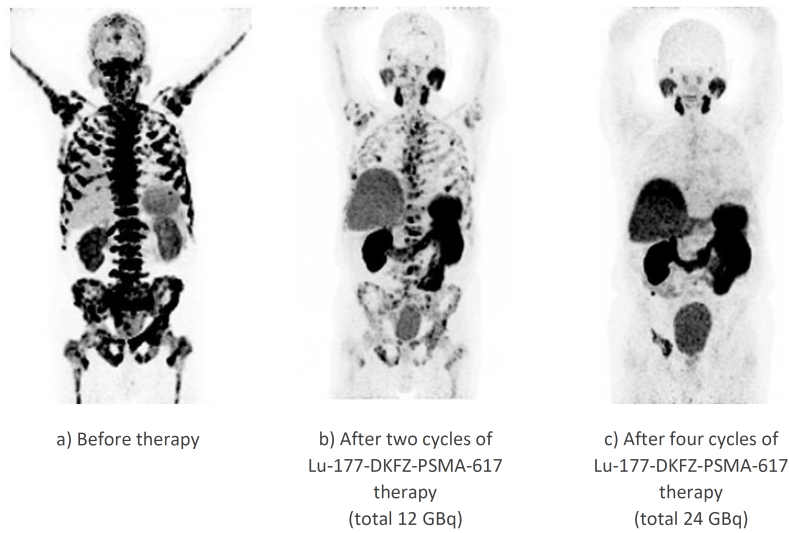


Figure 1.1: Response to Lu-177-DKFZ-PSMA-617 therapy shown for an exemplary mCRPC patient, as evaluated via Ga-68-PSMA-11 PET/CT (maximum-intensity projection (MIP)).

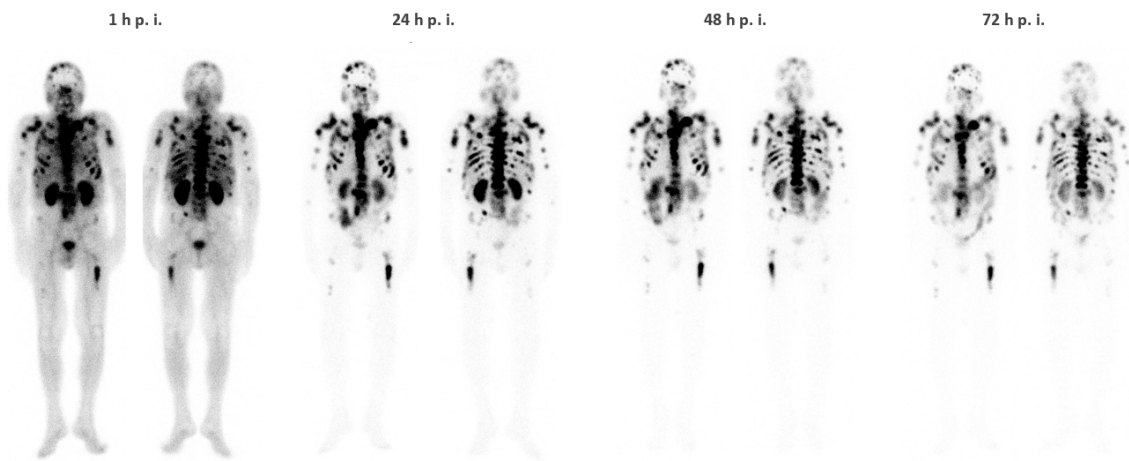


Figure 1.2: Sequential whole-body planar imaging of a mCRPC patient at selected time points post injection of 3.7 GBq Lu-177-DKFZ-PSMA-617 (anterior and posterior views) .

particular avoid severe OAR toxicities.

Despite its importance to guarantee safe and efficient RT, appropriate methods for internal dosimetry (ID) are still under investigation. Although patient-specific ID has been continuously improved over recent years, the uncertainty or error, respectively, of absorbed dose estimates is still high. Thus, the possibility to fully exploit the therapeutic window is limited [29, 37, 117], although absorbed-dose-response-relations could be established for several therapies [121]. ID is hardly standardized, however, involves multiple methodological aspects, i. e. the determination of the patient-specific three-dimensional activity distribution over time, the appropriate co-registration and segmentation of image data to identify accumulating source regions and target structures, and the absorbed dose calculation itself [46, 47, 64, 66, 68, 115]. On the other hand, ID requires a high number of quantitative measurements to assess the patient-specific time-activity-curve (TAC) in malignant tissues and OAR. The latter results in a severe increase in clinical workload and patient burden. Thus, offering RT to a high number of patients suffering from advanced cancer disease and a bad health condition requests a permanent trade-off be-

tween dosimetric accuracy and clinical feasibility. The latter is in particular true regarding bone marrow dosimetry, as the active bone marrow is probably the most critical although most challenging and most effort-demanding OAR [29, 70, 102].

2 | Basics of nuclear medicine imaging and internal dosimetry

2.1 Nuclear medicine imaging devices

2.1.1 Basics of Lutetium-177 imaging for internal dosimetry

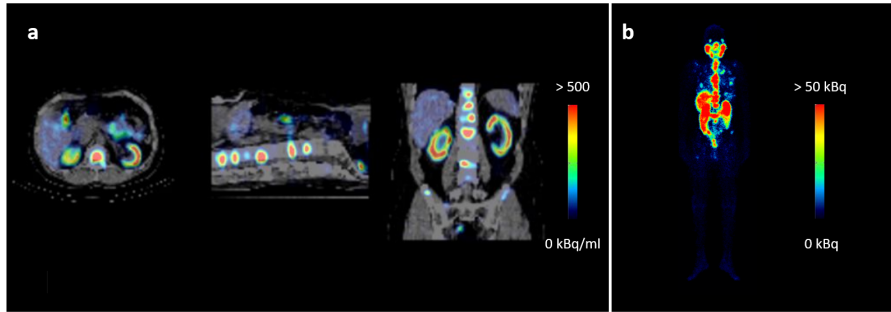


Figure 2.1: Quantitative Lu-177 SPECT/CT imaging (a) and quantified whole-body planar scintigraphy (b) for a mCRPC patient 24 h post injection of 3.7 GBq Lu-177-DKFZ-PSMA-617.

Nuclear medicine imaging is a vitally important tool in radionuclide therapy (RT) and internal dosimetry (ID), as the latter relies on the knowledge of the spatial and temporal intra-patient radionuclide distribution. For RT, β^- -emitting or α -emitting radionuclides are employed, however, radionuclides with co-emission of an additional diagnostic component are preferred, as the latter allows to measure the radiopharmaceutical distribution in vivo with regard to ID applications [35, 86, 115]. Lu-177 ($^{177}_{71}\text{Lu}$) is the currently most widely used radionuclide during RT of neuroendocrine tumors (NET) and metastasized castration-resistant prostate cancer (mCRPC), as it is characterized by a long physical half-life (6.7 days) suitable for therapeutic applications, and a short-range therapeutic β^- -component (maximum energy 498 keV; maximum range for soft tissue: 1.7 mm), accompanied by a sufficiently strong γ -emission [39, 86, 122]. Lu-177 undergoes β^- -decay to Hafnium-177 ($^{177}_{72}\text{Hf}$),



while after 20.7 % of all disintegrations Hafnium-177 is in an excited state ($^{177}_{72}\text{Hf}^*$) [10]. Both, the β^- -particle (e^-) and the electron anti-neutrino ($\bar{\nu}_e$), are released to maintain physical conservation laws [7]. The further de-excitation of Hafnium-177 to its ground state ($^{177}_{72}\text{Hf}$) results in the formation of two main γ -emissions of 113 keV and 208 keV at an abundance of 6.2 % and 10.4 %, respectively, which can both be employed for Gamma camera imaging [10, 86]:





Figure 2.2: Dual-headed Siemens Symbia Intevo T16 SPECT/CT Gamma camera system.

2.1.2 Gamma camera imaging

Gamma cameras, also called Anger or scintillation cameras, employ the scintillation principle to generate two-dimensional (planar scintigraphy) or 3D (Single-Photon-Emission-Computed-Tomography (SPECT)) views of the intra-body radionuclide distribution (Figure 2.1). Most systems are equipped with two detector heads, which are capable to move around the patient within a defined orbit to gather multiple two-dimensional projections through the intra-patient radionuclide distribution (Figures 2.2 and 2.3). For state-of-the-art systems, each detector head is build up of a changeable collimator, a large scintillation crystal, and multiple photomultiplier tubes (Figure 2.4). The collimator consists of a high- Z material (e. g. lead) and acts as a mechanical lens, which focuses the isotropically emitted γ -radiation to the detector head. In particular, for image generation a relation between the point of γ -origin and γ -detection has to be established. The collimator is composed of small, typically parallel-oriented, and usually hexagonal-shaped holes, which are separated by walls or so-called septa of high- Z material. Thus, all γ -photons that enter the holes within a pre-defined opening angle can pass the collimator (Figure 2.4), while γ -photons from undesired directions are ideally absorbed by the septa. Different collimators of varying thickness, hole diameter, and consequently resolution as well as sensitivity are available, and selected according to the clinical imaging application and γ -energy of the radionuclide of interest. The scintillation crystal is likewise manufactured from a high- Z material, typically sodium-iodine doped with Thallium (NaI(Tl)), to ideally enforce complete and immediate absorption of incoming γ -photons. However, incoming γ -photons usually undergo multiple interactions and only deposit a fraction of their energy within the scintillation material. Each energy deposition leads to an excitation of electron transitions within the crystal material. During relaxation of these excited states, appropriate doping causes the generation of photons in the visible light range, which are further guided to the photomultiplier tubes. The latter convert the relaxation photons to an amplified electrical signal, via photoelectric interactions in the photomultiplier cathodes plus a subsequent acceleration and multiplication of the released photoelectrons within multiple dynodes. The resulting electrical signal can be post-processed by appropriate subsequent electronics to form a final projection of the radionuclide distribution through the patient body, resulting in measured γ -events per projection pixel within the energy window of interest (Figure 2.3) [5, 7, 132].

2.1.3 Image-degrading effects

The measured projection data, i. e. the measured signal intensity at a given pixel of the projection matrix, is not solely linked to the intra-patient radionuclide distribution, but distorted by various physical

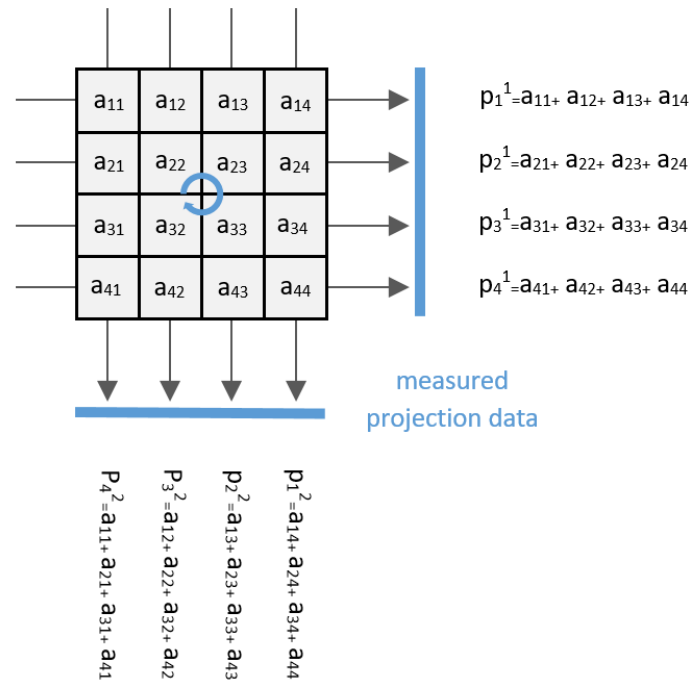


Figure 2.3: Schematic representation of projection generation via Gamma camera measurement. Values a_{ij} denote the activity distribution within the object of interest, which is projected onto the detector head. p_k^a describes the γ -events measured in projection pixel k and at projection angle a .

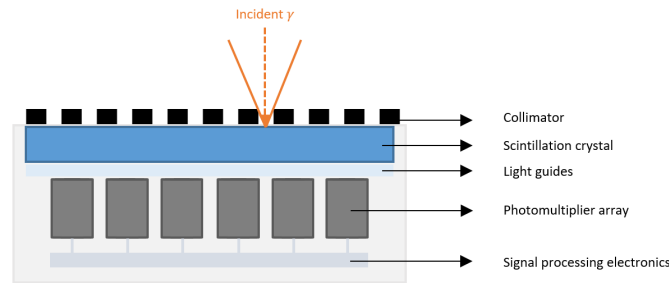


Figure 2.4: Schematic view of a Gamma camera detector.

effects originating either within the patient body or the Gamma camera device [7, 35, 115, 132]. When passing through the patient body, γ -photons interact with the surrounding body tissues, i. e. they can be absorbed or scattered. Both processes lead to photon flux attenuation from the original photon path:

$$N(x) = N_0 \cdot \exp\left(-\int_0^x \mu(E, x') dx'\right), \quad N_0 = N(x=0). \quad (2.3)$$

$N(x=0)$ and $N(x)$ refer to the initial photon flux and the photon flux after distance x , respectively. $\mu(E, x')$ denotes the photon attenuation coefficient, which describes the probability for an interaction to occur per unit path length. $\mu(E, x')$ is different for each γ -energy E and each body tissue [95]. While photon flux attenuation in general leads to a decrease of the measured intensity signal per defined pixel of the projection matrix, photon scattering itself causes an additional distortion of the overall intensity distribution [35, 86].

Motion, e. g. breathing motion or sudden patient movements during the image acquisition, is another

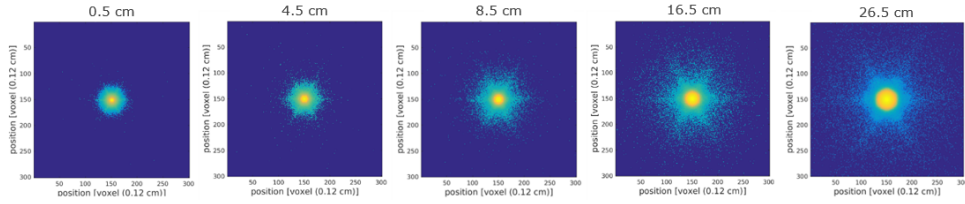


Figure 2.5: SIMIND simulation study of a Lu-177 point source measured at different distances to the detector head and for a Siemens medium-energy-low-penetration collimator. The broadening of the point source representation with increasing distances is well noticeable, in combination with collimator scatter (halo) and septal penetration (star pattern).

important patient-related effect that distorts the signal distribution within each projection, i. e. it leads to a blurring of the projection data. Especially sudden, random, and thus not predictable patient movements are challenging to model, and are more likely to appear for patients with a bad health condition (e. g. pain) and for long measurement times [7, 35, 66].

Image-degrading physical effects are also caused by the collimator, which ideally solely focuses the incident γ -radiation within a pre-defined direction to the detector head. However, this focusing is in general not perfect, and the interaction between γ -photons and collimator leads to a very complex pattern. More precise, a point source of activity is in general not represented as a simple point on the detector [7, 28, 35]. The finite size of the collimator hole allows only for a focusing within a geometrically defined opening angle (geometrical collimation; Figure 2.4), which leads to a broadened representation of the original point source, with the extent of broadening being additionally dependent on the source-to-detector distance (Figure 2.5). This effect is called distance-dependent geometrical collimator-detector-response (CDR). Further, γ -photons impinging from undesired directions are not perfectly shielded by the septa. Scattering within the collimator septa can direct undesired γ -photons to the crystal surface, and especially high-energy γ -photons can fully pass the septa (septal penetration). Collimator scattering leads to an additional isotropic blurring of the detector response function, while septal penetration can lead to a pronounced anisotropy of the detector response. For hexagonal-shaped holes, septal penetration produces a well-known star pattern (Figure 2.5).

Crystal and the photomultiplier system define a specific intrinsic and finite energy and spatial resolution of the system, although for Gamma camera imaging the overall system spatial resolution is more dominated by the collimator and radionuclide under usage [132]. The finite system spatial resolution causes the so-called spill-over effect. In particular, spill-over is noticeable for objects with a size below approximately three times the characteristic spatial resolution of both, system and radionuclide. The measured intensity signal is blurred over the object boundaries (spill-out) into the surrounding structures (spill-in), leading to a loss of intensity signal within the object itself [7, 35, 132].

Further, the finite relaxation time of the crystal material leads to a loss of detection sensitivity in case of high count rates or high activity concentrations. If the crystal is in a fully excited state, further incoming γ -photons cannot be detected until relaxation has been reached (dead time), resulting in an intensity loss with regard to the measured signal (dead time loss) [7, 127, 132].

2.1.4 SPECT reconstruction

As already stated, the acquisition of multiple projections around the patient body allows for 3D reconstruction of the intra-body radionuclide distribution (SPECT). A detailed description of SPECT image reconstruction can be found in [7, 24, 132]. The currently most common reconstruction algorithm is the ordered-subset-expectation-maximization (OSEM) algorithm, which is in turn based on the maximum-likelihood-expectation-maximization (MLEM) algorithm [114]. MLEM tries to iteratively find that vec-

for \vec{x} of image elements $x_j, j = 1, \dots, N$ with the highest likelihood to obtain the measured projection data \vec{y} of pixel values $y_i, i = 1, \dots, M$. Starting from an initial image estimate \vec{x}^0 (e. g. image containing a homogeneous non-zero distribution), the image is updated step-by-step by comparing the measured projection data \vec{y} with the projection estimate $A\vec{x}^k$ of the current image estimate \vec{x}^k :

$$\vec{x}^{k+1} = \vec{x}^k \frac{1}{A^T \mathbf{1}} \cdot A^T \left(\frac{\vec{y}}{A\vec{x}^k} \right), \quad (2.4)$$

[104] or equivalently using index spelling

$$x_j^{k+1} = x_j^k \cdot \frac{1}{\sum_i a_{ij}} \sum_i a_{ij} \frac{y_i}{\sum_j a_{ij} x_j^k}. \quad (2.5)$$

\vec{x}^{k+1} denotes the updated image estimate. A and A^T correspond to the forward-projection and backward-projection operator, respectively. More precisely, A is a mathematical representation of the measurement process, and ideally composes a realistic model of the measurement device and all physical processes during the image acquisition (see section 2.1.3). Thus, elements a_{ij} of A represent the probability that a γ -photon emitted in image voxel j is detected by projection pixel i . A^T mathematically corresponds to the reverse operation of A .

For OSEM, the update process is not performed over all projections at once, but by using a projection subset S of them, leading to an increased reconstruction speed:

$$x_j^{k+1} = x_j^k \cdot \frac{1}{\sum_{i \in S} a_{ij}} \sum_{i \in S} a_{ij} \frac{y_i}{\sum_j a_{ij} x_j^k}. \quad (2.6)$$

Iterative reconstruction based on OSEM provides good image quality for nuclear medicine purposes within an acceptable computational time. However, maximum-likelihood-based reconstruction is known to be more and more affected by image noise and edge artefacts with increasing number of iterations, i. e. increasing convergence [116, 126]. Thus, to obtain an acceptable image quality, usually a trade-off between convergence, noise and artefacts is necessary, and image reconstruction has to be stopped before the maximum-likelihood of the reconstructed activity distribution is reached. Image regularization can be employed for noise and artefact suppression, e. g. via post-reconstruction filters, or by specially designed intra-reconstruction filters, so-called priors. These can be, e. g., designed to restrict the deviation between voxels of a defined neighbourhood (maximum-a-posteriori (MAP) reconstruction) [24, 36, 83].

2.1.5 Quantitative imaging

Performing image-based ID requires quantitative images of the patient-specific radionuclide distribution, e. g. in units of Becquerel (Bq). However, the number of γ -events per voxel or pixel is the direct measure obtained via SPECT or planar imaging, while the measured distribution of γ -events is additionally distorted from physical factors during the imaging process (see section 2.1.3) [35, 86, 115]. Using iterative reconstruction algorithms (e. g. OSEM), SPECT quantification can be directly performed during the reconstruction process itself, as the modelling of physical disturbing factors can be directly included within the projection model A (see equation (2.4)) [7, 35]. Most of the state-of-the-art quantitative SPECT reconstruction algorithms used for ID include corrections for photon flux attenuation, photon scattering, and the distance-dependent geometrical collimator-detector-response (CDR) (see sections 2.1.5.1-2.1.5.3) [35, 86]. Methods to correct for other sources of errors (e. g. patient motion, dead time) are less in use, respectively, not yet fully investigated or introduced for applications in ID, although available for a few dedicated applications [38, 82, 92, 127]. After the corrected number of measured γ -events (usually units of counts per second (cps)) is obtained, this number of events has to be converted to radioactive decays.

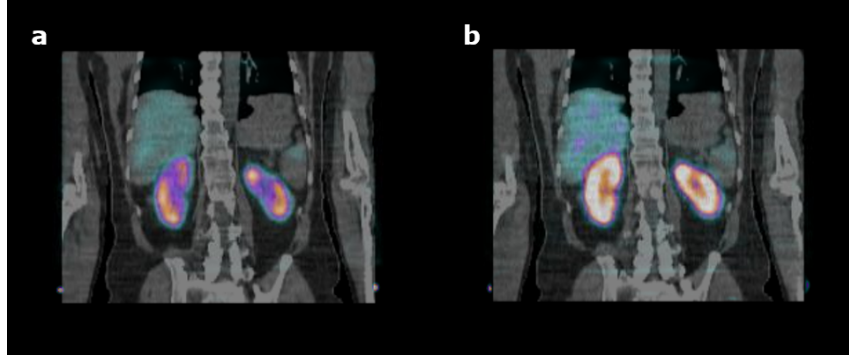


Figure 2.6: Relevance of attenuation correction for an exemplary mCRPC patient (6 GBq Lu-177-DKFZ-PSMA-617). a) and b) denote SPECT reconstruction without and with attenuation correction, respectively. Without attenuation correction, a pronounced loss of kidney uptake is noticeable.

Therefore, a suitable calibration factor has to be determined (see section 2.1.5.4) [35, 86].

2.1.5.1 SPECT attenuation correction

In case of modern hybrid SPECT/CT systems, the patient-specific Computed Tomography (CT) image can be directly used for attenuation correction [35, 99]. CT imaging exploits the specific attenuation characteristics of different body tissues to generate an anatomical image of the patient, and therefore directly includes the patient-specific spatial distribution of attenuation coefficients (μ) in Hounsfield Units (HU) per voxel j :

$$HU_j = \frac{\mu_j(E) - \mu_{H_2O}(E)}{\mu_{H_2O}(E)} \cdot 1000. \quad (2.7)$$

However, the patient CT is usually acquired using a photon energy (e. g. 120-130 keV) different from the photopeak energy of the radionuclide of interest (e. g. 208 keV for Lu-177). Thus, the CT-based HU-distribution has to be converted to a distribution of attenuation coefficients at the γ -energy of interest. Therefore, different body-tissue-imitating inserts of known density and chemical composition can be imaged within the CT scanner [35]. From the known density and chemical composition, the tissue-specific attenuation coefficients at the desired photopeak energy can be calculated. Both, measured HU-values and calculated μ -values, are then usually fitted by a bi-linear model to establish a relationship between both parameters. In this way, conversion of an arbitrary patient CT to a patient-specific μ -distribution can be achieved, which can further be employed for attenuation correction during SPECT quantification (Figure 2.6).

2.1.5.2 SPECT scatter correction

Scatter correction can be performed in multiple ways, with the optimal method of choice being highly nuclide-specific [35, 72]. For most radionuclides, scatter correction is based on the acquisition of multiple additional scatter windows, which can then be employed to estimate the amount of scattered, though detected γ -events within the photopeak window. For radionuclides with multiple photopeaks (e. g. Lu-177), usually one lower and one upper adjacent scatter window per photopeak window is acquired [86]. The amount of scattered photons per pixel i of the photopeak projection ($C_{i,scattered}$) can then be estimated from a weighted average of the γ -signal measured within the corresponding pixel of both scatter projections ($C_{i,lower}$, $C_{i,upper}$):

$$C_{i,scattered} = \frac{1}{2} \cdot \left(\frac{w_{peak}}{w_{lower}} \cdot C_{i,lower} + \frac{w_{peak}}{w_{upper}} \cdot C_{i,upper} \right). \quad (2.8)$$

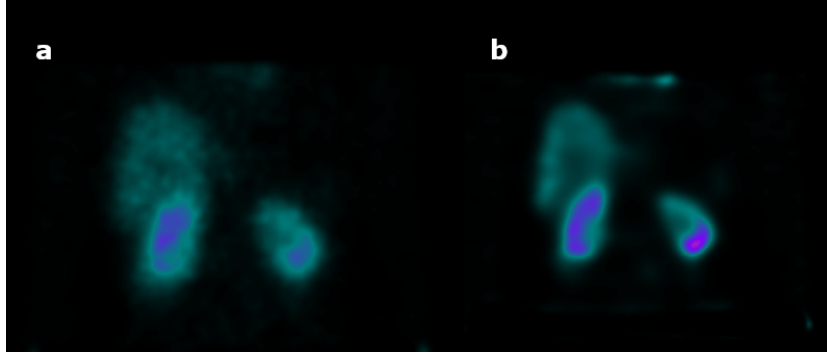


Figure 2.7: Exemplary abdominal SPECT of a mCRPC patient (6 GBq Lu-177-DKFZ-PSMA-617) reconstructed without (a) and with (b) Gaussian-based resolution compensation. Figure a) was post-filtered via a Gaussian filter of full-width half-maximum of 10 mm (post-reconstruction regularization).

w_{peak} , w_{lower} , and w_{upper} refer to the respective photopeak, lower, and upper energy window width. The respective scatter estimate $s_i = C_{i,scattered}$ can then be considered during quantitative SPECT reconstruction [72]:

$$x_j^{k+1} = x_j^k \cdot \frac{1}{\sum_{i \in S} a_{ij}} \sum_{i \in S} a_{ij} \frac{y_i}{\left(\sum_j a_{ij} x_j^k \right) + s_i}. \quad (2.9)$$

2.1.5.3 SPECT collimator-detector-response compensation

SPECT imaging requires the acquisition of multiple projections through the patient body, whereupon for each projection angle each activity signal within the patient shows a different distance to the detector head. As the geometrical CDR is distance-dependent (see section 2.1.3), each activity signal within the patient is imaged with a different spatial resolution. CDR or resolution compensation aims at correcting this effect to obtain a 3D SPECT reconstruction with comparable spatial resolution for each image point. Therefore, a small point source of activity can be imaged in varying distance to the detector head. Afterwards, a model describing the full-width half-maximum of the measured point source representation in dependence on the source-to-detector distance can be fitted to this data set. This CDR model can finally be considered within the reconstruction-specific projection model A (see section 2.1.4) [28, 35]. CDR compensation reduces spill-over effects, however, at the cost of a possible increase of edge artefacts [36] (Figure 2.7).

Correction of the distance-dependent geometrical CDR is part of many state-of-the-art quantitative SPECT reconstruction algorithms, in contrast to corrections for collimator scatter and septal penetration. The importance of these effects for quantification is nuclide-dependent, while a respective CDR compensation could be realized, e. g., by modelling the distance-dependent two-dimensional CDR point-spread-function within the projection model A [28].

2.1.5.4 SPECT calibration

Absolute quantification, i. e. calibration, of SPECT images to obtain units of activity or activity concentration (Bq or $\frac{Bq}{ml}$) can be performed via several methods [30, 134]. The appropriate method should be chosen according to radionuclide of interest and the accuracy of the reconstruction algorithm under usage [35]. A common way to determine calibration factors for absolute SPECT quantification is to use a large homogeneous phantom of known activity concentration, whereupon the phantom should be imaged and reconstructed in the same manner as it is done for patient cases. The reconstructed and relatively quantified counts per second can be set into relation to the known phantom activity to obtain

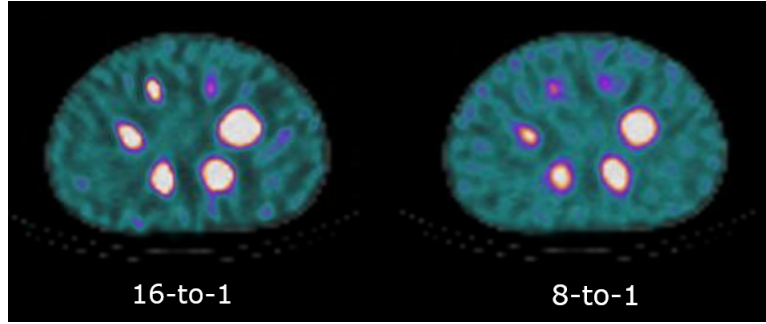


Figure 2.8: NEMA body phantom containing six spheres of varying volume (0.5-26.5 ml), filled with a Lu-177 sphere-to-background ration of 16-to-1 and 8-to-1. Reconstruction was based on a MAP algorithm (20 subsets and 16 iterations), which included corrections for photon flux attenuation, photon scattering, and resolution compensation.

Table 2.1: Recovery for the NEMA body phantom of Figure 2.8.

sphere volume [ml]	RC 16-to-1 [%]	RC 8-to-1 [%]
26.5	94	88
11.5	88	75
5.6	79	54
2.6	56	45
1.2	41	32
0.5	17	22
background	99	96

a final calibration factor ($\frac{Bq}{cps}$).

2.1.5.5 Accuracy of SPECT quantification

The accuracy of SPECT quantification is highly dependent on the reconstruction algorithm including the considered corrections, the radionuclide and the γ -energy under usage, and the typical object size of interest [35, 86]. Especially, the finite spatial resolution of the imaging system for the radionuclide and γ -energy of interest limits the quantification capabilities for small objects (see section 2.1.3). Although for iterative reconstruction algorithms quantification of small objects improves with increasing number of iterations, full object recovery cannot be reached, considering also that convergence has to be balanced against noise and artefacts for MLEM- or OSEM-based reconstruction (see section 2.1.4). Figure 2.8 shows a NEMA body phantom containing six spheres of varying size (0.5-26.5 ml) within a fillable background volume, and which contains a Lu-177 solution with a sphere-to-background ratio of 16-to-1 and 8-to-1. Via such an experimental setting, the expected recovery (RC) for a given reconstruction algorithm and imaging setting can be investigated, while the RC is obtained by comparing the known activity within spheres and background (A_{true}) with the reconstructed activity in each compartment ($A_{reconstructed}$):

$$RC[\%] = \frac{A_{reconstructed}}{A_{true}} \cdot 100. \quad (2.10)$$

Table 2.1 indicates a RC of less than 100 % for the largest sphere of 26.5 ml, for a MAP reconstruction (20 iterations and 16 subsets), which included corrections for photon flux attenuation, scattering, and resolution compensation [33]. Further, a decreasing RC for decreasing sphere sizes is noted, while for the large background volume a RC close to 100 % is reached. Particularly, for the background volume a RC less than 100 % is more likely attributed to an uncertainty in the dose calibrator measurement, i. e.

A_{true} .

A RC of less than 100 % for small objects especially implies a systematic underestimation of the activity within small lesions, and thus of the absorbed radiation dose to malignant structures. Methods for experimental or intra-reconstruction RC-correction (i. e. spill-over correction) exist, however, applying these corrections in a correct manner is challenging, as the RC is known to be affected by various aspects, e. g. lesion-specific foreground-to-background ratio (Figure 2.8 and Table 2.1) or the exact object shape. Furthermore, the determined RC is highly dependent on the exact contouring method (e. g. CT volume, isocontour) [35, 75]. Experimental RC-correction aims at determining correction factors from phantom measurements as shown in Figure 2.8. Intra-reconstruction RC-correction, e. g., tries to estimate object boundaries from additional image information (e. g. CT, MRI) to correct for spill-over effects [36]. However, the quality of the latter correction method is highly dependent on the quality of the employed additional information. Using an inadequate object information can even lead to a worsening of the results compared to a reconstruction without RC-correction. Particular care has to be taken if anatomical images (e. g. CT, MRI) shall be used for spill-over correction in molecular imaging.

2.1.5.6 Planar image quantification and comparison to quantitative SPECT

Planar image quantification usually covers corrections for photon flux attenuation and photon scattering, and final image calibration. While planar scatter correction can be performed window-based as during quantitative SPECT reconstruction, particularly accurate attenuation correction is more challenging, as an appropriate whole-body transmission measurement - unlike for hybrid SPECT/CT imaging - is in general not available a priori. The situation is further complicated as during planar scintigraphy only two-dimensional projections, e. g. anterior and posterior (Figure 1.2), of the radionuclide distribution are acquired, leading to an inherent overlap between main accumulating structures [115]. Planar attenuation correction, to obtain the corrected activity A_s within a region of interest, is usually performed via the conjugate view method:

$$A_s = \sqrt{\frac{I_a \cdot I_p}{e^{-\mu \cdot L}}} \cdot \frac{\frac{\mu_s \cdot L_s}{2}}{\sinh\left(\frac{\mu_s \cdot L_s}{2}\right)}. \quad (2.11)$$

I_a and I_p denote the measured anterior and posterior count signal, respectively, while μ , L , μ_s , and L_s refer to the effective attenuation coefficient and thickness of both, patient and region of interest [43, 115]. However, particularly the determination of pixel-wise values for μ , L , μ_s , and L_s is challenging without an appropriate transmission measurement, and usually a reference attenuation coefficient (e. g. soft tissue) is applied, in combination with reference thicknesses for L and L_s (e. g. average abdominal diameter and average kidney thickness). However, as attenuation correction is one of the most relevant factors during image quantification, such simplifying assumptions can lead to large errors. Planar transmission measurements can be performed in principal, however, these are time-consuming and limit patient comfort and throughput [69, 76].

Planar scintigraphy is inherently associated with a signal overlap of main activity-accumulating substructures, which complicates the determination of activity for individual regions of interest, i. e. single OAR or lesions (Figure 2.9). Background subtraction can be applied to correct the activity assessment in the region of interest for superimposed signal from the environment, although careful attention has to be paid to appropriately select the background region of interest [45, 115]. If sub-regions of the overall region of interest can be identified as overlap-free, these can be employed to derive an estimate of the overall region activity otherwise [45]. The challenging correction for background signal in planar images leads to an often observed positive bias of planar-based ID compared to absorbed dose estimates from 3D SPECT-based imaging [46].

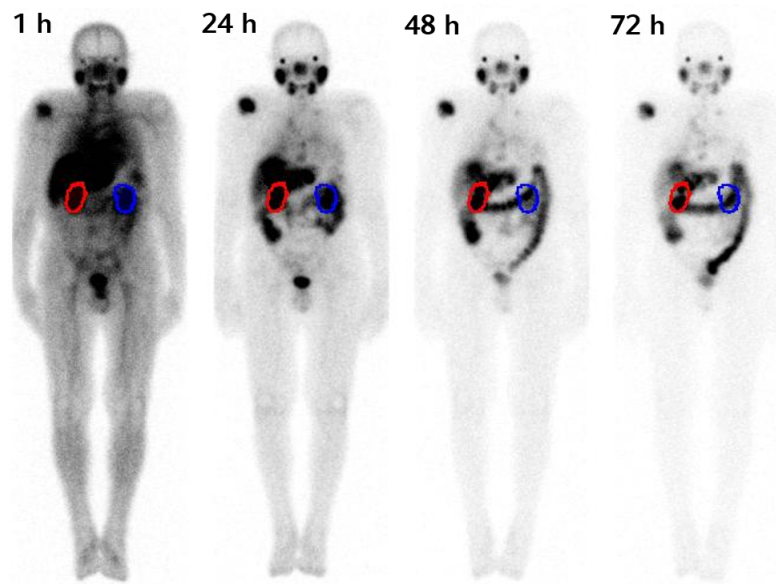


Figure 2.9: Sequential anterior whole-body planar scintigraphy of a mCRPC patient treated with 3.7 GBq Lu-177-DKFZ-PSMA-617. In particular, an increasing superposition of kidney and intestine activity is noticeable for late time points.

Due to the limited accuracy of planar image correction, final calibration has to be performed patient-specific. For calibration of patient-images, typically a patient-specific calibration factor is obtained via the known net activity within the patient body (e. g. administered activity minus measured excretion) [115]. Patient-specific net-activity-based calibration can adjust for a systematic bias in the whole-body activity, however, errors in smaller substructures cannot be generally full balanced. In combination with an increasing interest for 3D absorbed dose modelling, planar scintigraphy is more and more replaced by quantitative SPECT imaging for issues of ID, favoured by the fact that more and more commercial tools for quantitative SPECT reconstruction in combination with modern hybrid SPECT/CT systems are available. If full SPECT-based therapeutic imaging is not possible, at least combined SPECT-planar imaging protocols are recommended [46, 69, 78].

2.1.6 Positron-Emission-Tomography

Diagnostic compounds, targeting sstr or PSMA, and labelled with Gallium-68 (short: Ga-68) or Fluor-18 (short: F-18) are widely used for pre-therapeutic disease staging or therapy response evaluation (Figure 1.1) [1, 2, 8, 73, 74, 81]. Ga-68 and F-18 decay via a short half-life of approximately 70 and 110 minutes, respectively, via β^+ -decay. Within the patient body, the released positron or β^+ -particle nearly immediately (range of a few mm in soft tissue) annihilates with a surrounding electron, under subsequent emission of two co-incident and almost oppositely directed 511-keV annihilation photons. For 3D imaging of the intra-patient radionuclide distribution via Positron-Emission-Tomography (PET), this annihilation radiation can be measured in co-incidence within a ring detector, which is build up of various scintillation crystals. The requirements regarding image-degrading effects, image reconstruction, and image quantification are quite similar to Gamma camera imaging. A detailed description of PET imaging and PET image reconstruction can be found in [7]. An important difference of PET compared to Gamma camera imaging poses the electronic instead of mechanical collimation, which leads to a superior spatial resolution and quantification capabilities for PET.

2.2 Internal Dosimetry

2.2.1 MIRD scheme

Dosimetry during RT is needed to ensure a sufficiently high radiation absorbed dose to malignant structures to guarantee disease remission or at least control, while ensuring an absorbed dose as low as reasonable achievable to OAR. The physical radiation absorbed dose for a target of interest, e. g. lesion or OAR, can be derived from the radiation-deposited energy E per target mass m [95]:

$$D = \frac{E}{m}. \quad (2.12)$$

As a nuclide-specific amount of energy is released per radioactive decay, ID requires the knowledge of the amount of activity at each location within the patient body and for each time point. Quantitative imaging, preferably via SPECT, is the easiest and at the same time probably most accurate method to assess the intra-body radionuclide distribution in OAR and lesions (see section 2.1.5.6) [17, 35, 86]. However, a permanent measurement of the patient-specific intra-body activity distribution is in general not possible. Thus, usually the activity A_i at a defined number of time points t_i with $i = 1, \dots, N$ is measured. To describe the full time course of the intra-body activity within a region of interest (source; e. g. lesion, OAR, or single voxel) from injection (i. e. $t=0$) until infinity (i. e. until the last decay), an appropriate mathematical function model $A(t)$ has to be fitted to the data points (A_i, t_i) (Figure 2.10). Selected fit model, and the number and frequency of sampling points should be in agreement with the therapy-dependent pharmacokinetic [115]. However, routine clinical ID requires a trade-off between accuracy on the one hand, and patient burden as well as clinical workload on the other. Thus, the selected fit model and sampling of data points should be additionally adjusted according to clinical feasibility. Most of the pharmacokinetic models in use are based on a mono-exponential function (single pharmacokinetic phase),

$$A(t) = A(t=0) \cdot \exp\left(-\frac{\ln(2)}{T_{\frac{1}{2},eff}} \cdot t\right), \quad (2.13)$$

or a sum of exponential terms to model multiple pharmacokinetic phases [115, 118]. For the mono-exponential model of equation (2.13), $A(t=0)$ denotes the initial phase activity (e. g. at start of injection), while $T_{\frac{1}{2},eff}$ represents the phase-specific effective half-life, respectively, effective activity wash-out a, being driven by both, physical decay and biological processes:

$$T_{\frac{1}{2},eff} = \frac{T_{\frac{1}{2},physical} \cdot T_{\frac{1}{2},biological}}{T_{\frac{1}{2},physical} + T_{\frac{1}{2},biological}}. \quad (2.14)$$

Both, $A(t=0)$ and $T_{\frac{1}{2},eff}$, have to be determined from the function fit to the measured data (A_i, t_i) . Although, e. g., a bi-exponential function model can come closer to the real patient pharmacokinetic for some applications (e. g. kidneys during Lu-177-PRRT), a bi-exponential function model (four free parameters) ideally requires at least five to six quantitative measurements, compared to at least three for a mono-exponential model (two free parameters) [115]. Thus, the gain of accuracy has to be balanced against clinical requirements [34].

The total number of disintegrations within a source region, i. e. the so-called time-integrated activity \tilde{A}_{source} , can then be obtained via integration over the full time span of irradiation [17]:

$$\tilde{A}_{source} = \int_0^{\infty} A_{source}(t) dt. \quad (2.15)$$

According to the dosimetry scheme developed by the Medical-Internal-Radiation-Dose (MIRD) commit-

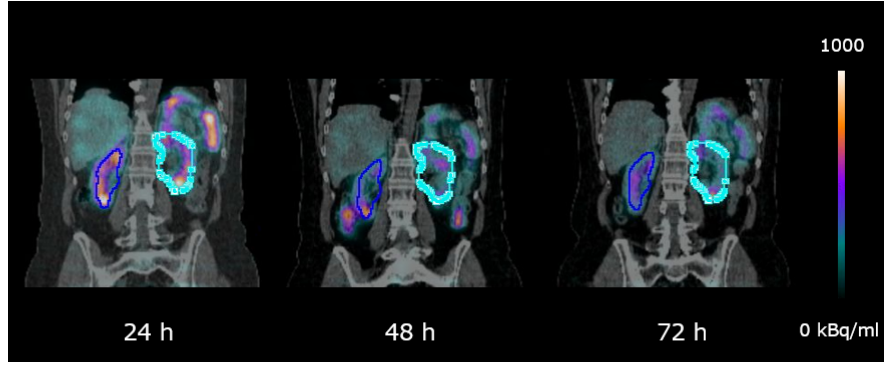


Figure 2.10: Kidney dosimetry based on sequential quantitative SPECT imaging at 24, 48, and 72 h p. i. for a NET patient treated with 7.4 GBq Lu-177-[DOTA0,Tyr3]-Octreotate. Respective dosimetry was based on mass-scaled kidney S-values and a mono-exponential function model, resulting in absorbed doses of 5.3 Gy (left kidney) and 4.4 Gy (right kidney).

tee, the mean absorbed dose D to a target region of interest can be derived via multiplication of the time-integrated activity \tilde{A}_{source} within a defined source region with appropriate absorbed dose conversion factors (S-values (S)). These S-values have been tabulated for many radionuclides and source-to-target organ combinations of interest [120]:

$$D_{target \leftarrow source} = \tilde{A}_{source} \cdot S_{target \leftarrow source}. \quad (2.16)$$

$S_{target \leftarrow source}$ thereby describes the nuclide-specific fraction of energy, which is released in the source region and deposited in the target region, per single radioactive decay, and per target mass m . For short-range-dominated emitters (β^- -emitter or α -emitter), the self-irradiation or self-absorbed dose (i. e. source = target) is the dominating absorbed dose component for main accumulating tissues (e. g. lesions, kidneys). For other targets, which show no or only a minor accumulation of the radiopharmaceutical (e. g. bone marrow for Lu-177-PRRT or Lu-177-PSMA), cross-irradiation (i. e. source \neq target) from the therapy-specific main accumulating structures (e. g. via a long-range photon component) can become important [33, 110].

Absorbed dose calculation via S-values represents the state-of-the-art method due to its simplicity. However, S-values are pre-calculated based on reference anatomies (phantoms) and standardized activity accumulations, i. e. a homogeneous uptake in source regions. Thus, S-values enable only a highly restricted consideration of the patient-specific anatomical and molecular characteristics [117, 118]. Mass-scaling via phantom and patient target masses can be employed to adapt S-values more to the patient-specific anatomy [29]. However, although mass-scaled S-values can be used to calculate the mean absorbed dose for self-irradiation and for short-range radiation (i. e. β^- , α), mass-scaling is particularly complex and inaccurate for the description of photon-based cross-irradiation (e. g. bone marrow dosimetry for Lu-177-based therapies) [64, 125]. Furthermore, consideration of lesions within S-value dosimetry is challenging, as particularly advanced cancer disease is typically associated with multiple lesions of varying shape, size, and location. Only a very simplistic approach to model the self-absorbed dose for lesion dosimetry via S-values is available, as no pre-calculation of S-values for all kind of lesion sizes, shapes, and positions is feasible. Thus, for lesion dosimetry, S-values for unity density spheres of varying size are employed [119].

2.2.2 Patient-specific 3D internal dosimetry

Classical use of organ or sphere S-values, although practical in their application, allows only for a restricted consideration of the 3D patient-specific anatomical and molecular characteristics, and only pro-

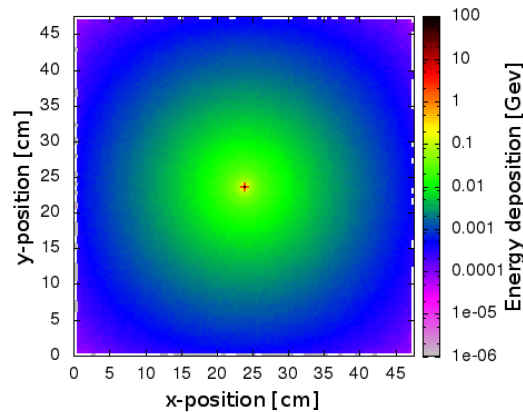


Figure 2.11: Simulated energy distribution around a Lu-177 source voxel ($0.1 \times 0.1 \times 0.1 \text{ mm}^3$; FLUKA Monte Carlo code).

vides mean target absorbed doses [29, 117, 118]. However, tomographic imaging (e. g. quantitative SPECT/CT) directly enables to assess the patient-specific 3D tissue and activity distribution, and therefore can be employed for 3D absorbed dose modelling down to the size of a single voxel (approximately 5 mm for SPECT), which represents the smallest unit of a three dimensional image, similar to a kind of technical spatial resolution. The physical spatial resolution of the derived 3D absorbed dose distribution is in turn driven by the physically available spatial resolution of the imaging system, radionuclide, and reconstruction algorithm (2.1.5.5), but can be roughly estimated as 5-25 mm for SPECT(full-width half-maximum) [35].

The Monte Carlo method represents the gold standard for absorbed dose modelling, as it is capable to simulate all physical effects relevant for absorbed dose deposition within a defined environment in a step-by-step manner, by sampling all relevant information from the known physical probability laws of particle-matter-interaction [112]. Further, many common codes offer the possibility to directly import the patient-specific medical image data (CT, SPECT, PET), leading to a full consideration of the patient-specific 3D tissue and accumulation characteristics [19, 27, 79, 87, 89]. However, due to their high complexity Monte Carlo simulations require a high computational demand, and should be performed on computing clusters to ensure an acceptable calculation time. Further, although default non-commercial solutions for many codes exist, the capabilities to set up a Monte-Carlo-based ID workflow is limited to larger clinics.

The use of absorbed dose kernels constitutes an intermediate method between a full Monte Carlo simulation and simplistic absorbed dose conversion factors. Absorbed dose kernels are simulated for a fixed tissue type (e. g. soft tissue), and model the absorbed dose distribution around a point source of activity (dose point kernel), or around a whole voxel containing a homogeneous activity distribution (voxel S-value kernel) (Figure 2.11) [16, 84, 98]. The latter is more practical for clinical use, as the medical image data is usually represented on a voxel grid, and as voxel S-value kernels can be consequently directly convolved with the patient-specific activity distribution [16]. Absorbed dose kernels can fully consider the patient-specific 3D activity information, however, as absorbed dose kernels are pre-calculated based on a fixed tissue type their validity in highly heterogeneous anatomic regions is limited, although approaches to adjust absorbed dose kernels to the anatomical environment exist [4, 91, 108, 109]. Voxel S-value kernels can provide a fast and sufficiently accurate method to calculate the 3D absorbed dose distribution of short-range particles with a maximum range below the employed voxel size, while the accuracy to describe the long-range photon absorbed dose component is limited, particularly without any corrections for tissue heterogeneity [64].

The currently most limiting factor of 3D image-based absorbed dose modelling is the challenging determination of the voxel-wise time-integrated activity. The latter requires a voxel-wise fit to multiple quantitative image acquisitions, and therefore ideally demands a perfect co-registration of all time points. However, co-registration is complicated by imperfect patient re-positioning between individual image acquisitions, as well as by intra-body or patient motion between or during the imaging sessions. Non-rigid co-registration can improve voxel-wise fitting for sub-body parts (e. g. organ-based), however, nonetheless requires careful and time-consuming monitoring. Special care has to be taken regarding activity preservation in case of larger deformations and volume changes [6, 68].

Besides imperfect co-registration, 3D absorbed dose distributions during ID are affected by spill-over, noise, and image artefacts (see sections 2.1.4 and 2.1.5.5). These effects are known to significantly alter the absorbed dose distributions, which currently prevents a pure physiological interpretation for evaluation of therapy response [88]. Image-errors are one of the most relevant sources of absorbed dose uncertainties [66], although ongoing effort tries to optimize in particular quantitative SPECT reconstruction for 3D ID [26].

2.2.3 State-of-the-art bone marrow dosimetry

The bone marrow is currently the most challenging and most effort-demanding, although probably also the most important OAR during ID. The latter is particularly true for Lu-177-PSMA therapy, as patients suffering from advanced mCRPC typically show a pronounced cancer infiltration of bone structures, a resulting pronounced uptake of the radiopharmaceutical within usual marrow-bearing regions (Figure 1.1 and 1.2), and a potentially already limited hematological function due to various pre-therapies [33, 102, 110].

State-of-the-art bone marrow ID is likewise based on the usage of S-values to model all relevant absorbed-dose-delivering components, and generally requires a large effort regarding appropriate data collection, including blood activity counting, whole-body activity measurements, and quantitative imaging [70]. The total bone marrow absorbed dose can be described as the composition of the bone marrow (BM) self-irradiation, as well as of the cross-irradiation via accumulation within non-marrow bone structures, major accumulating organs, and the remainder of the body (ROB):

$$D_{BM} = D_{BM \leftarrow BM} + D_{BM \leftarrow bone} + D_{BM \leftarrow organs} + D_{BM \leftarrow ROB} \quad (2.17)$$

$$= \tilde{A}_{BM} \cdot S_{BM \leftarrow BM} + \tilde{A}_{bone} \cdot S_{BM \leftarrow bone} + \tilde{A}_{organs} \cdot S_{BM \leftarrow organs} + \tilde{A}_{ROB} \cdot S_{BM \leftarrow ROB}. \quad (2.18)$$

The ROB time-integrated activity is thereby defined as the whole-body time-integrated activity (\tilde{A}_{WB}), minus the time-integrated activity of all defined source regions:

$$\tilde{A}_{ROB} = \tilde{A}_{WB} - \tilde{A}_{BM} - \tilde{A}_{bone} - \tilde{A}_{organs}. \quad (2.19)$$

The bone marrow self-absorbed dose is in turn dependent on a potential specific binding of the radiopharmaceutical by bone marrow or blood cells, as well as on an activity uptake within the extracellular fluid fraction (ECF) of the bone marrow compartment:

$$D_{BM \leftarrow BM} = D_{BM \leftarrow BM_{cells}} + D_{BM \leftarrow BLOOD_{cells}} + D_{BM \leftarrow ECF} \quad (2.20)$$

$$= (\tilde{A}_{BM_{cells}} + \tilde{A}_{BLOOD_{cells}} + \tilde{A}_{ECF}) \cdot S_{BM \leftarrow BM}. \quad (2.21)$$

As stated in section 2.2.1, the appropriate modelling of cross-irradiation is limited via usage of S-values,

although the accuracy can be improved via mass scaling with phantom and patient organ masses [125]. Furthermore, classical S-value bone marrow ID does not include a concept for the cross-irradiation from tumor lesions, as no tabulated S-values can be provided for each kind of patient-specific lesion distribution [110]. However, even if S-values for all kind of lesion positions, shapes, and sizes could be tabulated, the manual or semi-automatic determination of each lesion time-integrated activity and bone marrow cross-absorbed dose would not be feasible for high-lesion-load patients.

In addition to these restrictions, S-value bone marrow ID is further complicated as the patient-specific bone marrow distribution is not accounted for. As S-values are pre-calculated based on reference anatomies, S-value bone marrow dosimetry assumes a physiological bone marrow distribution [70]. However, the bone marrow is a highly variable OAR, and its exact distribution is known to be altered by multiple patient-specific parameters, particularly the presence and extent of bone metastases [90, 94]. As the patient-specific bone marrow distribution is, so far, not assessed prior to RT, the validity of state-of-the-art bone marrow ID is highly restricted by an undefined target localization. In particular, the heterogeneous bone marrow micro-structure is not accessible throughout the whole skeleton via state-of-the-art in vivo imaging. Further, even if the patient-specific whole-body bone marrow distribution can be made available prior to RT, a complete adjustment of tabulated S-values to the patient-specific, highly in-homogeneous, and 3D bone marrow distribution is not possible. Thus, to increase patient-specificity during bone marrow ID advanced Monte-Carlo-based methods are required [71, 113].

3 | Studies

3.1 Motivation and objectives of this thesis

The aim of this thesis was to extend classical bone marrow internal dosimetry (ID) for Lu-177-based radionuclide therapy (RT) to clinical demands, which require a permanent trade-off between efficiency, patient-comfort, and accuracy. The hematologically active and highly radio-sensitive bone marrow is an important organ-at-risk (OAR) for Lu-177-PRRT of neuroendocrine tumor (NET) disease, and currently possibly the most critical organ during Lu-177-PSMA therapy of metastasized castration-resistant prostate cancer (mCRPC), particularly regarding high-risk mCRPC patients with a pronounced skeletal tumor burden. However, state-of-the-art bone marrow dosimetry requires a large number of quantitative measurements to gather the Lu-177 time-activity-curve (TAC) information in all relevant accumulating source regions (see section 2.2.3). The so far requested large number of patient examinations limits the application of routine bone marrow dosimetry, if multiple therapies per week shall be offered to patients suffering from advanced cancer disease and a bad health condition. In addition, classical ID for RT is based on absorbed dose conversion factors (S-values), which were tabulated for reference anatomies and simplified accumulation patterns (i. e. homogeneous uptake in defined source regions). However, S-value-based ID was originally transferred from applications of radiation protection (e. g. diagnostic applications) to radionuclide therapy, and consequently provides only a very simplistic concept to account for the presence of lesions (see section 2.2.1). By contrast, bone marrow ID for patients with excessive skeletal metastases requires an improved consideration of the patient-specific 3D disease and anatomical characteristics, to model the bone marrow cross-irradiation via radiopharmaceutical uptake in skeletal metastases.

In the scope of the first publication underlying this thesis [51], an efficient and patient-friendly quantitative measurement scheme for clinical bone marrow ID was developed. The latter was compared to a state-of-the-art, although clinically hardly feasible measurement protocol during S-value-based bone marrow ID of patients suffering from NET or mCRPC. The included hybrid planar-SPECT approach is based on a TAC model developed during the attempts to provide an efficient multi-cycle dosimetry for kidneys and lesions for both, Lu-177-PRRT of NET and Lu-177-PSMA therapy of mCRPC. Thus, the proposed overall dosimetry protocol shall meet the requirements to provide an absorbed dose assessment for the bone marrow, non-marrow OAR, and lesions.

The second objective of this thesis was to design an approach for clinical patient-specific 3D bone marrow dosimetry, via usage of Monte-Carlo-based 3D absorbed dose modelling in combination with the Lu-177 TAC information gathered via the optimized measurement scheme of the first objective. This proposed dosimetry workflow can be further combined with image-based localization of the patient-specific 3D distribution of the hematologically active bone marrow. During the second publication underlying this thesis [58], this Monte Carlo dosimetry workflow was applied to Lu-177-PSMA therapy, as a preliminary study based on a sub-group of mCRPC patients already indicated a positive correlation between S-value-based bone marrow absorbed doses and the patient-specific metastatic bone load. This preceding study therefore clarified the need to provide more accurate and patient-specific dosimetry

methods for risk patients with pronounced skeletal metastases.

3.2 Objective 1

3.2.1 Preceding investigation of the feasibility of single-SPECT kidney and lesion dosimetry

The following preceding study was presented in [56] and [57].

Table 3.1: Imaging parameters used for Lu-177 SPECT and Lu-177 whole-body planar acquisitions.

Photopeak (width)	208 keV (15 %)
Collimator	MELP (medium-energy low-penetration)
Scatter windows (width)	lower: 170 keV (15 %) upper: 240 keV (10 %)
SPECT configuration	2 heads in H-mode (180°-orbit per head)
SPECT projections per head & time per projection	64 & 15 s
SPECT projection matrix	128 x 128 pixel (4.8 x 4.8 mm ²)
Planar scan length & scan speed	200 cm and 10 cm/min

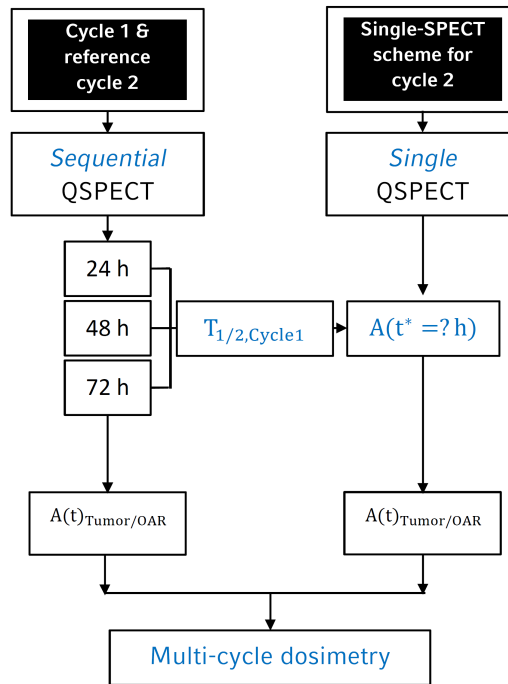


Figure 3.1: Overview of measurement schemes for lesion and kidney internal dosimetry: Full sequential quantitative SPECT (QSPECT) imaging is proposed for dosimetry during cycle 1, and applied for reference dosimetry of cycle 2. Further, for cycle 2 a reduced single-SPECT measurement scheme is investigated.

As it is the case for bone marrow ID, absorbed dose assessment for lesions and kidneys usually requires multiple quantitative measurements, preferably via SPECT imaging (see section 2.1.5.6). Further, patients usually undergo several therapy cycles of Lu-177-PRRT or Lu-177-PSMA therapy. This therapy scheme implies the question whether the same number of quantitative measurements is required for each individual therapy cycle, or whether information gathered over multiple cycles can be appropriately combined to reduce the number of measurements for selected therapy cycles with preservation of a defined demand on accuracy. In this context, a reduced measurement scheme was investigated and

established for lesion and kidney dosimetry for both, Lu-177-PRRT and Lu-177-PSMA therapy [56, 57]. The aim was to combine a single SPECT image acquired during the therapy cycle of interest with the patient-specific pharmacokinetic information gathered in a previous therapy cycle, for which sequential SPECT imaging had been performed. This approach required both, to identify the appropriate timing of SPECT imaging within the reduced dosimetry measurement scheme and to understand the course of the patient-specific pharmacokinetic behaviour over multiple therapy cycles.

The study employs data from the first and second therapy cycle of 12 patients, who underwent Lu-177-PRRT (six patients with on average 7.4 GBq Lu-177-[DOTA0,Tyr3]-Octreotate) or Lu-177-PSMA therapy (six patients with on average 3.7 or 6 GBq Lu-177-DKFZ-PSMA-617). Each patient obtained, amongst others, three 15-minute lasting SPECT acquisitions at approximately 24, 48, and 72 h p. i., either on a dual-headed Siemens Symbia T2 SPECT/CT or on a Siemens ECam SPECT system, with usage of a standard Lu-177 imaging protocol (Table 3.1) [33, 86].

For cycle 1 and cycle 2, reference dosimetry was assessed for the kidneys, representing an important OAR for both, Lu-177-PRRT and Lu-177-PSMA therapy, and three selected lesions. For each cycle, volumes of interest (VOI) were semi-automatically drawn on the SPECT at 24 h p. i., by usage of an isocontour 30-40 % of the kidney maximum, or a 40%-isocontour with regard to the mean over the lesion-specific three highest voxel values. Each VOI was manually co-registered onto the SPECT images at 48 and 72 h. Further, reference dosimetry was based on a mono-exponential fit to the time-activity-data, in combination with mass-scaled kidney and soft-tissue sphere S-values (see section 2.2.1) [120]:

$$S_{target \leftarrow source, patient} = S_{target \leftarrow source, phantom} \cdot \frac{m_{phantom}}{m_{patient}}. \quad (3.1)$$

After full dosimetry assessment for both cycles, the VOI-specific percent changes regarding absorbed dose, uptake concentration (fitted at $t=0$), and effective half-life were investigated.

For cycle 2, reference dosimetry results were compared to the absorbed dose assessment via a reduced single-SPECT dosimetry scheme. The latter combines a mono-exponential function model with the VOI-specific effective half-life of the first therapy cycle ($T_{\frac{1}{2}, Cycle1}$), and a SPECT-based VOI-uptake measurement at time t^* p. i. of cycle 2 ($A_{Cycle2}(t^*)$) (Figure 3.1). 24, 48, and 72 h p. i. were investigated as possible time points for t^* . From this single-SPECT TAC model, the VOI-specific time-integrated activity can be obtained as follows:

$$\tilde{A}_{Cycle2}(t^*) = A_{Cycle2}(t^*) \cdot \exp\left(\frac{\ln(2)}{T_{\frac{1}{2}, Cycle1}} \cdot t^*\right) \cdot \frac{T_{\frac{1}{2}, Cycle1}}{\ln(2)}. \quad (3.2)$$

For Lu-177-PRRT, no significant change of the mean (\pm standard deviation) kidney absorbed dose from cycle 1 to 2 was found (cycle 1: 0.8 ± 0.3 Gy/GBq; cycle 2: 0.8 ± 0.4 Gy/GBq), although for individual cases changes of up to 74 % were observed. An increasing absorbed dose from cycle 1 to 2 was mostly attributed to a respective increase in the effective half-life (Figure 3.2). Regarding all investigated kidney VOIs, changes of 18 % and 22 % were observed regarding the fitted uptake concentration and the effective half-life, respectively. The mean lesion absorbed dose slightly decreased from 4.9 ± 4.0 Gy/GBq to 3.9 ± 1.9 Gy/GBq, due to a reduction of the individual lesion absorbed dose particularly for patients P4 and P6 (Figure 3.2). This absorbed dose decrease was mainly attributed to an uptake decrease. Concerning all selected tumors, the absolute change of lesion uptake concentration and effective half-life was found to be 31 % and 46 %, while in 50 % of the all investigated tumor VOIs the effective half-life was the dominating factor for a change in the absorbed dose (Figure 3.2).

The analysis of Lu-177-PSMA data revealed similar results. For the mean kidney absorbed dose no severe change was observed from cycle 1 to 2 (cycle 1: 0.6 ± 0.2 Gy/GBq; cycle 2: 0.6 ± 0.2 Gy/GBq),

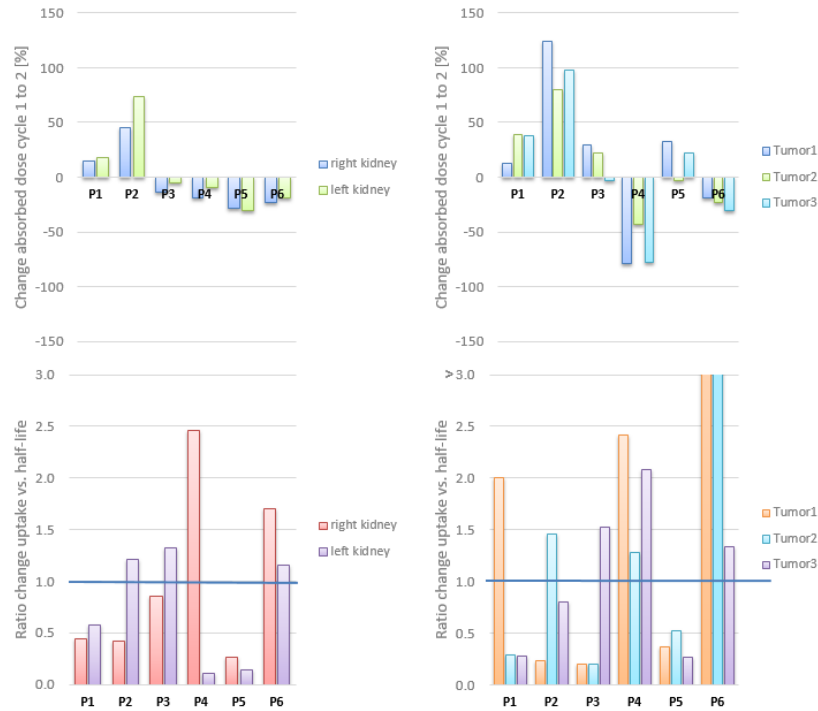


Figure 3.2: Multi-cycle dosimetry for Lu-177-PRRT: The upper row visualizes percent changes of the absorbed dose for both, kidneys and lesions. The lower row compares the change of uptake concentration (t=0) and effective half-life. E. g., a value greater than one indicates that the change in absorbed dose from cycle 1 to 2 was mostly driven by a respective uptake change.

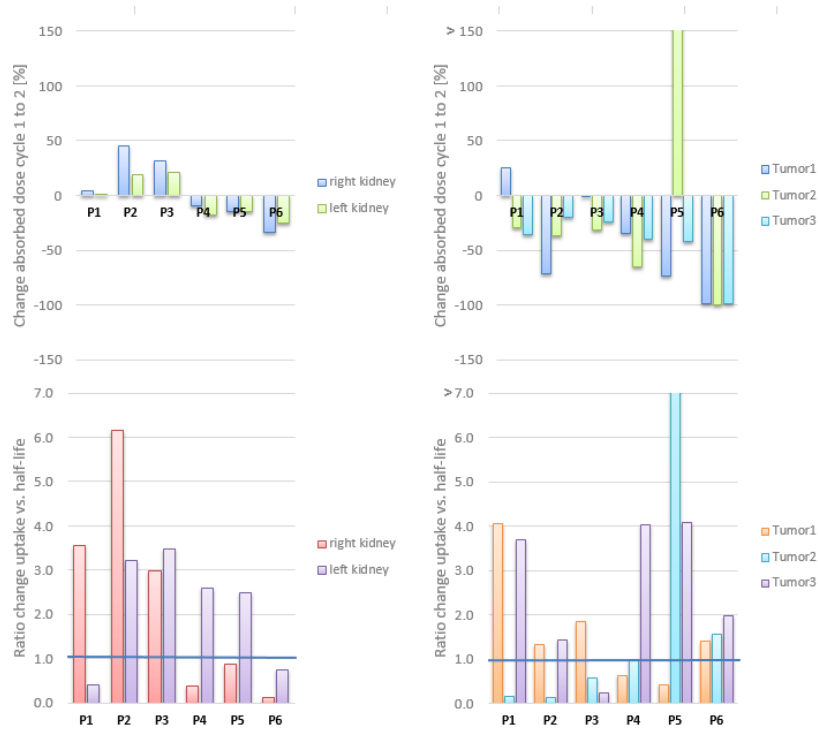


Figure 3.3: Multi-cycle dosimetry for Lu-177-PSMA therapy: The upper row visualizes percent changes of the absorbed dose for both, kidneys and lesions. The lower row compares the change of uptake concentration (t=0) and effective half-life. E. g., a value greater than one indicates that the change in absorbed dose from cycle 1 to 2 was mostly driven by a respective uptake change.

Table 3.2: Percent deviations of absorbed dose estimates achieved with the reduced dosimetry protocol using a single SPECT at 24, 48, or 72 h p. i., compared to respective results from the reference protocol employing sequential SPECT imaging.

VOI	24 h	48 h	72 h
Lu-177-PRRT			
Kidney	14.7 ± 7.9 %	6.4 ± 3.5 %	5.8 ± 3.4 %
Tumor	21.6 ± 12.6 %	20.8 ± 12.6 %	7.4 ± 5.1 %
Lu-177-PSMA			
Kidney	10.8 ± 11.3 %	5.2 ± 2.2 %	8.0 ± 4.0 %
Tumor	49.1 ± 38.4 %	16.8 ± 16.0 %	9.6 ± 9.3 %

despite an increase of individual absorbed doses for 50 % of the investigated VOIs. The latter was mainly attributed to an increased uptake, i. e. for five out of six VOIs (Figure 3.3). Both, the change of kidney uptake concentration and effective half-life, were calculated to be 15 %. The average tumor absorbed dose severely decreased from 5.0 ± 5.1 Gy/GBq to 1.8 ± 1.3 Gy/GBq. This observation was linked to a reduction of the individual lesion absorbed dose for 83 % of the investigated VOIs, with effective half-life and lesion uptake concentration being nearly equally responsible (Figure 3.3). With regard to all investigated lesion VOIs, the effective half-life changed on average by 38 %, while for the uptake concentration a mean change of 62 % was observed from cycle 1 to 2.

Although the effective half-life can significantly change between successive treatment cycles, a reduced dosimetry scheme based on the effective half-life of the previous cycle was found to be feasible within an expected uncertainty of approximately 10 %, if imaging is based on a late time point (72 h p. i.) (Table 3.2). This accuracy is well satisfying regarding the typical uncertainty of image-based ID [66] (see section 2.1.5.5), if routine dosimetry particularly for non-risk patients shall be balanced against clinical workload and patient burden. The maximum time point of 72 h p. i. is defined according to the local institution's dosimetry scheme, while the applicability of a single-SPECT measurement protocol based on a later time point has to be investigated separately, if necessary.

3.2.2 Studies on an efficient data acquisition for clinical bone marrow internal dosimetry

This section provides a short description and summary of the first publication [51] underlying this thesis. Further, relevant findings presented in [52] and [53] shall be described, to give a complete overview of efficient data acquisition for clinical bone marrow ID.

Complementary to the investigations described in the previous section, which resulted in the single-SPECT protocol for non-marrow OAR and lesion dosimetry for, e. g., every second cycle, an efficient and robust acquisition and processing protocol had to be explored and established for the estimation of the radiation absorbed dose to the active bone marrow during Lu-177-PRRT and Lu-177-PSMA therapy. While dosimetry for lesions and non-marrow OAR can be performed solely relying on 3D quantitative SPECT (see section 2.1.5.6), bone marrow ID additionally requires the determination of the whole-body and blood time-activity-curves (TAC) to derive the absorbed dose contribution from the remainder-of-the-body (ROB) and the blood (see section 2.2.3). Whole-body activity measurements can be performed via probe measurements, however, whole-body imaging is preferable, as it provides additional information regarding the patient-specific activity distribution for therapy evaluation. The optimum would be to acquire a whole-body quantitative SPECT, however, whole-body SPECT acquisitions within an acceptable patient examination time have not been fully introduced to clinical routine, yet. Thus, in order to obtain high-quality dosimetry for lesions and non-marrow OAR, and to allow for bone marrow

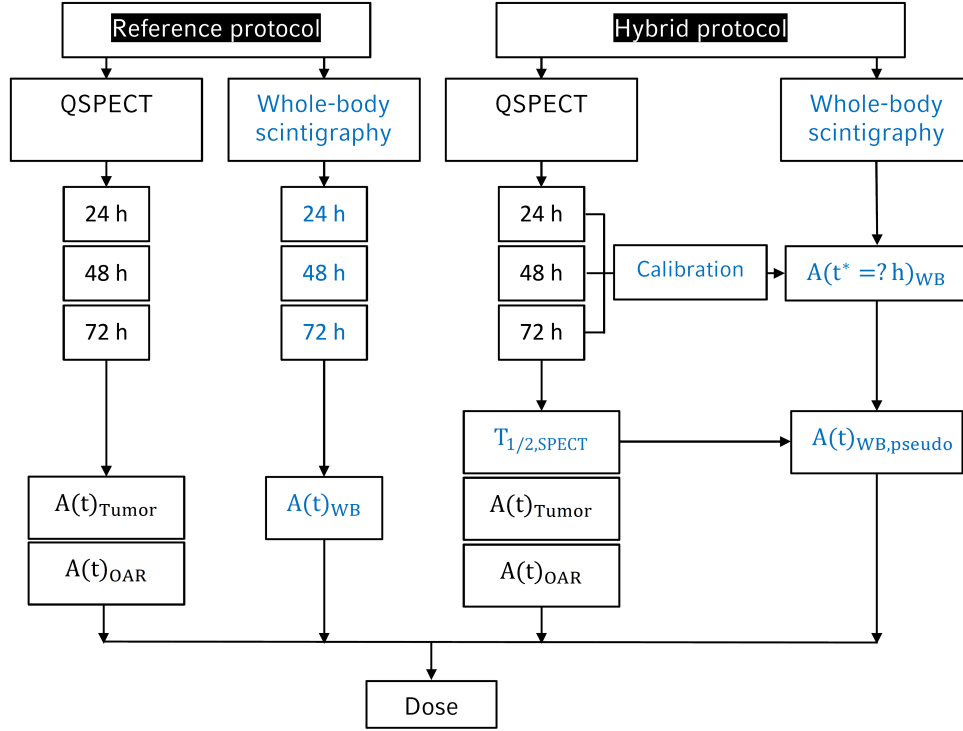


Figure 3.4: Classical (reference) dosimetry measurement protocol to allow for tumor, non-marrow OAR, and bone marrow ID, and proposed hybrid dosimetry scheme.

dosimetry, sequential SPECT and whole-body planar acquisitions including net-activity counting are typically combined, leading to an increase in clinical workload and patient burden (Figure 3.4) [110]. A common image-based Lu-177 dosimetry protocol, as described in Table 3.1 and Figure 3.4, requires examination times of approximately 45 minutes three times per patient and per treatment cycle. On the other hand, determination of the blood time-activity-curve is usually based on a bi-exponential model, which ideally requires a high number of sampling points to accurately model each pharmacokinetic phase. The minimum number would be five, however, using the lowest possible number of blood samples requires adequate timing of each sample.

The aim of this study was to provide a more efficient workflow for routine bone marrow dosimetry by appropriately condensing SPECT and planar whole-body information into a hybrid SPECT-planar protocol, which allows for both, SPECT-based dosimetry for lesions and non-marrow OAR, as well as an estimation of the whole-body TAC (Figure 3.4) [51–53]. The proposed dosimetry scheme is based on the single-SPECT TAC model proposed in section 3.2.1 [56, 57], and combines sequential quantitative SPECT imaging of the abdomen with a single whole-body planar scintigraphy acquired at a suitable time point t^* . The sequential SPECT was employed to estimate the effective whole-body wash-out by applying a mono-exponential fit to the total abdominal SPECT activity. This SPECT-based TAC was scaled with the whole-body uptake measurement at time point t^* ($A_{WB}(t^*)$) afterwards, resulting in an estimate of the true whole-body TAC and its respective time-integrated activity ($\tilde{A}_{WB,pseudo}$):

$$\tilde{A}_{WB,pseudo} = A_{WB}(t^*) \cdot \exp\left(\frac{\ln(2)}{T_{\frac{1}{2},SPECT}} \cdot t^*\right) \cdot \frac{T_{\frac{1}{2},SPECT}}{\ln(2)}. \quad (3.3)$$

Similar to study 3.2.1, the appropriate timing t^* of the single whole-body planar measurement had to be determined. In agreement with the institution's therapy procedures, 24, 48, and 72 h p. i. were investi-

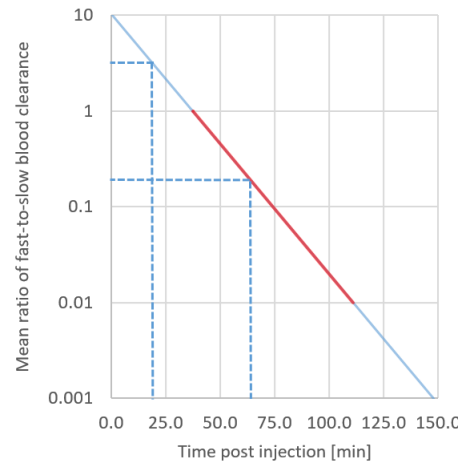


Figure 3.5: Analysis of the ratio of fast-to-slow blood clearance (average over eight Lu-177-PSMA cycles); the dashed blue line denotes the proposed timing for early blood sampling (i. e. 20/60 min post infusion). The red line denotes the drop of the fast-to-slow clearance ratio from 1 to 0.01.

gated as possible time points.

Further, a cross-calibration of whole-body planar images via the quantitative SPECT of the corresponding time point was investigated (Figure 3.4), to replace the need for excreta counting. The latter had been performed, so far, to allow for planar image calibration via the known patient-specific net-activity (see section 2.1.5.6), however, was likewise associated with a high clinical workload. The proposed cross-calibration is based on the fact that the total abdominal SPECT activity (A_{SPECT}) should be equal to the counts per second (x_{planar}) contained in the equivalent body region of the corresponding planar image, multiplied with a suitable patient-specific calibration factor ($C_{SPECT-planar}$):

$$C_{SPECT-planar} = \frac{A_{SPECT}}{x_{planar}}. \quad (3.4)$$

This SPECT-based cross-calibration of planar images was pre-investigated for eight Lu-177-PSMA therapy cycles of four mCRPC patients, who received on average 3.7 GBq Lu-177-DKFZ-PSMA-617 [52]. For these patient cohort excreta counting, and full sequential Lu-177 SPECT imaging and whole-body planar imaging was available (Table 3.1). A comparison of conventional net-activity calibration and SPECT-based calibration at 24 h p. i. yielded an average deviation of $5.7 \pm 4.8 \%$, and strong correlation (Pearson's $r=0.7$). This difference is well acceptable, considering also multiple sources of errors during reference net activity counting itself (e. g. appropriate excreta sampling and uncertainty of activity measurement).

Results from this study demonstrated that for both, Lu-177-PRRT and Lu-177-PSMA therapy, hybrid SPECT-planar bone marrow dosimetry as proposed in Figure 3.4 is feasible within an average deviation of less than 5 % compared to full sequential whole-body planar imaging, if single whole-body planar imaging is performed at approximately 72 h (Lu-177-PRRT (mean \pm standard deviation): $2 \pm 2 \%$; Lu-177-PSMA therapy: $3 \pm 2 \%$) [51]. These results are thus in well correspondence with the experience gathered during single-SPECT lesion and kidney dosimetry (see section 3.2.1 [56, 57]).

To achieve full optimization of quantitative measurements regarding clinical bone marrow dosimetry, a reduced blood sampling scheme, was likewise investigated [52]. For the respective patient cohort, extended blood sampling was performed, i. e. 2-3 ml of venous blood were drawn from the side contralateral to injection at approximately 20, 30, 40, 60, and 80 min post start of infusion, to describe the fast blood pharmacokinetic, as well as before each image acquisition session at 24, 48, and 72 h p. i. to model the slow pharmacokinetic phase. The blood pharmacokinetic of this patient cohort was analyzed

in order to find the optimal sampling scheme based on five blood samples, which is the minimum to allow for bi-exponential curve fitting. The average effective half-life of the fast and slow blood clearance phases were identified as 11 min and 8.5 h, respectively, while the fast blood clearance was found to contribute on average 22 % to the total time-integrated blood activity and consequently blood-to-bone-marrow absorbed dose. Analysis of patient-specific blood clearance curves indicated, that particularly the appropriate blood sampling during the transition from fast to slow blood clearance is critical to accurately represent the overall shape of the bi-exponential curve fit. Both phases equally contributed to the overall blood clearance around 37 min post start of infusion, while the mean ratio of fast-to-slow blood clearance rapidly drops to one-tenth and one-hundredth until 74 min and 111 min, respectively (Figure 3.5). Consequently, the full blood sampling protocol was compared to a reduced sampling scheme relying on an early blood sampling at approximately 20 and 60 min p. i., yielding an average deviation of 5.0 ± 5.6 %. For one investigated cycle, the deviation of the five-sample protocol from extended early blood sampling reached 30 %, however, for this patient an untypically prolonged fast blood clearance was noticed.

3.3 Objective 2

3.3.1 Preceding study on the relevance of kidneys and bone marrow for high-lesion load mCRPC patients

The following preceding study was presented in [59, 61, 62].

A simplification of ID by using a reduced number of quantitative measurements, as proposed in the previous studies 3.2 and 3.3, is accompanied by the limitation that some dosimetric information can not be retrieved, resulting in a decrease of accuracy. However, the accuracy of both, single-SPECT-based dosimetry for lesions and non-marrow OAR and hybrid SPECT-planar bone marrow dosimetry, is tolerable without doubt during clinical dosimetry for Lu-177-based RT of non-risk patients. By contrast, a dosimetry as accurate as clinically achievable should be performed for, e. g., NET or mCRPC patients suffering from a decreased kidney excretion, or for patients with an expected high bone marrow absorbed dose. The risk of critical bone marrow absorbed doses is especially of concern during Lu-177-PSMA therapy of mCRPC, and is currently probably the most limiting factor to exploit the full therapeutic window of PSMA-targeting RT [102].

Figure 3.6 exemplarily shows the whole-body planar scintigraphy of two mCRPC patients at 24 h post Lu-177-PSMA therapy (3.7-6 GBq Lu-177-DKFZ-PSMA-617). For patient case a), a strong retention of the radiopharmaceutical in the visceral liver metastases is visible, accompanied by an accumulation in typical OAR, i. e. both kidneys, the PSMA-positive salivary and lacrimal glands, as well as a beginning accumulation in the PSMA-positive intestine. mCRPC patient b) presents with a pronounced bone lesion load, leading to a nearly complete absorption of the radiopharmaceutical in the skeleton, while the accumulation in kidneys, glands, and intestine is almost negligible. Patient b) thereby represents a common clinical case during Lu-177-PSMA therapy of mCRPC, and further illustrates a severe conflict regarding the current therapy approach: The accumulation pattern of patient case b) indicates a low absorbed dose to the typical non-marrow OAR, which would initially allow for a more aggressive therapy approach by usage of higher amounts of radioactivity. However, the pronounced radiopharmaceutical retention in the skeleton might lead to a significant cross-irradiation of the highly radio-sensitive active bone marrow, and potentially result in severe hematological toxicity.

The presented study aimed at providing a first investigation of this initially intuitive assessment [59, 61, 62]. Using the developed hybrid SPECT-planar dosimetry protocol of study 3.2.2 in combination

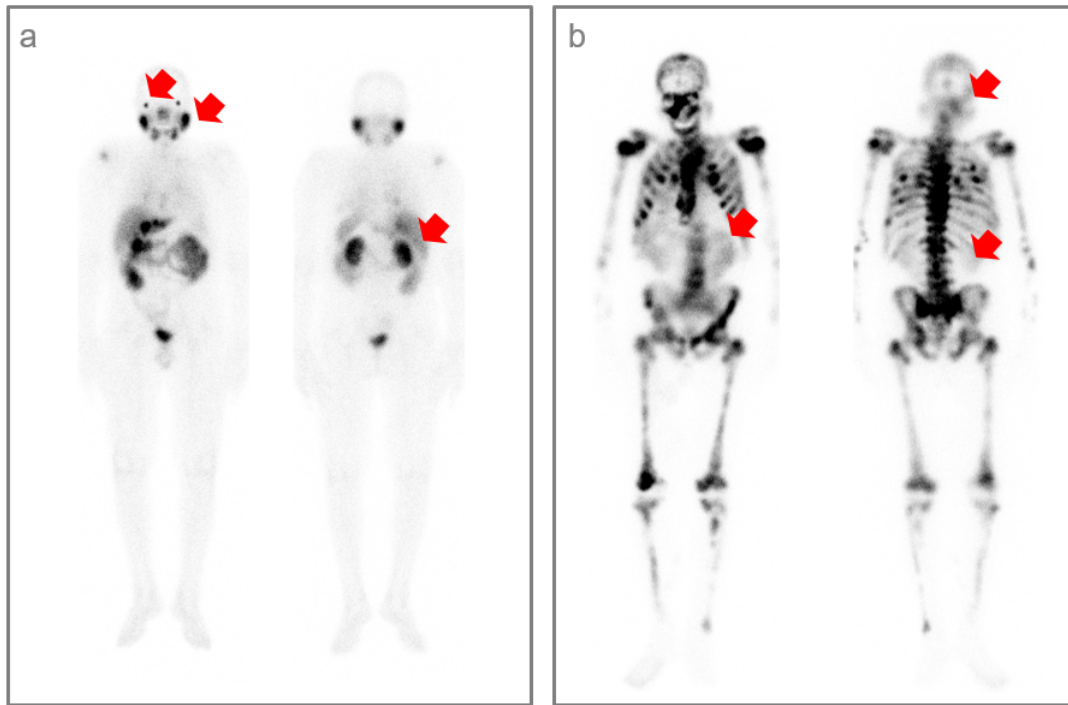


Figure 3.6: Anterior (left) and posterior (right) view of two mCRPC patients 24 h p. i. of approximately 3.7 (patient a) and 6 GBq (patient b) Lu-177-DKFZ-PSMA-617.

with a conventional sequential Lu-177 SPECT-based dosimetry (see study 3.2.1), the absorbed dose to the bone marrow and the kidneys as exemplary non-marrow OAR was evaluated for 14 mCRPC patients (3.7 or 6 GBq Lu-177-DKFZ-PSMA-617; 10 mCRPC patients with available blood sampling), and finally correlated to the patient-specific whole-lesion or bone tumor burden, respectively. The latter was semi-automatically segmented on the pre-therapeutic Ga-68-PSMA-11 PET/CT data, based on a 40%-isocontour threshold of the PET image maximum, intersected with a bone VOI derived from the diagnostic CT of the PET/CT acquisition. To derive the total bone marrow absorbed dose, ROB, blood, and the kidneys were considered as specific source regions (see section 2.2.3) [33, 44, 51, 110].

Average (\pm standard deviation) kidney and bone marrow absorbed doses were 0.33 ± 0.16 Gy/GBq (range: 0.03-0.59 Gy/GBq) and 16 ± 10 mGy/GBq (range: 6-36 mGy/GBq). Kidney absorbed doses were proven to show a significant and strong negative correlation with the segmented bone lesion load (Pearson's $r=-0.9$, $p<0.05$), while the bone marrow absorbed dose significantly increased with increasing metastatic bone load (Pearson's $r=0.8$, $p<0.05$) (Figure 3.7). For patient case a) presented in Figure 3.6, kidney and bone marrow absorbed doses of 0.56 Gy/GBq and 13 mGy/GBq were found, while for mCRPC patient b) respective values were 0.07 Gy/GBq and 36 mGy/GBq. For the patient cohort under study, ROB and blood contributed on average 66 % and 30 % to the total bone marrow absorbed dose, while the contribution of the kidneys was nearly negligible (mean of 4 %; Figure 3.8).

Results from this study demonstrate that for mCRPC patients with a high metastatic lesion load the bone marrow is the main OAR, leading to a strong need of dosimetry calculations as realistic as possible. Although S-value bone marrow absorbed doses were found to be well below the typically applied critical threshold of 2 Gy [110], the significance of classical S-value bone marrow dosimetry for Lu-177-PSMA therapy is limited, especially due to a missing patient-specific concept to accurately consider bone marrow cross-irradiation from skeletal lesions (section 2.2.1). In this study, the overall lesion activity was considered as part of the ROB compartment, which is one possible simplified approach to at least account for the prolonged lesion-associated activity retention in the patient body (Figure 3.8) [110,

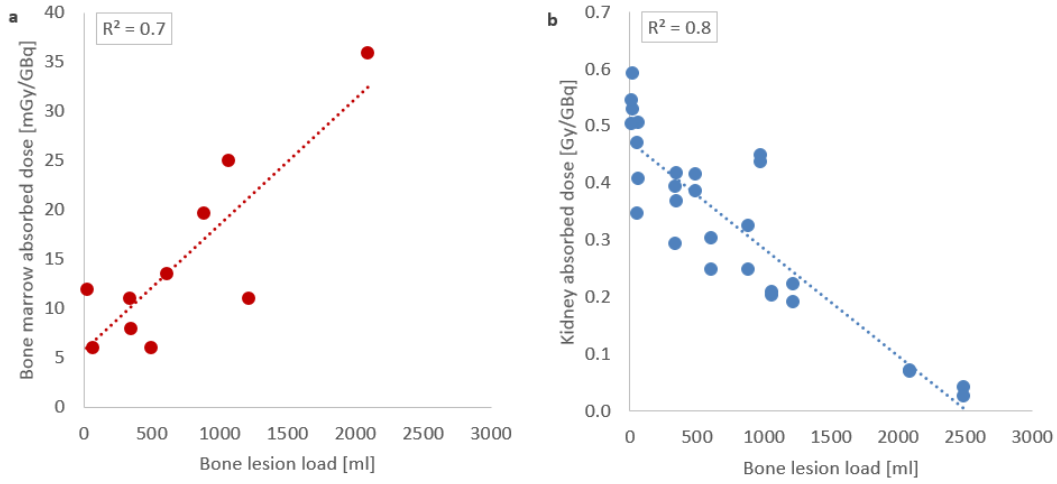


Figure 3.7: Correlation of bone marrow (a) and kidney (b) absorbed doses with the patient-specific bone lesion volume.

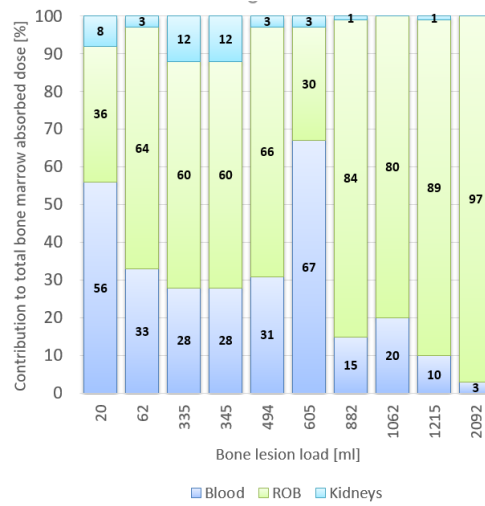


Figure 3.8: Source-specific contributions to the total bone marrow absorbed dose as evaluated for 10 mCRPC patients.

124]. Despite the high correlation between S-value bone marrow absorbed doses and the segmented bone lesion load, absolute values might be severely underestimated during classical S-value ID. Particularly, the high correlation coefficient found for S-value bone marrow dosimetry and patient-specific bone lesion load is somewhat mis-leading, as it is mainly driven by the data of patient b). Omitting the respective data from the patient cohort of Figure 3.7 a) leads to a less pronounced (Pearson's $r=0.6$), although still positive correlation.

3.3.2 Investigation of a clinical 3D Monte-Carlo-based bone marrow dosimetry workflow

This study summarizes the second publication underlying this thesis [58], as well as related findings presented in [49, 50, 54, 55].

Study 3.3.1 illustrated the strong request for 3D bone marrow dosimetry for Lu-177-PSMA therapy, to particularly account for the patient-specific 3D lesion distribution. Thus, the first Monte-Carlo-based bone marrow ID workflow was developed, which is applicable in clinical routine for high-risk mCRPC patients [58]. The Monte Carlo workflow was set up based on the FLUKA code, which has already been

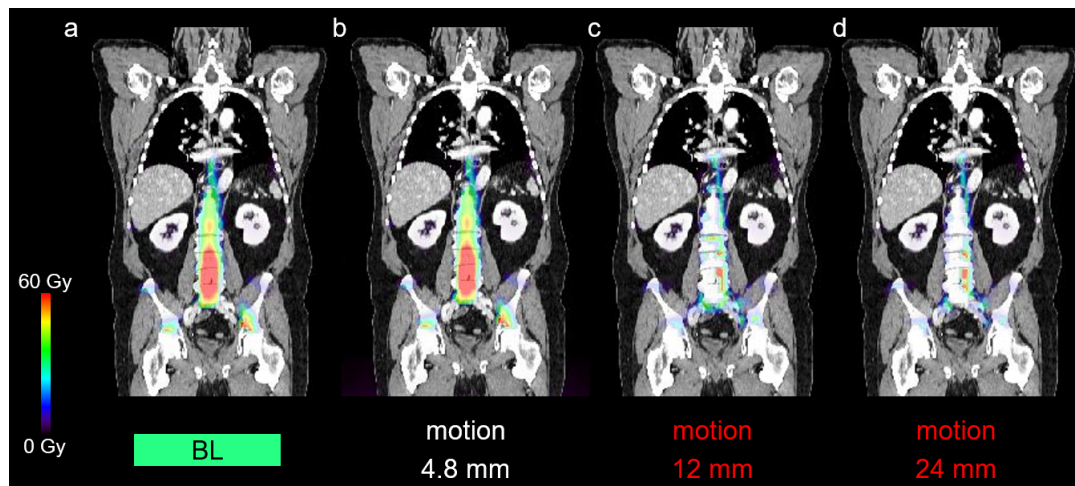


Figure 3.9: Simulation study to demonstrate the relevance of patient motion during voxel-wise absorbed dose calculation for an exemplary mCRPC patient case (6 GBq Lu-177-DKFZ-PSMA-617.); BL (a) denotes the baseline motion-free absorbed dose calculation, while Figures b-d visualize the change of the absorbed dose distribution after different magnitudes of patient motion had been artificially introduced into the SPECT raw data.

Table 3.3: Effect of patient motion (Figure 3.9) on absorbed dose calculation for three selected lesions; percent deviations are calculated with respect to a motion-free SPECT acquisition.

Motion	Tumor 1	Tumor 2	Tumor 3
4.8 mm	-8 %	0 %	0 %
12 mm	-95 %	-92 %	-50 %
24 mm	-97 %	-97 %	-57 %

validated for nuclear medicine applications in previous studies [19].

The first working step was to set up a basic Monte-Carlo-based ID workflow, which accurately imports both, the desired patient-specific molecular and anatomical information. A validation of simulated Lu-177 organ S-values and Lu-177 S-value kernels via usage of tabulated data led to an excellent agreement (deviation approximately 1 %) [84, 120]. Further, in a second step, the appropriate patient data for 3D bone marrow absorbed dose modelling had to be identified. As described in section 2.2.2, full 3D absorbed dose modelling relies on voxel-wise fitting of sequential SPECT data to obtain the voxel-wise time-integrated activity. However, voxel-wise fitting of sequential SPECT data is challenging due to image noise and artefacts, as well as mis-alignments between individual SPECT scans due to patient motion and uncertainties in patient re-positioning. Even small motion magnitudes can lead to severe artefacts in calculated absorbed dose distributions [49, 50] (Figure 3.9 and Table 3.3).

In studies 3.2.2 and 3.3.1, the ROB including the lesions and the blood were identified as main source regions, which contribute to the total bone marrow absorbed dose during Lu-177-PSMA therapy, followed by the kidneys. Thus, the method of choice for patient-specific bone marrow dosimetry was to combine compartment-based time-integrated activity determination for ROB, lesions, kidneys, and blood with Monte-Carlo-based absorbed dose simulation to balance both, strength and limitations, of simplistic organ-level and full 3D dosimetry [58]. A template-based dosimetry workflow was introduced, which combines a PET/CT-based segmentation of all relevant source compartments plus the skeleton as target region with the TAC information gathered during therapeutic Lu-177-imaging and blood sampling according to the optimized measurement scheme proposed in study 3.2.2 [51] (Figure 3.10).

Using the PET/CT data for template generation offers several advantages for issues of bone marrow dosimetry: first, Ga-68 PET/CT offers a higher spatial resolution compared to Lu-177 SPECT/CT imag-

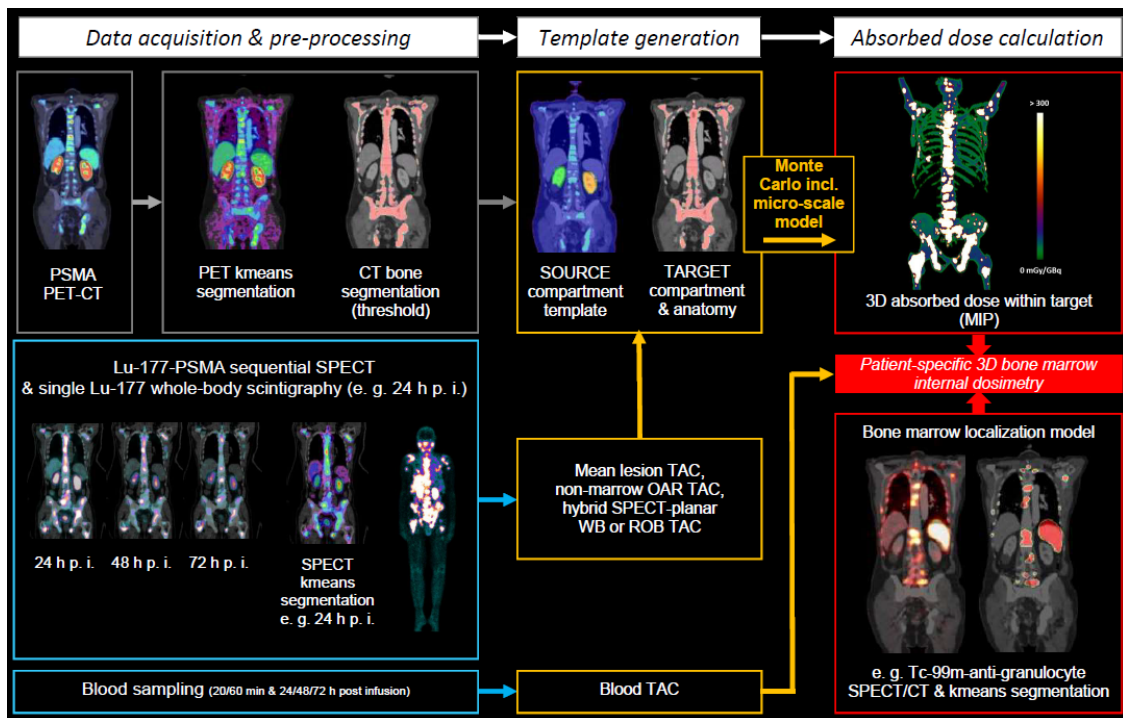


Figure 3.10: Template-based dosimetry workflow for patient-specific 3D bone marrow dosimetry.

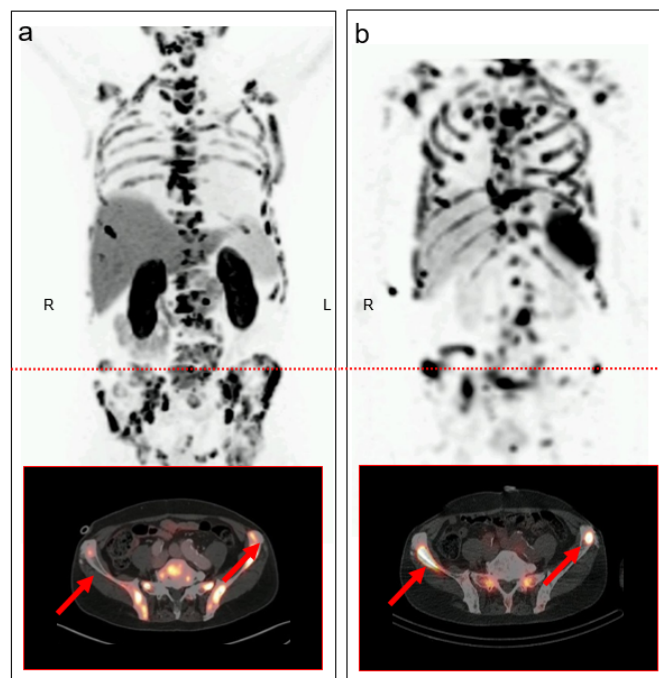


Figure 3.11: Comparison of Ga-68-PSMA-11 PET lesion accumulation (a) with image-based active bone marrow localization via Tc-99m-anti-granulocyte SPECT/CT (b) for a mCRPC patient suffering from a pronounced skeletal metastasis. The upper row visualizes the respective maximum-intensity projection (MIP), while the lower row shows an exemplary transverse slice (denoted by the red dashed line in both MIPs).

ing; second, the pre-therapeutic Ga-68-PSMA PET/CT usually covers a large part of the patient body from the middle of the head to approximately the knees, while for most of the mCRPC patients included in this study only Lu-177 SPECT imaging of the abdomen was available [58].

Table 3.4: Comparison of different models regarding macroscopic active bone marrow localization: MC1 and MC2 denote results from Monte-Carlo-based absorbed dose calculation assuming either no or complete active marrow displacement from skeletal lesions, respectively. For gMC3, Monte Carlo absorbed dose calculation was combined with image-based patient-specific active bone marrow localization via Tc-99m-anti-granulocyte SPECT/CT. SMIRD corresponds to results from classical organ S-value bone marrow dosimetry.

Case	MC1 [mGy]	MC2 [mGy]	gMC3 [mGy]	SMIRD [mGy]
1	1123	225	718	46
2	684	202	408	40

Bone marrow ID is further generally limited by the fact that the bone marrow micro-structure is not visible on clinical imaging modalities. The bone marrow itself consists of a mixture of hematologically active bone marrow (red marrow), which represents the important target for applications in RT, and in-active bone marrow (yellow marrow). This bone marrow mixture is in turn mostly located in small marrow cavities with a typical diameter of the order of $100\ \mu\text{m}$, which are further separated by small ridges of hard bone. Thus, an abstract weighting-based model was adapted to applications in RT, to adjust Monte-Carlo-based absorbed dose calculation to the small-scale nature of the bone marrow target [54, 55, 58]. It estimates the absorbed dose to the active bone marrow from the absorbed dose deposited within the total bone mixture, multiplied with a weighting factor w , which is dependent on the mass fractions, as well as the energy-dependent electron and photon interaction probabilities of each bone compartment. Thus, w represents an effective probability for an absorbed dose deposition to occur specifically in the active bone marrow.

Besides consideration of the microscopic characteristics of the bone marrow, also the macroscopic localization is of crucial importance for absorbed dose calculations. The active bone marrow compartment is a highly dynamic OAR, which can alter its distribution throughout the whole patient body, dependent on the patient age or with regard to self-protecting mechanisms [90, 94]. Skeletal metastases, as typically encountered during Lu-177-PSMA therapy, can release a displacement of active bone marrow from the lesion sites, while the unknown extent of such displacement processes can lead to a large range of possible absorbed dose values. For the patient cohort underlying the presented investigation [58], application of both scenarios, no displacement (MC1) and complete bone marrow displacement (MC2), resulted in a median difference by a factor of three concerning respective Monte-Carlo-derived bone marrow absorbed doses (MC1 - median: 130 mGy/GBq; MC2 - median: 37 mGy/GBq). Consequently, a priori assuming one scenario or the other for each patient can lead to severe over- or underestimations of the bone marrow absorbed dose, indicating the need for macroscopic bone marrow localization at least for identified risk-patients. For a sub-group of two mCRPC patients image-based active bone marrow localization via Tc-99m-anti-granulocyte antibody SPECT/CT was available prior to therapy, which indicated the presence of ongoing displacement mechanisms (Figure 3.11). Reanalysis of bone marrow absorbed doses for these patients resulted in values between both extreme scenarios (Figure 3.10 and Table 3.4), due to both, technical and physiological aspects. Particularly, a mis-alignment of image-based bone marrow localization with the compartment template, and the finite spatial resolution of involved imaging modalities can lead to an artificial overlap between lesions and active bone marrow distribution, and thus in an artificially increased estimate of the absorbed dose. The latter goes hand in hand with a physiologically-driven incomplete bone marrow displacement.

However, results from this investigation also demonstrate that performing S-value bone marrow dosimetry lead to a similar, in parts even larger overall uncertainty than compared to Monte-Carlo-derived absorbed dose estimates without knowing the exact location of the active bone marrow [58]. Median S-value bone marrow absorbed doses (SMIRD) were 11 mGy/GBq, and on median 17-fold to

four-fold smaller compared to MC1 and MC2, respectively. Deviations between SMIRD, MC1, and MC2 were found to be driven - as expected - by the patient-specific bone lesion load, but also by lesion activity uptake and ROB retention. Consequently, all aspects should be considered for identification of risk patients. A correlation of bone marrow absorbed doses with the decrease of blood element counts yielded a significant correlation regarding platelet counts for all dosimetry models, while highest correlation was obtained for MC2 (Pearson's $r=-0.7$).

4 | Discussion & outlook

This thesis aimed at the optimization of clinically feasible, patient-specific estimation of the absorbed dose to the active bone marrow for Lu-177-based radionuclide therapy (RT). Investigations were taken out for Lu-177-PRRT of NET and with special emphasis for Lu-177-PSMA therapy of mCRPC. After identification of a suitable quantitative measurement protocol, various strategies for absorbed dose estimation were investigated.

Classical and simple S-value-based internal dosimetry (ID), resulted in an average absorbed dose estimate of the order of 10 mGy/GBq, which at first could be considered as uncritical in relation to the typical bone marrow absorbed dose constraint of 2 Gy [110]. However, the prediction of hematological toxicity via S-value bone marrow ID is limited due to the inherent lack of patient-specificity of tabulated absorbed dose conversion coefficients, and in particular due to the lack of an appropriate concept to account for the high and heterogeneous bone lesion load which is often observed for mCRPC patients. For Lu-177-PRRT, the classical S-value method has been further refined to the characteristic uptake pattern of NET patients, resulting in a good agreement with the course of blood element counts [124]. Still, the situation for NET patients during Lu-177-PRRT might be less critical, as the occurrence of pronounced bone metastases and severe hematological events is reduced compared to the situation encountered in Lu-177-PSMA therapy. Rahbar et al. reported hematological toxicity to be the most common severe event during Lu-177-PSMA therapy of 145 patients (average activity 5.9 GBq), with regard to all grades as well as grade 3-4 events [102, 122].

Data regarding the correlation between bone marrow dosimetry and hematological response has not been available for a sufficiently large patient cohort having received Lu-177-PSMA therapy, yet, although independently published data on hematological response assessment indicates a disagreement between the incidence of hematological toxicity and so far S-value-derived bone marrow absorbed doses [9, 40, 102]. Section 3.3.2 [58] demonstrated elevated Monte-Carlo-based bone marrow absorbed dose estimates compared to respective results from classical S-value ID, irrespective of the exact model used for active bone marrow localization (MC1 - median: 130 mGy/GBq; MC2 - median: 37 mGy/GBq; SMIRD - median: 11 mGy/GBq). The preliminary analysis of the correlation between nadir-to-baseline values of blood element counts and model-specific bone marrow absorbed doses, as performed for the small patient cohort of this study until eight to ten weeks after the first therapy cycle, revealed significant results ($p < 0.05$) regarding platelet response for both, Monte Carlo and S-value calculations. However, the highest correlation coefficient ($r = -0.7$) was observed for the Monte-Carlo-based calculation with assumption of complete bone marrow displacement. MC1, assuming a complete neglect of bone marrow displacement mechanisms, can be judged to lead to too drastic bone marrow absorbed dose values, as - according to the absorbed dose constraint of 2 Gy - severe hematological events should have been occurred for three to four (27-37 %) of investigated mCRPC patients.

Appropriate hematological response assessment in the scope of treatment of advanced cancer disease is challenging, as the course of blood element counts is strongly dependent on multiple patient-specific parameters, e. g. pre-therapies or hematological baseline status. Further, apart from the cross-irradiation of the active bone marrow via bone lesions, bone marrow infiltration of cancer cells alone can cause

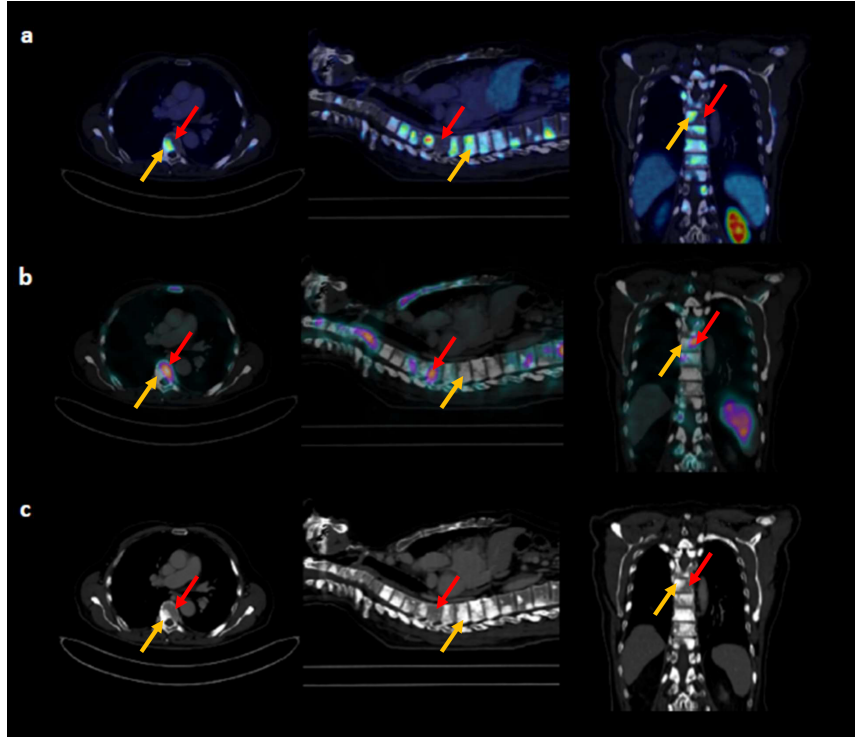


Figure 4.1: Comparison of PSMA PET/CT imaging (a), active bone marrow localization via Tc-99m-anti-granulocyte SPECT/CT (b), and results from diagnostic CT imaging (hybrid PET/CT imaging) (c) for an exemplary mCRPC patient. Yellow arrows indicate the interplay between detection of PSMA-avid lesions, active bone marrow displacement, and CT-detectable sclerosing processes. Red arrows denote regions without metastatic impairment, inconspicuous CT bone structure, and active bone marrow localization.

a worsening of the patient-specific hematological function. This implies that bone marrow dosimetry is not the sole decisive aspect to predict severe hematological events [12, 15, 102, 124, 131]. Thus, a patient stratification according to hematological risk factors, in combination with Monte-Carlo-based bone marrow ID and active bone marrow localization is advisable for future studies in order to obtain both, predictive absorbed-dose-response-relationships and realistic absorbed dose constraints. In particular, a current debate focuses on the question whether the common absorbed dose constraint of 2 Gy might be too optimistic for patients of progressed cancer disease, who already underwent various pre-therapies and consequently already present with an impaired hematological function. Further, the immediate radiation harm on blood cells due to the activity circulation in the blood pool or the uptake in hematological-related organs (e. g. spleen) has to be separated from the medium-term radiation effect on the active bone marrow itself.

Concerning the absolute magnitude of the bone marrow absorbed dose, bone lesion load, prolonged whole-body activity circulation, and a high time-integrated tumor uptake were identified as risk factors (see section 3.3.2 [58]), which can be employed to identify patients for further pre-therapeutic image-based active bone marrow localization. For instance, a high lesion load in combination with a high lesion SUV in the pre-therapeutic PET, but also a decreased excretion rate with regard to the pre-therapeutic evaluation of kidney function might justify additional image-based active bone marrow localization. Similar findings have already been reported for Lu-177-PRRT [12]. Image-based active bone marrow localization can be performed, e. g., via Tc-99m-anti-granulocyte scintigraphy, as described in the scope of section 3.3.2 [58] for a small sub-cohort of patients, or via magnetic resonance imaging (MRI) [3, 11, 100]. High-resolution MRI-based active bone marrow localization, in combination with PET imaging or improved Lu-177 SPECT imaging could further reduce the artificial spatial-resolution-related over-

lap between active bone marrow and lesion uptake. Hybrid PET/MR imaging could be of interest to reduce co-registration errors between active bone marrow and lesion localization. However, the exact method for image-based active bone marrow localization should be feasible for several patients per week and easy to be integrated in the routine therapy procedure.

S-value bone marrow absorbed doses showed a strong and significant correlation with both, time-integrated ROB retention and tumor uptake [58], while results from study 3.3.1 and 3.3.2 indicate only a weak to moderate correlation with the patient-specific bone lesion load, depending on the exact patient cohort and segmentation method. Thus, in the absence of severe metastases and other therapy-related or hematological risk factors, efficient hybrid SPECT-planar S-value bone marrow ID as proposed in section 3.2.2 [51] could be suitable to estimate bone marrow absorbed doses within defined uncertainty limits. Ongoing studies shall aim at finding appropriate stratification thresholds of risk parameters (e. g. SUV cut-off to identify critical lesion uptake), and, as emphasized, appropriate absorbed dose constraints. Nonetheless, also for Monte-Carlo-based bone marrow dosimetry the optimized measurement scheme proposed in section 3.2.2 [51] allows to effectively gather the Lu-177 TAC information in all relevant accumulating regions.

High-resolution 3D absorbed dose estimation using Monte Carlo techniques is characterized by a strongly elevated computational demand compared to classical S-value-based bone marrow ID. However, via usage of automatized CT, PET, and SPECT segmentation algorithms in combination with computing clusters, Monte Carlo results using the proposed template-based approach can be obtained within one day, which is in principal acceptable regarding the time scale of treatment planning and evaluation during nuclear medicine RT. Future studies will additionally aim to enable absorbed dose kernels methods, which could allow for 3D bone marrow ID within several minutes [108, 109]. The proposed weighting-based Monte Carlo workflow for 3D bone marrow ID already compromises accuracy and efficiency for clinical applications, compared to existing time-consuming hybrid Monte-Carlo-workflows, which switch the simulation between the macroscopic and microscopic representation of both, patient anatomy and skeletal system (paired-image radiation transport (PIRT) model) [113]. However, Lee et al. demonstrated for selected skeletal sites that voxel-wise weighting-based methods (mass-energy-absorption-coefficient (MEAC) methods) are in good agreement with PIRT results for the typical γ -energy range of radionuclides employed in RT [85]. These results can also be transferred to typical RT β -energies, as absorbed dose deposition by photons occurs via release of secondary electrons.

So far, the application of PIRT models was limited to phantoms or to information gathered from cadavers, for which the exact structure of the skeletal micro-environment was well known. Regarding clinical conditions, the patient-specific 3D spongiosa structure is not available for the entire skeleton due to the limited resolution of state-of-the-art in vivo imaging modalities. Patient-specific active marrow cellularities, i. e. the hematologically active volume fraction of the overall bone marrow mixture, could be derived from biopsies, however, these imply a large patient burden, and are further only representative regarding the bone marrow characteristics at the direct intervention location. In a first step, a clinically feasible method employing region-wise reference mass fractions of active and inactive bone marrow, as well as hard bone, is proposed [58]. In a second step, voxel-wise patient-specific mass fractions could be derived from dual-energy CT imaging, as already performed during phantom experiments [48]. Therefore, future studies should aim at understanding the typical time scale of detectable PSMA-avid lesions, active bone marrow displacement, and CT-detectable and lesion-induced sclerosing processes (Figure 4.1).

A similar dosimetry selection scheme, as proposed for bone marrow dosimetry during Lu-177-PSMA therapy, was established at the nuclear medicine department of the University Hospital Munich to identify patients for efficient single-SPECT kidney dosimetry for both, Lu-177-PRRT and Lu-177-PSMA therapy. Single-SPECT dosimetry can be considered as suitable if no impairment of the kidney excretion is

Table 4.1: Dosimetry results for the simulation study presented in Figure 4.2.

VOI	Absorbed dose 6 min/bed [Gy]	Absorbed dose 3 min/bed [Gy]
Kidneys	2.1	2.1
Liver	0.2	0.2
Spleen	0.3	0.3
Bone lesions	8.3	7.8

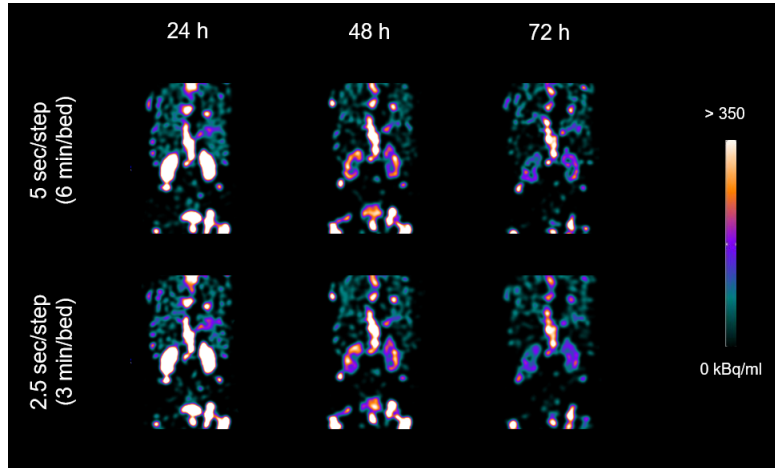


Figure 4.2: Simulation study to investigate the feasibility of fast whole-body Lu-177 SPECT imaging based on the data of an exemplary mCRPC patient (6 GBq Lu-177-DKFZ-PSMA-617). For the lower row, a whole-body Lu-177 SPECT acquisition within 15 minutes was simulated. Respective dosimetry is provided in Table 4.1.

expected, and if precautions such as amino acid infusion for Lu-177-PRRT are undertaken [13, 15, 106, 123]. For mCRPC patients with a high initial lesion load, therapy response might initiate severe changes of the whole-body accumulation pattern (see sections 3.2.1 and 3.3.1) [56, 57, 59, 61, 62]. Thus, for mCRPC patients a more frequent sequential SPECT imaging is advisable (e. g. every second cycle), than for NET patients (e. g. every fourth cycle) [133]. As for NET patients with normal kidney excretion recent studies demonstrated no severe incidence of kidney toxicity, even standard single-SPECT imaging in combination with population-based therapy-specific pharmacokinetic information could be feasible, if respective uncertainty limits are acceptable to detect possible organ toxicities [67, 106]. Single-SPECT dosimetry was found to yield an increased uncertainty for lesion absorbed dose estimates. However, the current clinical procedure in Lu-177-based RT of NET and mCRPC is rather driven by the concern to limit the absorbed dose in OAR, than directly aims at applying a prescribed lesion absorbed dose. More precise, multiple cycles of a standardized amount of activity are applied, while the decision to undergo the next therapy cycle is dependent on a pre-therapy assessment of clinical parameters (e. g. blood element counts, kidney function, PET-detectable PSMA-avid orsstr-avid lesions), in combination with a OAR dosimetry of the preceding therapy cycles, if available [110, 123]. By contrast, due to the high uncertainty of SPECT-based lesion dosimetry, and as ongoing efforts still have to identify all relevant influencing factors on therapy response for Lu-177-based RT, the knowledge of absorbed-dose-response-relationships and appropriate lesion absorbed dose prescriptions is still fragmentary [14, 49, 50, 88]. Although, from a dosimetric point of perspective, the uncertainty of SPECT-based kidney absorbed doses can be judged as lower compared to that of lesion dosimetry [66], finding appropriate kidney absorbed dose constraints for Lu-177-based RT is still a matter of interest. So far applied absorbed dose constraints are derived from markedly different treatment regimes, such as external beam therapy. Further, risk factors associated with nephrotoxicity, and in particular the relevant underlying

sub-cellular mechanisms have not been fully understood, yet [15, 63, 123].

Improving Lu-177 SPECT imaging is crucial to allow for appropriate response assessment, which in turn supports the identification of clinical risk and response factors. In this context, Figure 4.2 and Table 4.1 present the initial attempts to provide fast whole-body Lu-177 SPECT imaging, which shall allow for a high-quality response assessment for a large part of the patient body without sacrificing patient comfort.

Bibliography

- [1] A. Afshar-Oromieh, J. W. Babich, C. Kratochwil, F. L. Giesel, M. Eisenhut, K. Kopka, and U. Haberkorn. “The rise of PSMA ligands for diagnosis and therapy of prostate cancer”. In: *Journal of Nuclear Medicine* 57.Supplement 3 (2016), 79S–89S.
- [2] A. Afshar-Oromieh, H. Hetzheim, C. Kratochwil, M. Benesova, M. Eder, O. C. Neels, M. Eisenhut, W. Kübler, T. Holland-Letz, F. L. Giesel, et al. “The theranostic PSMA ligand PSMA-617 in the diagnosis of prostate cancer by PET/CT: biodistribution in humans, radiation dosimetry, and first evaluation of tumor lesions”. In: *Journal of Nuclear Medicine* 56.11 (2015), pp. 1697–1705.
- [3] A. Agool, A. W. Glaudemans, H. H. Boersma, R. A. Dierckx, E. Vellenga, and R. H. Slart. “Radionuclide imaging of bone marrow disorders”. In: *European journal of nuclear medicine and molecular imaging* 38.1 (2011), pp. 166–178.
- [4] A. Ahnesjö. “Collapsed cone convolution of radiant energy for photon dose calculation in heterogeneous media”. In: *Medical physics* 16.4 (1989), pp. 577–592.
- [5] H. O. Anger. “Scintillation camera”. In: *Review of scientific instruments* 29.1 (1958), pp. 27–33.
- [6] E. C. Ao, N.-Y. Wu, S.-J. Wang, N. Song, and G. S. Mok. “Improved dosimetry for targeted radionuclide therapy using nonrigid registration on sequential SPECT images”. In: *Medical physics* 42.2 (2015), pp. 1060–1070.
- [7] D. L. Bailey and J. Humm. *Nuclear medicine physics: a handbook for teachers and students*. IAEA, 2014.
- [8] R. P. Baum and H. R. Kulkarni. “THERANOSTICS: from molecular imaging using Ga-68 labeled tracers and PET/CT to personalized radionuclide therapy-the Bad Berka experience”. In: *Theranostics* 2.5 (2012), p. 437.
- [9] R. P. Baum, H. R. Kulkarni, C. Schuchardt, A. Singh, M. Wirtz, S. Wiessalla, M. Schottelius, D. Mueller, I. Klette, and H.-J. Wester. “Lutetium-177 PSMA radioligand therapy of metastatic castration-resistant prostate cancer: safety and efficacy”. In: *Journal of Nuclear Medicine* (2016), jnumed–115.
- [10] M. Bé, V Chisté, C Duiieu, E Browne, V Chechev, N Kuzmenko, R Helmer, A Nichols, E Schönfeld, and R Dersch. “Table of radionuclides (Vol. 2-A= 151 to 242)”. In: *Bureau international des poids et mesures, Pavillon de Breteuil, Sèvres* (2004).
- [11] B. C. V. Berg, J. Malghem, F. E. Lecouvet, and B. Maldague. “Magnetic resonance imaging of the normal bone marrow”. In: *Skeletal radiology* 27.9 (1998), pp. 471–483.
- [12] H. Bergsma, M. W. Konijnenberg, B. L. Kam, J. J. Teunissen, P. P. Kooij, W. W. de Herder, G. J. Franssen, C. H. van Eijck, E. P. Krenning, and D. J. Kwekkeboom. “Subacute haematotoxicity after PRRT with 177 Lu-DOTA-octreotate: prognostic factors, incidence and course”. In: *European journal of nuclear medicine and molecular imaging* 43.3 (2016), pp. 453–463.

- [13] L. Bodei, M. Cremonesi, M. Ferrari, M. Pacifici, C. M. Grana, M. Bartolomei, S. M. Baio, M. Sansovini, and G. Paganelli. “Long-term evaluation of renal toxicity after peptide receptor radionuclide therapy with 90 Y-DOTATOC and 177 Lu-DOTATATE: the role of associated risk factors”. In: *European journal of nuclear medicine and molecular imaging* 35.10 (2008), pp. 1847–1856.
- [14] L. Bodei, M. S. Kidd, A. Singh, W. A. van der Zwan, S. Severi, I. A. Drozdov, J. Cwikla, R. P. Baum, D. J. Kwekkeboom, G. Paganelli, et al. “PRRT genomic signature in blood for prediction of 177 Lu-octreotate efficacy”. In: *European journal of nuclear medicine and molecular imaging* 45.7 (2018), pp. 1155–1169.
- [15] L. Bodei, M. Kidd, G. Paganelli, C. M. Grana, I. Drozdov, M. Cremonesi, C. Lepensky, D. J. Kwekkeboom, R. P. Baum, E. P. Krenning, et al. “Long-term tolerability of PRRT in 807 patients with neuroendocrine tumours: the value and limitations of clinical factors”. In: *European journal of nuclear medicine and molecular imaging* 42.1 (2015), pp. 5–19.
- [16] W. E. Bolch, L. G. Bouchet, J. S. Robertson, B. W. Wessels, J. A. Siegel, R. W. Howell, A. K. Erdi, B. Aydogan, S. Costes, E. E. Watson, et al. “MIRD pamphlet no. 17: the dosimetry of nonuniform activity distributions—radionuclide S values at the voxel level”. In: *Journal of Nuclear Medicine* 40.1 (1999), 11S–36S.
- [17] W. E. Bolch, K. F. Eckerman, G. Sgouros, and S. R. Thomas. “MIRD pamphlet no. 21: a generalized schema for radiopharmaceutical dosimetry - standardization of nomenclature”. In: *Journal of Nuclear Medicine* 50.3 (2009), pp. 477–484.
- [18] S. J. Bonnema and L. Hegedüs. “Radioiodine therapy in benign thyroid diseases: effects, side effects, and factors affecting therapeutic outcome”. In: *Endocrine reviews* 33.6 (2012), pp. 920–980.
- [19] F. Botta, A. Mairani, R. F. Hobbs, A. V. Gil, M. Pacilio, K. Parodi, M. Cremonesi, M. A. C. Pérez, A. Di Dia, M. Ferrari, et al. “Use of the FLUKA Monte Carlo code for 3D patient-specific dosimetry on PET-CT and SPECT-CT images”. In: *Physics in Medicine & Biology* 58.22 (2013), p. 8099.
- [20] J. F. Brosch, A. Gosewisch, A. Delker, L. Vomacka, P. Bartenstein, H. Ilhan, A. Todica, and G. Boening. “Comparison of a simplified quantitative yttrium-90 bremsstrahlung SPECT reconstruction with yttrium-90 PET in terms of quantification for dosimetry of SIR-therapy in the liver”. In: *European journal of nuclear medicine and molecular imaging* 45.Suppl. 1 (2018).
- [21] J. F. Brosch, A. Gosewisch, A. Delker, L. Vomacka, P. Bartenstein, A. Todica, H. Ilhan, and G. Boening. “Investigation of a simplified quantitative yttrium-90 bremsstrahlung SPECT reconstruction by usage of background compensation and patient-specific calibration factors for yttrium-90 SIRT dosimetry”. In: *European journal of nuclear medicine and molecular imaging* 45.Suppl. 1 (2018).
- [22] J. Brosch, A. Gosewisch, H. von Zimmermann, L. Kaiser, P. Barstenstein, A. Todica, H. Ilhan, and G. Böning. “Evaluation von Yttrium-90-PET und Yttrium-90-SPECT Phantommessungen angepasst an Messbedingungen von 20 SIRT Patienten”. In: *Nuklearmedizin* 58.02 (2019).
- [23] J. Brosch, A. Gosewisch, L. Kaiser, P. Bartenstein, H. Ilhan, A. Todica, and G. Boening. “3D image-based dosimetry for Yttrium-90 SIR-therapy of HCC: comparison of three different techniques”. In: *Journal of Nuclear Medicine* 60.supplement 1 (2019).
- [24] P. P. Bruyant. “Analytic and iterative reconstruction algorithms in SPECT”. In: *Journal of Nuclear Medicine* 43.10 (2002), pp. 1343–1358.

- [25] J. A. Carrasquillo. “Alpha Radionuclide Therapy: Principles and Applications to NETs”. In: (2017), pp. 429–445.
- [26] L. Cheng, R. F. Hobbs, P. W. Segars, G. Sgouros, and E. C. Frey. “Improved dose–volume histogram estimates for radiopharmaceutical therapy by optimizing quantitative SPECT reconstruction parameters”. In: *Physics in Medicine & Biology* 58.11 (2013), p. 3631.
- [27] S. Chiavassa, M. Bardiès, F. Guiraud-Vitau, D. Bruel, J.-R. Jourdain, D. Franck, and I. Aubineau-Lanièce. “OEDIPE: a personalized dosimetric tool associating voxel-based models with MCNPX”. In: *Cancer biotherapy & radiopharmaceuticals* 20.3 (2005), pp. 325–332.
- [28] S. Y. Chun, J. A. Fessler, and Y. K. Dewaraja. “Correction for collimator-detector response in SPECT using point spread function template”. In: *IEEE transactions on medical imaging* 32.2 (2012), pp. 295–305.
- [29] M. Cremonesi, M. Ferrari, L. Bodei, G. Tosi, and G. Paganelli. “Dosimetry in peptide radionuclide receptor therapy: a review”. In: *Journal of nuclear medicine* 47.9 (2006), pp. 1467–1475.
- [30] M. D'Arienzo, M. Cazzato, M. L. Cozzella, M. Cox, M. D'Andrea, A. Fazio, A. Fenwick, G. Iaccarino, L. Johansson, L. Strigari, et al. “Gamma camera calibration and validation for quantitative SPECT imaging with ^{177}Lu ”. In: *Applied Radiation and Isotopes* 112 (2016), pp. 156–164.
- [31] A. Delker, A. Gosewisch, S. Rieger, H. Ilhan, W. Fendler, F. J. Gildehaus, P. Bartenstein, and G. Böning. “Dosimetrie bei der Lu-177-PSMA Therapie von Patienten mit metastasiertem kastrationsresistentem Prostatakarzinom: Ein Vergleich von 3D SPECT und 2D planaren Szintigraphien”. In: *Nuklearmedizin* 56.02 (2017).
- [32] A. Delker, A. Gosewisch, S. Rieger, H. Ilhan, W. Fendler, F. Gildehaus, P. Bartenstein, and G. Böning. “Dosimetry for Lu-177-PSMA therapy of patients with mCRPC: A comparison of 3D SPECT and 2D planar methods”. In: *European Journal of Nuclear Medicine and Molecular Imaging* 43.Suppl. 1 (2016).
- [33] A. Delker, W. P. Fendler, C. Kratochwil, A. Brunegraf, A. Gosewisch, F. J. Gildehaus, S. Tritschler, C. G. Stief, K. Kopka, U. Haberkorn, P. Bartenstein, and G. Böning. “Dosimetry for ^{177}Lu -DKFZ-PSMA-617: a new radiopharmaceutical for the treatment of metastatic prostate cancer”. In: *European journal of nuclear medicine and molecular imaging* 43.1 (2016), pp. 42–51.
- [34] A. Delker, H. Ilhan, C. Zach, J. Brosch, F. J. Gildehaus, S. Lehner, P. Bartenstein, and G. Böning. “The influence of early measurements onto the estimated kidney dose in [^{177}Lu][DOTA 0, Tyr 3] Octreotate peptide receptor radiotherapy of neuroendocrine tumors”. In: *Molecular Imaging and Biology* 17.5 (2015), pp. 726–734.
- [35] Y. K. Dewaraja, E. C. Frey, G. Sgouros, A. B. Brill, P. Roberson, P. B. Zanzonico, and M. Ljungberg. “MIRD pamphlet no. 23: quantitative SPECT for patient-specific 3-dimensional dosimetry in internal radionuclide therapy”. In: *Journal of Nuclear Medicine* 53.8 (2012), pp. 1310–1325.
- [36] Y. K. Dewaraja, K. F. Koral, and J. A. Fessler. “Regularized reconstruction in quantitative SPECT using CT side information from hybrid imaging”. In: *Physics in Medicine & Biology* 55.9 (2010), p. 2523.
- [37] U. Eberlein, J. H. Bröer, C. Vandevoorde, P. Santos, M. Bardiès, K. Bacher, D. Nosske, and M. Lassmann. “Biokinetics and dosimetry of commonly used radiopharmaceuticals in diagnostic nuclear medicine—a review”. In: *European journal of nuclear medicine and molecular imaging* 38.12 (2011), pp. 2269–2281.
- [38] R. Eisner, T. Noever, D. Nowak, W. Carlson, D. Dunn, J. Oates, K. Cloninger, H. Liberman, and R. Patterson. “Patient motion during SPECT imaging”. In: *J Nucl Med* 28 (1987), pp. 97–101.

- [39] L. Emmett, K. Willowson, J. Violet, J. Shin, A. Blanksby, and J. Lee. “Lutetium 177 PSMA radionuclide therapy for men with prostate cancer: a review of the current literature and discussion of practical aspects of therapy”. In: *Journal of medical radiation sciences* 64.1 (2017), pp. 52–60.
- [40] W. P. Fendler, S. Reinhardt, H. Ilhan, A. Delker, G. Böning, F. J. Gildehaus, C. Stief, P. Bartenstein, C. Gratzke, S. Lehner, and A. Rominger. “Preliminary experience with dosimetry, response and patient reported outcome after 177Lu-PSMA-617 therapy for metastatic castration-resistant prostate cancer”. In: *Oncotarget* 8.2 (2017), p. 3581.
- [41] L. Fiedler, M. Kellner, A. Gosewisch, G. Böning, S. Lindner, P. Bartenstein, R. Zeidler, and F. Gildehaus. “Evaluation of Lu-177 Labelled 6A10 Fab as Carbonic Anhydrase 12 Targeting Agent”. In: *European journal of nuclear medicine and molecular imaging* 44.Suppl. 2 (2017).
- [42] L. Fiedler, M. Kellner, A. Gosewisch, R. Oos, G. Böning, S. Lindner, N. Albert, P. Bartenstein, H.-J. Reulen, R. Zeidler, and F. J. Gildehaus. “Evaluation of 177Lu[Lu]-CHX-A-DTPA-6A10 Fab as a radioimmunotherapy agent targeting carbonic anhydrase XII”. In: *Nuclear medicine and biology* 60 (2018), pp. 55–62.
- [43] J. Fleming. “A technique for the absolute measurement of activity using a gamma camera and computer”. In: *Physics in Medicine & Biology* 24.1 (1979), p. 176.
- [44] F. Forrer, E. P. Krenning, P. P. Kooij, B. F. Bernard, M. Konijnenberg, W. H. Bakker, J. J. Teunissen, M. de Jong, K. van Lom, W. W. de Herder, et al. “Bone marrow dosimetry in peptide receptor radionuclide therapy with [177 Lu-DOTA 0, Tyr 3] octreotate”. In: *European journal of nuclear medicine and molecular imaging* 36.7 (2009), p. 1138.
- [45] E. C. Frey, J. L. Humm, and M. Ljungberg. “Accuracy and precision of radioactivity quantification in nuclear medicine images”. In: 42.3 (2012), pp. 208–218.
- [46] M. Garkavij, M. Nickel, K. Sjögren-Gleisner, M. Ljungberg, T. Ohlsson, K. Wingårdh, S.-E. Strand, and J. Tennvall. “177Lu-[DOTA0, Tyr3] octreotate therapy in patients with disseminated neuroendocrine tumors: Analysis of dosimetry with impact on future therapeutic strategy”. In: *Cancer* 116.S4 (2010), pp. 1084–1092.
- [47] K. S. Gleisner, E. Spezi, P. Solny, P. M. Gabina, F. Cicone, C. Stokke, C. Chiesa, M. Paphiti, B. Brans, M. Sandström, et al. “Variations in the practice of molecular radiotherapy and implementation of dosimetry: results from a European survey”. In: *EJNMMI physics* 4.1 (2017), p. 28.
- [48] M. M. Goodsitt, A. Shenoy, J. Shen, D. Howard, M. J. Schipper, S. Wilderman, E. Christodoulou, S. Y. Chun, and Y. K. Dewaraja. “Evaluation of dual energy quantitative CT for determining the spatial distributions of red marrow and bone for dosimetry in internal emitter radiation therapy”. In: *Medical physics* 41.5 (2014), p. 051901.
- [49] A. Gosewisch, M. Cachovan, H. Ilhan, P. Bartenstein, A. H. Vija, and G. Boening. “Investigation of the effect of patient motion onto 3D dose estimates in Lu-177-PSMA therapy using Siemens xSPECT Quant reconstruction with integrated motion correction and Dosimetry Research Tool”. In: *European journal of nuclear medicine and molecular imaging* 45.Suppl. 1 (2018).
- [50] A. Gosewisch, M. Cachovan, H. Ilhan, P. Bartenstein, A. H. Vija, and G. Böning. “Untersuchung des Effekts von Patientenbewegung auf die 3D Dosimetrie für die Lu-177-PSMA Therapie mittels Siemens xSPECT Quant mit integrierter Bewegungskorrektur sowie Siemens Dosimetry Research Tool”. In: *Nuklearmedizin* 58.02 (2019).

- [51] A. Gosewisch, A. Delker, S. Tattenberg, H. Ilhan, A. Todica, J. Brosch, L. Vomacka, A. Brunegraf, F. J. Gildehaus, S. Ziegler, P. Bartenstein, and G. Böning. “Patient-specific image-based bone marrow dosimetry in Lu-177-[DOTA0, Tyr3]-Octreotate and Lu-177-DKFZ-PSMA-617 therapy: investigation of a new hybrid image approach”. In: *EJNMMI research* 8.1 (2018), p. 76.
- [52] A. Gosewisch, A. Delker, S. Tattenberg, L. Vomacka, A. Brunegraf, F. J. Gildehaus, P. Bartenstein, and G. Böning. “Investigation of a hybrid image approach and a reduction in the number of blood samples for a decreased clinical workload for patient-specific bone marrow dosimetry in Lu-177-DKFZ-PSMA-617 therapy”. In: *European journal of nuclear medicine and molecular imaging* 43.Suppl. 1 (2016).
- [53] A. Gosewisch, A. Delker, S. Tattenberg, L. Vomacka, H. Ilhan, F. J. Gildehaus, A. Brunegraf, P. Bartenstein, and G. Böning. “Entwurf eines effizienten Messprotokolls zur patienten-spezifischen Knochenmarksdosimetrie in der Lu-177-PSMA-DKFZ-617 Therapie”. In: *Nuklearmedizin* 56.02 (2017).
- [54] A. Gosewisch, A. Delker, L. Vomacka, W. Fendler, A. Brunegraf, F. J. Gildehaus, F. Botta, A. Mairani, K. Parodi, P. Bartenstein, and G. Böning. “Monte Carlo basierte Risikoabschätzung der Photonendosis auf das aktive Knochenmark bei der Lu-177-DKFZ-PSMA-617 Therapie”. In: *Nuklearmedizin* 55.02 (2016).
- [55] A. Gosewisch, A. Delker, L. Vomacka, W. Fendler, A. Brunegraf, F. J. Gildehaus, A. Mairani, K. Parodi, P. Bartenstein, and G. Böning. “Estimation of local photon dose to active bone marrow in Lu-177 PSMA PRRT therapy using patient-specific Monte Carlo simulations”. In: *European journal of nuclear medicine and molecular imaging* 42.Suppl. 1 (2015).
- [56] A. Gosewisch, L. Ermoschkin, H. Ilhan, A. Todica, L. Vomacka, P. Bartenstein, and G. Böning. “Patient-specific pharmacokinetics and dosimetry over multiple therapy cycles during Lu-177-based radionuclide therapy: a study for Lu-177-DOTATATE and Lu-177-PSMA”. In: *European journal of nuclear medicine and molecular imaging* 44.Suppl. 2 (2017).
- [57] A. Gosewisch, L. Ermoschkin, H. Ilhan, A. Todica, L. Vomacka, P. Bartenstein, and G. Böning. “Patienten-Spezifische Pharmakokinetik und Dosimetrie über multiple Therapiezyklen bei der Lu-177-PSMA oder Lu-177-DOTATATE Radionuklidtherapie”. In: *Nuklearmedizin* 57.02 (2018).
- [58] A. Gosewisch, H. Ilhan, S. Tattenberg, A. Mairani, K. Parodi, J. Brosch, L. Kaiser, F. J. Gildehaus, A. Todica, S. Ziegler, P. Bartenstein, and G. Böning. “3D Monte Carlo bone marrow dosimetry for Lu-177-PSMA therapy with guidance of non-invasive 3D localization of active bone marrow via Tc-99m-anti-granulocyte antibody SPECT/CT”. In: *EJNMMI research* 9.1 (2019), p. 76.
- [59] A. Gosewisch, H. Ilhan, A. Todica, J. Brosch, L. Kaiser, P. Bartenstein, and G. Böning. “The role of kidneys and bone marrow as critical organs during Lu-177-PSMA-DKFZ-617 therapy depending on the patient-specific tumor load”. In: *Journal of Nuclear Medicine* 60.supplement 1 (2019).
- [60] A. Gosewisch, H. Ilhan, L. Vomacka, and G. Böning. “Dosimetrie bei der Radionuklidtherapie mit Lu-177”. In: *Der Nuklearmediziner* 41.01 (2018), pp. 69–80.
- [61] A. Gosewisch, H. Ilhan, C. Zach, J. Brosch, L. Kaiser, A. Todica, P. Bartenstein, and G. Böning. “Relevanz von Nieren und Knochenmark als Risikoorgane bei der Lu-177-PSMA Therapie für Patienten mit hoher Tumorlast”. In: *Nuklearmedizin* 58.02 (2019).
- [62] A. Gosewisch, H. Ilhan, C. Zach, A. Todica, J. Brosch, L. Vomacka, P. Bartenstein, and G. Böning. “Relevance of kidneys and bone marrow as dose-limiting organs during Lu-177-PSMA-DKFZ-617 therapy for patients with high bone tumor burden”. In: *European journal of nuclear medicine and molecular imaging* 45.Suppl. 1 (2018).

- [63] A. Green, A. Flynn, R. B. Pedley, J. Dearling, and R. Begent. “Nonuniform absorbed dose distribution in the kidney: the influence of organ architecture”. In: *Cancer Biotherapy and Radiopharmaceuticals* 19.3 (2004), pp. 371–377.
- [64] J. Grimes and A. Celler. “Comparison of internal dose estimates obtained using organ-level, voxel S value, and Monte Carlo techniques”. In: *Medical physics* 41.9 (2014), p. 092501.
- [65] S. K. Gupta, S. Singla, P. Thakral, and C. Bal. “Dosimetric analyses of kidneys, liver, spleen, pituitary gland, and neuroendocrine tumors of patients treated with ^{177}Lu -DOTATATE”. In: *Clinical nuclear medicine* 38.3 (2013), pp. 188–194.
- [66] J. Gustafsson, G. Brodin, M. Cox, M. Ljungberg, L. Johansson, and K. S. Gleisner. “Uncertainty propagation for SPECT/CT-based renal dosimetry in ^{177}Lu peptide receptor radionuclide therapy”. In: *Physics in Medicine & Biology* 60.21 (2015), p. 8329.
- [67] H. Hänscheid, C. Lapa, A. K. Buck, M. Lassmann, and R. A. Werner. “Dose mapping after endoradiotherapy with ^{177}Lu -DOTATATE/DOTATOC by a single measurement after 4 days”. In: *Journal of Nuclear Medicine* 59.1 (2018), pp. 75–81.
- [68] B. He and E. C. Frey. “The impact of 3D volume of interest definition on accuracy and precision of activity estimation in quantitative SPECT and planar processing methods”. In: *Physics in Medicine & Biology* 55.12 (2010), p. 3535.
- [69] B. He, R. L. Wahl, G. Sgouros, Y. Du, H. Jacene, W. R. Kasecamp, I. Flinn, R. J. Hammes, J. Bianco, B. Kahl, et al. “Comparison of organ residence time estimation methods for radioimmunotherapy dosimetry and treatment planning-patient studies”. In: *Medical physics* 36.5 (2009), pp. 1595–1601.
- [70] C. Hindorf, G. Glatting, C. Chiesa, O. Lindén, and G. Flux. “EANM Dosimetry Committee guidelines for bone marrow and whole-body dosimetry”. In: *European journal of nuclear medicine and molecular imaging* 37.6 (2010), pp. 1238–1250.
- [71] M. Hough, P. Johnson, D. Rajon, D. Jokisch, C. Lee, and W. Bolch. “An image-based skeletal dosimetry model for the ICRP reference adult male internal electron sources”. In: *Physics in Medicine & Biology* 56.8 (2011), p. 2309.
- [72] B. F. Hutton, I. Buvat, and F. J. Beekman. “Review and current status of SPECT scatter correction”. In: *Physics in Medicine & Biology* 56.14 (2011), R85.
- [73] H. Ilhan, S. Lindner, A. Todica, C. C. Cyran, R. Tiling, C. J. Auernhammer, C. Spitzweg, S. Boeck, M. Unterrainer, F. J. Gildehaus, G. Böning, K. Jurkschat, C. Wängler, B. Wängler, R. Schirrmacher, and P. Bartenstein. “Biodistribution and first clinical results of ^{18}F -SiFalin-TATE PET: a novel ^{18}F -labeled somatostatin analog for imaging of neuroendocrine tumors”. In: *European Journal of Nuclear Medicine and Molecular Imaging* (2019), pp. 1–11.
- [74] H. Ilhan, A. Todica, S. Lindner, G. Böning, A. Gosewisch, C. Wängler, B. Wängler, R. Schirrmacher, and P. Bartenstein. “First-in-human ^{18}F -SiFalin-TATE PET/CT for NET imaging and theranostics”. In: *European journal of nuclear medicine and molecular imaging* (2019), pp. 1–2.
- [75] W. Jentzen. “Experimental investigation of factors affecting the absolute recovery coefficients in iodine-124 PET lesion imaging”. In: *Physics in Medicine & Biology* 55.8 (2010), p. 2365.
- [76] L. Jönsson, M. Ljungberg, and S.-E. Strand. “Evaluation of accuracy in activity calculations for the conjugate view method from Monte Carlo simulated scintillation camera images using experimental data in an anthropomorphic phantom”. In: *Journal of Nuclear Medicine* 46.10 (2005), pp. 1679–1686.

- [77] N. Khajornjiraphan, N. A. Thu, and P. K. H. Chow. “Yttrium-90 microspheres: a review of its emerging clinical indications”. In: *Liver Cancer* 4.1 (2015), pp. 6–15.
- [78] K. F. Koral, Y. Dewaraja, J. Li, Q. Lin, D. D. Regan, K. R. Zasadny, S. G. Rommelfanger, I. R. Francis, M. S. Kaminski, and R. L. Wahl. “Update on hybrid conjugate-view SPECT tumor dosimetry and response in ^{131}I -tositumomab therapy of previously untreated lymphoma patients”. In: *Journal of Nuclear Medicine* 44.3 (2003), pp. 457–464.
- [79] S. D. Kost, Y. K. Dewaraja, R. G. Abramson, and M. G. Stabin. “VIDA: a voxel-based dosimetry method for targeted radionuclide therapy using Geant4”. In: *Cancer Biotherapy and Radiopharmaceuticals* 30.1 (2015), pp. 16–26.
- [80] C. Kratochwil, F. Bruchertseifer, F. L. Giesel, M. Weis, F. A. Verburg, F. Mottaghy, K. Kopka, C. Apostolidis, U. Haberkorn, and A. Morgenstern. “ ^{225}Ac -PSMA-617 for PSMA-targeted α -radiation therapy of metastatic castration-resistant prostate cancer”. In: *Journal of Nuclear Medicine* 57.12 (2016), pp. 1941–1944.
- [81] C. Kratochwil, F. L. Giesel, M. Stefanova, M. Benešová, M. Bronzel, A. Afshar-Oromieh, W. Mier, M. Eder, K. Kopka, and U. Haberkorn. “PSMA-targeted radionuclide therapy of metastatic castration-resistant prostate cancer with ^{177}Lu -labeled PSMA-617”. In: *Journal of Nuclear Medicine* 57.8 (2016), pp. 1170–1176.
- [82] A. Z. Kyme, B. F. Hutton, R. L. Hatton, D. W. Skerrett, and L. R. Barnden. “Practical aspects of a data-driven motion correction approach for brain SPECT”. In: *IEEE transactions on medical imaging* 22.6 (2003), pp. 722–729.
- [83] D. S. Lalush and B. M. Tsui. “Simulation evaluation of Gibbs prior distributions for use in maximum a posteriori SPECT reconstructions”. In: *IEEE transactions on Medical Imaging* 11.2 (1992), pp. 267–275.
- [84] N. Lanconelli, M. Pacilio, S. L. Meo, F. Botta, A. Di Dia, L. A. T. Aroche, M. A. C. Pérez, and M. Cremonesi. “A free database of radionuclide voxel S values for the dosimetry of nonuniform activity distributions”. In: *Physics in Medicine & Biology* 57.2 (2012), p. 517.
- [85] C. Lee, C. Lee, A. P. Shah, and W. E. Bolch. “An assessment of bone marrow and bone endosteum dosimetry methods for photon sources”. In: *Physics in Medicine & Biology* 51.21 (2006), p. 5391.
- [86] M. Ljungberg, A. Celler, M. W. Konijnenberg, K. F. Eckerman, Y. K. Dewaraja, and K. Sjögreen-Gleisner. “MIRD pamphlet no. 26: joint EANM/MIRD guidelines for quantitative ^{177}Lu SPECT applied for dosimetry of radiopharmaceutical therapy”. In: *Journal of nuclear medicine* 57.1 (2016), pp. 151–162.
- [87] M. Ljungberg, E. Frey, K. Sjögreen, X. Liu, Y. Dewaraja, and S.-E. Strand. “3D absorbed dose calculations based on SPECT: evaluation for ^{111}In / ^{90}Y therapy using Monte Carlo simulations”. In: *Cancer Biotherapy and Radiopharmaceuticals* 18.1 (2003), pp. 99–107.
- [88] M. Ljungberg and K. Sjögreen-Gleisner. “The accuracy of absorbed dose estimates in tumours determined by quantitative SPECT: a Monte Carlo study”. In: *Acta oncologica* 50.6 (2011), pp. 981–989.
- [89] M. Ljungberg, K. Sjögreen, X. Liu, E. Frey, Y. Dewaraja, and S.-E. Strand. “A 3-dimensional absorbed dose calculation method based on quantitative SPECT for radionuclide therapy: evaluation for ^{131}I using Monte Carlo simulation”. In: *Journal of Nuclear Medicine* 43.8 (2002), pp. 1101–1109.
- [90] C. J. Logothetis and S.-H. Lin. “Osteoblasts in prostate cancer metastasis to bone”. In: *Nature Reviews Cancer* 5.1 (2005), p. 21.

- [91] G. Loudos, I. Tsougos, S. Boukis, N. Karakatsanis, P. Georgoulas, K. Theodorou, K. Nikita, and C. Kappas. “A radionuclide dosimetry toolkit based on material-specific Monte Carlo dose kernels”. In: *Nuclear medicine communications* 30.7 (2009), pp. 504–512.
- [92] N. Matsumoto, D. S. Berman, P. B. Kavanagh, J. Gerlach, S. W. Hayes, H. C. Lewin, J. D. Friedman, and G. Germano. “Quantitative assessment of motion artifacts and validation of a new motion-correction program for myocardial perfusion SPECT”. In: *Journal of Nuclear Medicine* 42.5 (2001), pp. 687–694.
- [93] H. R. Maxon, S. R. Thomas, V. S. Hertzberg, J. G. Kereiakes, I.-W. Chen, M. I. Sperling, and E. L. Saenger. “Relation between effective radiation dose and outcome of radioiodine therapy for thyroid cancer”. In: *New England Journal of Medicine* 309.16 (1983), pp. 937–941.
- [94] C. Morrissey and R. L. Vessella. “The role of tumor microenvironment in prostate cancer bone metastasis”. In: *Journal of cellular biochemistry* 101.4 (2007), pp. 873–886.
- [95] H. Nikjoo, S. Uehara, and D. Emfietzoglou. *Interaction of radiation with matter*. CRC press, 2016.
- [96] F. Pacini, F. Cetani, P. Miccoli, F. Mancusi, C. Ceccarelli, F. Lippi, E. Martino, and A. Pinchera. “Outcome of 309 patients with metastatic differentiated thyroid carcinoma treated with radioiodine”. In: *World Journal of Surgery* 18.4 (1994), pp. 600–604.
- [97] N. Pandit-Taskar, S. M. Larson, and J. A. Carrasquillo. “Bone-seeking radiopharmaceuticals for treatment of osseous metastases, Part 1: α therapy with ^{223}Ra -dichloride”. In: *Journal of Nuclear Medicine* 55.2 (2014), pp. 268–274.
- [98] P. Papadimitroulas, G. Loudos, G. C. Nikiforidis, and G. C. Kagadis. “A dose point kernel database using GATE Monte Carlo simulation toolkit for nuclear medicine applications: Comparison with other Monte Carlo codes”. In: *Medical physics* 39.8 (2012), pp. 5238–5247.
- [99] J. A. Patton and T. G. Turkington. “SPECT/CT physical principles and attenuation correction”. In: *Journal of nuclear medicine technology* 36.1 (2008), pp. 1–10.
- [100] J. C. Pichardo, R. J. Milner, and W. E. Bolch. “MRI measurement of bone marrow cellularity for radiation dosimetry”. In: *Journal of Nuclear Medicine* 52.9 (2011), pp. 1482–1489.
- [101] K. Rahbar, A. Afshar-Oromieh, H. Jadvar, and H. Ahmadzadehfar. “PSMA theranostics: current status and future directions”. In: *Molecular imaging* 17 (2018), p. 1536012118776068.
- [102] K. Rahbar, H. Ahmadzadehfar, C. Kratochwil, U. Haberkorn, M. Schäfers, M. Essler, R. P. Baum, H. R. Kulkarni, M. Schmidt, A. Drzezga, et al. “German multicenter study investigating ^{177}Lu -PSMA-617 radioligand therapy in advanced prostate cancer patients”. In: *Journal of Nuclear Medicine* 58.1 (2017), pp. 85–90.
- [103] A. Raza and G. K. Sood. “Hepatocellular carcinoma review: current treatment, and evidence-based medicine”. In: *World journal of gastroenterology: WJG* 20.15 (2014), p. 4115.
- [104] I. Reiser and S. Glick. *Tomosynthesis Imaging*. Taylor & Francis, 2014.
- [105] H.-J. Reulen, E. S. Molina, R. Zeidler, F. J. Gildehaus, G. Böning, A. Gosewisch, and W. Stummer. “Intracavitary radioimmunotherapy of high-grade gliomas: present status and future developments”. In: *Acta neurochirurgica* 161.6 (2019), pp. 1109–1124.
- [106] S. Rudisile, A. Gosewisch, V. Wenter, M. Unterrainer, G. Böning, F. J. Gildehaus, W. P. Fendler, C. J. Auernhammer, C. Spitzweg, P. Bartenstein, A. Todica, and H. Ilhan. “Salvage PRRT with ^{177}Lu -DOTA-octreotate in extensively pretreated patients with metastatic neuroendocrine tumor (NET): dosimetry, toxicity, efficacy, and survival”. In: *BMC cancer* 19.1 (2019), pp. 1–9.

- [107] S. Rudisile, A. Gosewisch, F. J. Gildehaus, G. Boening, C. Auernhammer, P. Bartenstein, A. Todica, and H. Ilhan. “Effectivity and Toxicity of Salvage PRRT with Lu-177 DOTATATE in patients with progressive, metastasized NET”. In: *Journal of Nuclear Medicine* 59.supplement 1 (2018).
- [108] M. Sanchez-Garcia, I. Gardin, R. Lebtahi, and A. Dieudonné. “A new approach for dose calculation in targeted radionuclide therapy (TRT) based on collapsed cone superposition: validation with 90Y”. In: *Physics in Medicine & Biology* 59.17 (2014), p. 4769.
- [109] M. Sanchez-Garcia, I. Gardin, R. Lebtahi, and A. Dieudonné. “Implementation and validation of collapsed cone superposition for radiopharmaceutical dosimetry of photon emitters”. In: *Physics in Medicine & Biology* 60.20 (2015), p. 7861.
- [110] M. Sandström, U. Garske-Román, D. Granberg, S. Johansson, C. Widström, B. Eriksson, A. Sundin, H. Lundqvist, and M. Lubberink. “Individualized dosimetry of kidney and bone marrow in patients undergoing 177Lu-DOTA-octreotate treatment”. In: *Journal of Nuclear Medicine* 54.1 (2013), pp. 33–41.
- [111] A. Saxena, L. Bester, L. Shan, M. Perera, P. Gibbs, B. Meteling, and D. L. Morris. “A systematic review on the safety and efficacy of yttrium-90 radioembolization for unresectable, chemorefractory colorectal cancer liver metastases”. In: *Journal of cancer research and clinical oncology* 140.4 (2014), pp. 537–547.
- [112] J. Seco and F. Verhaegen. *Monte Carlo techniques in radiation therapy*. CRC press, 2013.
- [113] A. P. Shah, W. E. Bolch, D. A. Rajon, P. W. Patton, and D. W. Jokisch. “A paired-image radiation transport model for skeletal dosimetry”. In: *Journal of Nuclear Medicine* 46.2 (2005), pp. 344–353.
- [114] L. A. Shepp and Y. Vardi. “Maximum likelihood reconstruction for emission tomography”. In: *IEEE transactions on medical imaging* 1.2 (1982), pp. 113–122.
- [115] J. A. Siegel, S. R. Thomas, J. B. Stubbs, M. G. Stabin, M. T. Hays, K. F. Koral, J. S. Robertson, R. W. Howell, B. W. Wessels, D. R. Fisher, et al. “MIRD pamphlet no. 16: techniques for quantitative radiopharmaceutical biodistribution data acquisition and analysis for use in human radiation dose estimates”. In: *Journal of Nuclear Medicine* 40.2 (1999), 37S–61S.
- [116] D. L. Snyder, M. I. Miller, L. J. Thomas, and D. G. Politte. “Noise and edge artifacts in maximum-likelihood reconstructions for emission tomography”. In: *IEEE transactions on medical imaging* 6.3 (1987), pp. 228–238.
- [117] M. G. Stabin. “Uncertainties in internal dose calculations for radiopharmaceuticals”. In: *Journal of nuclear medicine* 49.5 (2008), pp. 853–860.
- [118] M. G. Stabin and A. B. Brill. “State of the art in nuclear medicine dose assessment”. In: 38.5 (2008), pp. 308–320.
- [119] M. G. Stabin and M. W. Konijnenberg. “Re-evaluation of absorbed fractions for photons and electrons in spheres of various sizes”. In: *Journal of nuclear medicine* 41.1 (2000), pp. 149–160.
- [120] M. G. Stabin, X. G. Xu, M. A. Emmons, W. P. Segars, C. Shi, and M. J. Fernald. “RADAR reference adult, pediatric, and pregnant female phantom series for internal and external dosimetry”. In: *Journal of Nuclear Medicine* 53.11 (2012), pp. 1807–1813.
- [121] L. Strigari, M. Konijnenberg, C. Chiesa, M. Bardies, Y. Du, K. S. Gleisner, M. Lassmann, and G. Flux. “The evidence base for the use of internal dosimetry in the clinical practice of molecular radiotherapy”. In: *European journal of nuclear medicine and molecular imaging* 41.10 (2014), pp. 1976–1988.

- [122] J. Strosberg, G. El-Haddad, E. Wolin, A. Hendifar, J. Yao, B. Chasen, E. Mittra, P. L. Kunz, M. H. Kulke, H. Jacene, et al. “Phase 3 trial of ^{177}Lu -Dotatate for midgut neuroendocrine tumors”. In: *New England Journal of Medicine* 376.2 (2017), pp. 125–135.
- [123] A. Sundlöv, K. Sjögreen-Gleisner, J. Svensson, M. Ljungberg, T. Olsson, P. Bernhardt, and J. Tennvall. “Individualised ^{177}Lu -DOTATATE treatment of neuroendocrine tumours based on kidney dosimetry”. In: *European journal of nuclear medicine and molecular imaging* 44.9 (2017), pp. 1480–1489.
- [124] J. Svensson, T. Rydén, L. Hagmarker, J. Hemmingsson, B. Wängberg, and P. Bernhardt. “A novel planar image-based method for bone marrow dosimetry in ^{177}Lu -DOTATATE treatment correlates with haematological toxicity”. In: *EJNMMI physics* 3.1 (2016), p. 21.
- [125] A. Traino, M. Ferrari, M. Cremonesi, and M. Stabin. “Influence of total-body mass on the scaling of S-factors for patient-specific, blood-based red-marrow dosimetry”. In: *Physics in Medicine & Biology* 52.17 (2007), p. 5231.
- [126] B. Tsui, E. C. Frey, X. Zhao, D. Lalush, R. Johnston, and W. McCartney. “The importance and implementation of accurate 3D compensation methods for quantitative SPECT”. In: *Physics in medicine & biology* 39.3 (1994), p. 509.
- [127] C. F. Uribe, P. L. Esquinas, M. Gonzalez, W. Zhao, J. Tanguay, and A. Celler. “Deadtime effects in quantification of ^{177}Lu activity for radionuclide therapy”. In: *EJNMMI physics* 5.1 (2018), p. 2.
- [128] L. Vomacka, A. Delker, A. Gosewisch, W. Fendler, P. Bartenstein, and G. Boening. “Automatische Bildsegmentierung für die 3D Dosimetrie unter Verwendung eines robusten Cluster Algorithmus auf 4D SPECT Daten bei der Therapie von Patienten mit kastrationsresistentem metastasierten Prostatakarzinom mit ^{177}Lu -DKFZ-PSMA-617”. In: *Nuklearmedizin* 55.02 (2016).
- [129] L. Vomacka, A. Delker, A. Gosewisch, W. Fendler, F. J. Gildehaus, A. Brunegraf, P. Bartenstein, and G. Böning. “Automatic image segmentation for efficient 3D dosimetry with reduced influence of registration-errors and noise in ^{177}Lu -DKFZ-PSMA-617 therapy using a robust cluster algorithm on sequential SPECT data and subsequent voxel-wise re-scaling”. In: *European journal of nuclear medicine and molecular imaging* 43.Suppl. 1 (2016).
- [130] L. Vomacka, A. Gosewisch, A. Delker, W. Fendler, P. Bartenstein, and G. Boening. “Automatic image segmentation for 3D dosimetry in ^{177}Lu -DKFZ-PSMA-617 therapy of castrate-resistant metastatic prostate cancer using a robust cluster algorithm on 4D SPECT data”. In: *Journal of Nuclear Medicine* 57.supplement 2 (2016).
- [131] S. Walrand, R. Barone, S. Pauwels, and F. Jamar. “Experimental facts supporting a red marrow uptake due to radiometal transchelation in ^{90}Y -DOTATOC therapy and relationship to the decrease of platelet counts”. In: *European journal of nuclear medicine and molecular imaging* 38.7 (2011), pp. 1270–1280.
- [132] M. N. Wernick and J. N. Aarsvold. *Emission tomography: the fundamentals of PET and SPECT*. Elsevier, 2004.
- [133] K. P. Willowson, E. Eslick, H. Ryu, A. Poon, E. J. Bernard, and D. L. Bailey. “Feasibility and accuracy of single time point imaging for renal dosimetry following ^{177}Lu -DOTATATE (^{177}Lu -DOTATE) therapy”. In: *EJNMMI physics* 5.1 (2018), p. 33.
- [134] W. Zhao, P. L. Esquinas, X. Hou, C. F. Uribe, M. Gonzalez, J.-M. Beauregard, Y. K. Dewaraja, and A. Celler. “Determination of gamma camera calibration factors for quantitation of therapeutic radioisotopes”. In: *EJNMMI physics* 5.1 (2018), p. 8.

- [135] H. von Zimmermann, A. Gosewisch, J. Brosch, L. Kaiser, C. Zach, F. J. Gildehaus, P. Bartenstein, and G. Böning. “Einfluss von Läsionsgröße und Tumor-zu Hintergrundverhältnis auf die quantitative Lutetium-177 SPECT Bildgebung für die Dosimetrie”. In: *Nuklearmedizin* 58.02 (2019).

List of Figures

1.1	Response to Lu-177-DKFZ-PSMA-617 therapy shown for an exemplary mCRPC patient as evaluated via Ga-68-PSMA-11 PET/CT	2
1.2	Sequential whole-body planar imaging of a mCRPC patient at selected time points post injection of 3.7 GBq Lu-177-DKFZ-PSMA-617	2
2.1	Quantitative Lu-177 SPECT/CT imaging and quantified whole-body planar scintigraphy for a mCRPC patient 24 h post injection	5
2.2	Dual-headed Siemens Symbia Intevo T16 SPECT/CT Gamma camera system.	6
2.3	Schematic representation of projection generation via Gamma camera measurement . . .	7
2.4	Schematic view of a Gamma camera detector.	7
2.5	SIMIND simulation study of a Lu-177 point source measured at different distances to the detector head	8
2.6	Relevance of attenuation correction for an exemplary mCRPC patient	10
2.7	Exemplary abdominal SPECT of a mCRPC patient reconstructed without and with Gaussian-based resolution compensation	11
2.8	NEMA body phantom containing six spheres of varying volume (0.5-26.5 ml), filled with a Lu-177 sphere-to-background ratio of 16-to-1 and 8-to-1	12
2.9	Sequential anterior whole-body planar scintigraphy of a mCRPC patient showing an increasing superposition of kidney and intestine activity	14
2.10	Kidney dosimetry based on sequential quantitative SPECT imaging for an exemplary NET patient	16
2.11	Simulated energy distribution around a Lu-177 source voxel	17
3.1	Overview of measurement schemes for lesion and kidney internal dosimetry	22
3.2	Multi-cycle dosimetry for Lu-177-PRRT	24
3.3	Multi-cycle dosimetry for Lu-177-PSMA therapy	24
3.4	Classical and hybrid dosimetry scheme for absorbed dose assessment in tumors, non-marrow OAR, and the bone marrow	26
3.5	Analysis of the ratio of fast-to-slow blood clearance for Lu-177-PSMA-617 therapy	27
3.6	Whole-body planar scintigraphy of two mCRPC patients 24 h post Lu-177-PSMA therapy. .	29
3.7	Correlation of bone marrow and kidney absorbed doses with the patient-specific bone lesion volume	30
3.8	Source-specific contributions to the total bone marrow absorbed dose as evaluated for 10 mCRPC patients.	30
3.9	Simulation study to demonstrate the relevance of patient motion during voxel-wise absorbed dose calculation	31
3.10	Template-based dosimetry workflow for patient-specific 3D bone marrow dosimetry. . . .	32

3.11	Comparison of Ga-68-PSMA-11 PET lesion accumulation with image-based active bone marrow localization via Tc-99m-anti-granulocyte SPECT/CT	32
4.1	Comparison of PSMA PET/CT imaging and active bone marrow localization via Tc-99m-anti-granulocyte SPECT/CT	36
4.2	Simulation study to investigate the feasibility of fast whole-body Lu-177 SPECT imaging	38

List of Tables

2.1	Recovery for the NEMA body phantom of Figure 2.8.	12
3.1	Imaging parameters used for Lu-177 SPECT and Lu-177 whole-body planar acquisitions.	22
3.2	Percent deviations of absorbed dose estimates based on single-SPECT imaging	25
3.3	Effect of patient motion (Figure 3.9) on absorbed dose calculation for three selected lesions	31
3.4	Comparison of different bone marrow absorbed models regarding macroscopic active bone marrow localization	33
4.1	Dosimetry results for the simulation study presented in Figure 4.2.	38

5 | Original publication 1

ORIGINAL RESEARCH

Open Access



Patient-specific image-based bone marrow dosimetry in Lu-177-[DOTA⁰,Tyr³]-Octreotate and Lu-177-DKFZ-PSMA-617 therapy: investigation of a new hybrid image approach

Astrid Gosewisch, Andreas Delker, Sebastian Tattenberg, Harun Ilhan, Andrei Todica, Julia Brosch, Lena Vomacka, Anika Brunegraf, Franz Josef Gildehaus, Sibylle Ziegler, Peter Bartenstein and Guido Böning*

Abstract

Background: The bone marrow (BM) is a main organ at risk in Lu-177-PSMA-617 therapy of prostate cancer and Lu-177-Octreotate therapy of neuroendocrine tumours. BM dosimetry is challenging and time-consuming, as different sequential quantitative measurements must be combined. The BM absorbed dose from the remainder of the body (ROB) can be determined from sequential whole-body planar (WB-P) imaging, while quantitative Lu-177-SPECT allows for more robust tumour and organ absorbed doses. The aim was to investigate a time-efficient and patient-friendly hybrid protocol (HP) for the ROB absorbed dose to the BM. It combines three abdominal quantitative SPECT (QSPECT) scans with a single WB-P acquisition and was compared with a reference protocol (RP) using sequential WB-P in combination with sequential QSPECT images. We investigated five patients receiving 7.4 GBq Lu-177-Octreotate and five patients treated with 3.7 GBq Lu-177-PSMA-617. Each patient had WB-P and abdominal SPECT acquisitions 24 (+ CT), 48, and 72 h post-injection. Blood samples were drawn 30 min, 80 min, 24 h, 48 h, and 72 h post-injection. BM absorbed doses from the ROB were estimated from sequential WB-P images (RP), via a mono-exponential fit and mass-scaled organ-level *S* values. For the HP, a mono-exponential fit on the QSPECT data was scaled with the activity of one WB-P image acquired either 24, 48, or 72 h post-injection (HP24, HP48, HP72). Total BM absorbed doses were determined as a sum of ROB, blood, major organ, and tumour contributions.

Results: Compared with the RP and for Lu-177-Octreotate therapy, median differences of the total BM absorbed doses were 13% (9–17%), 8% (4–15%), and 1% (0–5%) for the HP24, HP48, and HP72, respectively. For Lu-177-PSMA-617 therapy, total BM absorbed doses deviated 10% (2–20%), 3% (0–6%), and 2% (0–6%).

Conclusion: For both Lu-177-Octreotate and Lu-177-PSMA-617 therapy, BM dosimetry via sequential QSPECT imaging and a single WB-P acquisition is feasible, if this WB-P image is acquired at a late time point (48 or 72 h post-injection). The reliability of the HP can be well accepted considering the uncertainties of quantitative Lu-177 imaging and BM dosimetry using standardised organ-level *S* values.

Keywords: Radionuclide therapy, Bone marrow, Dosimetry, Hybrid imaging, Lutetium-177, Prostate cancer, PSMA, mCRPC, Neuroendocrine tumour, Octreotate, NET

* Correspondence: guido.boening@med.uni-muenchen.de
Department of Nuclear Medicine, University Hospital, LMU Munich,
Marchioninistrasse 15, 81377 Munich, Germany

Background

Over the recent years, radionuclide therapy using Lu-177-Octreotate and Lu-177-PSMA-617 evolved as a promising approach for the treatment of metastasised and inoperable neuroendocrine tumours (NET) and metastasised, castration-resistant prostate cancer (mCRPC), respectively [1–3]. The red or active bone marrow (BM) represents a main organ at risk in radionuclide therapy [4–8]. Bone marrow toxicity is particularly of concern in Lu-177-PSMA-617 therapy, as patients suffering from mCRPC often present with a high burden of bone metastases. The latter may cause pronounced activity accumulations in close proximity to the regions which potentially bear active marrow. At these locations, especially the γ -component of the Lu-177 decay might lead to a significant photon cross-irradiation of the bone marrow [9]. However, for Lu-177-Octreotate therapy, the bone marrow is also considered as an organ at risk, as patients with progressive cancer disease usually already underwent several pre-therapies such as external radiotherapy or chemotherapy [3, 4]. These pre-therapies may have interfered with the haematological function of the bone marrow. Thus, bone marrow dosimetry is highly recommended in these patients for risk reduction of marrow toxicities and, at the same time, an as high as possible tumour absorbed dose [10].

The total bone marrow absorbed dose is composed of different contributions originating from various activity source regions: (1) the bone marrow self-absorbed dose including the active bone marrow cells, the extracellular fluid, and the blood cells; (2) activity accumulations in the remaining skeleton composed of compact bone or fatty tissue (yellow or inactive marrow); (3) the cross-absorbed dose by major organs or tumours; and (4) the cross-irradiation coming from the remainder of the body (ROB; whole body minus specific or unspecific accumulations in the other source regions) [11]. Each absorbed dose component requires a dedicated measurement procedure to derive its respective time-activity curve (TAC) and the source-specific time-integrated activity. The cumulated activity-to-absorbed-dose conversion is usually performed via pre-calculated and standardised organ-level S values [11].

The appropriate data collection to accurately quantify the various possible source regions is challenging and leads to both a high clinical workload and long patient examination times, if bone marrow dosimetry shall be routinely performed in the clinic. For Lu-177-Octreotate or Lu-177-PSMA-617 therapy, the bone marrow absorbed dose from the major accumulating organs ($D_{\text{BM} \leftarrow \text{organs}}$), the ROB ($D_{\text{BM} \leftarrow \text{ROB}}$), and the blood ($D_{\text{BM} \leftarrow \text{blood}}$) can be determined from sequential quantitative SPECT images, sequential quantitative whole-body planar images, and multiple blood samples, respectively, in combination with the corresponding S values [8, 9, 11–13]. However, despite the

high metastatic load which might be observed for NET and mCRPC patients, it is challenging to explicitly consider the bone marrow absorbed dose from activity accumulations in the tumours ($D_{\text{BM} \leftarrow \text{tumours}}$) via standardised and pre-calculated tumour-to-bone marrow S values, as the latter intrinsically cannot consider the large inter-patient variability of the shape, size, and distribution of all lesions [14].

Our institutional protocol determines the absorbed dose contribution from the ROB via sequential whole-body planar images [11], which are acquired at three time points at 24, 48, and 72 h post-injection. In addition, we decided to derive organ (e.g. kidneys) and tumour absorbed doses from sequential quantitative SPECT measurements for improved organ and tumour dosimetry [15–18]. However, full whole-body quantitative Lu-177 SPECT is still not commonly used in the clinic, implicating the need of consecutive planar and SPECT imaging at each time point to obtain both reliable bone marrow absorbed doses from the ROB and reliable organ or tumour absorbed doses [19]. Particularly, the increased examination time in case of consecutive SPECT and whole-body planar imaging leads to an increased clinical workload and patient discomfort, as patients with progressive cancer disease may suffer from a bad health condition. Thus, the aim of this work was to derive a time-efficient, patient-friendly, and simplified bone marrow dosimetry protocol for clinical routine. Therefore, we investigated the possibility to reduce the number of image acquisitions from three whole-body planar and three quantitative SPECT scans (reference protocol (RP)) to a single whole-body planar acquisition while maintaining the institution's usual sequential quantitative SPECT protocol (hybrid protocol (HP)). Further, we investigated the effect of this image reduction on the bone marrow absorbed dose from the ROB and on the total bone marrow dose ($D_{\text{BM} \leftarrow \text{total}}$), to prove whether the proposed hybrid protocol provides comparable absorbed dose estimates for both Lu-177-Octreotate and Lu-177-PSMA-617 therapy. For the determination of the total bone marrow absorbed dose, the energy depositions in the bone marrow due to activity accumulations in the ROB, blood, major organs, and tumours were considered. Furthermore, we determined the best-suited time point for this single whole-body planar image acquisition with respect to the time points available in our institutional protocol. All absorbed dose calculations are based on the organ-level S values (e.g. whole ROB to bone marrow) [11].

Methods

Patient selection, data acquisition, and image quantification

Patient selection

This study is based on ten patients, with five patients suffering from somatostatin receptor-positive neuroendocrine

metastases (P1-P5) and five patients from mCRPC with expression of PSMA-avid lesions (P6-P10). Details for each patient are provided in Tables 1 and 2. All patients received multiple therapy cycles of approximately 3.7 GBq Lu-177-DKFZ-PSMA-617 (Lu-177-PSMA-617) or 7.4 GBq Lu-177-[DOTA⁰,Tyr³]-Octreotate (Lu-177-Octreotate). All patients except one mCRPC patient showed soft tissue lesions on the pre-therapeutic Ga-68-HBED-CC-PSMA or Ga-68-[DOTA⁰,Tyr³]-Octreotate PET/CT scans, while all prostate-specific membrane antigen (PSMA) patients and two NET patients additionally presented with bone metastases (Tables 1 and 2). The local ethics committee approved the study protocol and did not desire any written consent for the study entry. The study is based on retrospective and anonymised patient data.

Data acquisition

Data for dosimetry were acquired during a routine 4-day in-patient stay following the radiopharmaceutical injection, in conjunction with standard clinical examinations. All patients received a 15-min one-bed abdominal SPECT scan and a 20-min whole-body planar scintigraphy at 24, 48, and 72 h post-injection (p. i.) on a dual-headed Symbia T2 SPECT/CT (Siemens Medical Solutions, Erlangen, Germany). Counts were detected for the photopeak window of 208 keV (width 15%) by the usage of a medium-energy low-penetration collimator. Two additional scatter windows were measured at 170 keV (width 15%) and 240 keV (width 10%). A low-dose AC-CT was acquired at the first image acquisition session for

anatomical correlation and attenuation correction during quantitative SPECT reconstruction. For the determination of the absorbed dose to the bone marrow from the activity circulating in the blood, five venous blood samples were drawn from the site contralateral to injection at 30 and 80 min p. i. and 24, 48, and 72 h p. i. [9, 20].

SPECT image reconstruction and quantification

Quantitative SPECT images were reconstructed as described by Delker et al. [9] via a rotation-based, penalised, one-step-late ordered subset expectation maximisation algorithm, which included corrections for scatter, attenuation, and distance-dependent geometrical collimator blur. Attenuation correction was performed for each SPECT scan via the AC-CT, which was acquired along with the SPECT scan 24 h post-injection. To apply the attenuation correction, especially to the SPECT scans 48 and 72 h p. i., the single AC-CT was co-registered onto an initial SPECT reconstruction without attenuation correction by using a rigid body co-registration algorithm with six degrees of freedom (PMOD Version 3.609, PMOD Technologies, Zurich, Switzerland). If only one AC-CT is acquired for sequential SPECT imaging, special care has to be taken to minimise misregistration between SPECT images and separately acquired CT scans, as such a misalignment can distort the proper attenuation correction and, thus, activity quantification. This is in principal also true for serial SPECT and CT imaging, as even within a single image acquisition session patient movements cannot be entirely avoided. Scatter correction employed the triple energy window (TEW) method.

Table 1 Characteristics of all NET patients included in this study for Lu-177-Octreotate therapy

Octreotate	P1	P2	P3	P4	P5
Sex	M	M	F	F	F
Age	68	66	61	47	73
Activity investigated cycle [MBq]	7654	7425	7420	7409	7410
Diagnosis	NET small intestine	NET	NET terminal ileum	NET pancreas	NET stomach
Metastases (PET/CT)					
- Extend	Medium	Medium	Medium	Medium	Medium
- Type (VIS = visceral, LYM = lymph, OSS = osseous)	Mainly VIS (liver), LYM	Mainly LYM, VIS (liver)	Mainly VIS (liver), LYM, OSS	Mainly LYM, VIS (liver and other)	Mainly VIS (liver), OSS
Proliferation index	Ki67 3–4%	Ki67 5–10%	Ki67 1%	Ki67 10%	Ki67 10%
Pre-therapies	SSA-analogues	Interferon alpha	Hemicolectomy, SSA-analogues, radioembolization	Chemotherapy (stoptozotocin/5-FU, dacarbazapin, capecitabin/Te-modal)	SSA-analogues, bisphosphonate therapy
Blood pre-therapy					
- Leukocytes [G/l]	7.76	10.4	3.79	3.93	10.2
- Erythrocytes [T/l]	4.58	4.50	4.43	3.73	4.42
- Thrombocytes [G/l]	207	294	297	177	303
- Haematocrit	0.421	0.442	0.373	0.341	0.399

Table 2 Characteristics of all mCRPC patients included in this study for Lu-177-PSMA-617 therapy

PSMA-617	P6	P7	P8	P9	P10
Age	68	66	61	47	73
Activity investigated cycle [MBq]	3718	3743	3745	3752	3700
Diagnosis	mCRPC	mCRPC	mCRPC	mCRPC	mCRPC
Metastases (PET/CT)					
- Extend	High	High	High	High	High
- Type (VIS = visceral, LYM = lymph, OSS = osseous)	Mainly VIS (liver), OSS, LYM	Only OSS	Mainly OSS, LYM	Mainly OSS, LYM	Mainly OSS, LYM
Initial TNM classification	pT3b, pN1, R0, G3, Gleason 9	pT4, N1, R1, G3, Gleason 8	pT3b, pN1, R1, Gleason 9	pT3a, pN1, pR1, Gleason 9	pT4, N1, R1, Gleason 9
PSA [ng/ml]	368	1201	5436	408	101
Pre-therapies (1, yes/0, no)					
- Surgery	0	1	1	1	1
- Radiotherapy	1	1	1	0	0
- Anti-hormonal therapy (including bicalutamide, enzalutamide, abiraterone acetate)	1	1	1	1	1
- Radionuclide therapy (Ra-223)	0	1	0	1	1
- Chemotherapy (docetaxel, cabazitaxel)	1	1	1	1	0
Blood pre-therapy					
- Leukocytes [G/l]	4.90	7.20	5.60	6.20	5.00
- Erythrocytes [T/l]	4.31	4.79	4.08	4.35	4.00
- Thrombocytes [G/l]	307	195	291	314	191
- Haematocrit	0.376	0.406	0.335	0.377	0.366

Correction for distance-dependent collimator blur made use of a Gaussian blur model. Corrections for partial volume effects and dead time were not applied. For conversion of the measured counts per second and per voxel to Becquerel per millilitre, an appropriate calibration factor was determined. Therefore, we used a large cylinder of approximately 20 cm diameter, which was filled with a known activity concentration and which has been imaged and reconstructed via the same protocol [9, 15, 20].

Planar image correction and calibration

For each patient, all acquired whole-body planar images were corrected for scatter and attenuation on a pixel basis via a dedicated MATLAB routine (Fig. 1) [16, 20, 21]; for the correction of scatter, the TEW method was applied, as for the quantitative SPECT images. For the attenuation correction, a linear projection of μ values along the ventral axis of the patient was created from the diagnostic CT image of the pre-therapeutic Ga-68 PET/CT scan, which covered nearly the whole patient body from the middle of the head to approximately the knees. Therefore, a conversion between the Hounsfield units (HUs) in the diagnostic CT and the μ values at 208 keV was established by acquiring a CT scan of a Gammex tissue phantom (Gammex 467; Gammex, Inc., Middleton, WI) with 16 tissue rods of known composition and thus known attenuation characteristics [22]. The μ values of all rods were plotted against the measured HUs, and a bilinear fit model (range 1: $HU = (-688; 0)$; range 2: $HU = (0; 1127)$) was applied to the whole data set [15, 22]. This calibration curve allows for the assignment of μ values to a continuous range of HUs. The lower arms and legs as well as a part of the

head were not included in the PET/CT data, as the arms are usually positioned above the head during the PET/CT scan and as the PET/CT scan is usually not acquired over the entire patient length. By contrast, the arms, legs, and head are fully included in the whole-body planar images, and an appropriate μ value has to be defined for each segment (Fig. 1). Thus, mean μ values derived from three patients with PET/CT acquisitions of the head, legs, and arms were assigned to the missing segments. Therefore, all segments—the part visible on the PET/CT and the missing parts of the head, arms, and legs—were delineated on the co-registered whole-body planar images (delineation and rigid body co-registration via PMOD Version 3.609). The resulting map of the regions of interest (ROI) was saved, with each ROI segment being characterised via a defined value. This ROI map was then loaded by a self-designed MATLAB routine, which assigned the defined μ value to each segment according to the ROI number. Afterwards, the resulting whole-body integral μ -map was blurred via a Gaussian filter with a width approximating an average resolution of the gamma camera (geometric resolution of full width at half maximum of 11 mm at 10 cm). Pixel-wise attenuation correction was finally performed in conjunction with geometric averaging of both planar views (conjugate view method) [21].

Calibration of whole-body planar images was performed via the corresponding quantitative abdominal SPECT by using the fact that ideally the total activity A_{SPECT} within the quantitative SPECT should be correlated to the number of counts per second (cps) x_{planar} in the planar abdominal counterpart multiplied by an appropriate calibration factor:

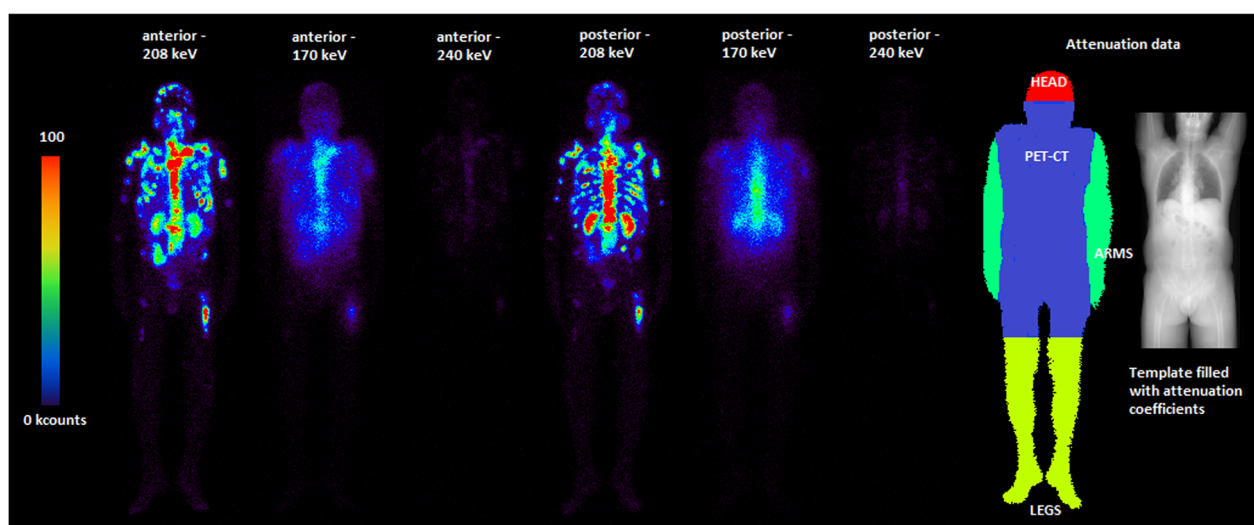


Fig. 1 Workflow for planar image quantification shown for patient P8. Anterior and posterior views for all three energy windows (24 h p. i.; photopeak and both scatter windows) and attenuation map based on the projected patient-specific CT from the PET/CT scan

$$A_{\text{SPECT}} = x_{\text{planar}} \cdot C_{\text{planar,SPECT}}. \quad (1)$$

$C_{\text{planar,SPECT}}$ denotes the SPECT-based calibration factor in units of Bq/cps.

Bone marrow dosimetry formalism

To derive total bone marrow absorbed doses ($D_{\text{BM} \leftarrow \text{total}}$), a sum of the bone marrow self-absorbed dose from the activity in the blood ($D_{\text{BM} \leftarrow \text{blood}}$) as well as the bone marrow cross-absorbed dose by major organs ($D_{\text{BM} \leftarrow \text{organs}}$), tumours ($D_{\text{BM} \leftarrow \text{tumours}}$), and the ROB ($D_{\text{BM} \leftarrow \text{ROB}}$) was considered according to the findings of previous studies [5, 7–9, 13]. If not indicated otherwise, the general term bone marrow always refers to the red or active bone marrow, i.e. the radiation-sensitive part of the bone marrow mixture [23]. The dose contribution of each source component to the bone marrow was estimated according to the guidelines of the European Association of Nuclear Medicine (EANM) [11]. Following the Medical Internal Radiation Dose (MIRD) formalism underlying the EANM guidelines, the absorbed dose to the bone marrow originating from a specified source region ($D_{\text{BM} \leftarrow \text{source}}$) was calculated according to Eq. (2) [24]:

$$\begin{aligned} D_{\text{BM} \leftarrow \text{source}} &= S_{\text{BM} \leftarrow \text{source}} \cdot \tilde{A}_{\text{source}} \\ &= S_{\text{BM} \leftarrow \text{source}} \cdot \int_0^{\infty} A_{\text{source}}(t) dt. \end{aligned} \quad (2)$$

$\tilde{A}_{\text{source}}$ describes the time-integrated activity per source region and $S_{\text{BM} \leftarrow \text{source}}$ the corresponding S value or absorbed dose conversion factor. $A_{\text{source}}(t)$ corresponds to the source-specific time-activity curve (TAC), which is based on sequential measurements and a subsequent fit to the source time-activity measurements. For this study, S values are taken from the public tabulations of Monte Carlo simulation results for the standardised male (Lu-177-PSMA-617 and Lu-177-Octreotate therapy) or female (Lu-177-Octreotate therapy) anthropomorphic phantom as provided, amongst other phantoms, by RADAR [25]. To adjust these phantom-based S values to the patient-specific conditions, all S values were scaled according to a non-linear mass scaling approach developed by Traino et al. [26].

Absorbed dose from the blood time-integrated activity

In the absence of specific binding to the bone marrow or blood cells, as indicated for PSMA therapy [27, 28], the bone marrow self-absorbed dose is solely given by the activity in the extracellular fluid of the marrow tissue [11]. The activity in the extracellular fluid of the bone marrow can be derived from the activity concentration in the blood plasma (blood method), multiplied with the

red marrow extracellular fluid fraction (RMECF = 0.19) of the bone marrow [11, 29, 30]. The activity concentration in the plasma can in turn be determined from the activity concentration in the blood ($[\tilde{A}_{\text{blood}}]$) and the patient-specific haematocrit (HCT), if there is no specific binding to the blood cells [11]. This yields to:

$$D_{\text{BM} \leftarrow \text{blood}}^{\text{PSMA}} = [\tilde{A}_{\text{blood}}] \cdot \text{RMBLR} \cdot m_{\text{BM,patient}} \cdot S_{\text{BM} \leftarrow \text{BM,phantom}} \cdot \left(\frac{m_{\text{BM,phantom}}}{m_{\text{BM,patient}}} \right)^a, \quad (3.1)$$

$$\text{RMBLR}^{\text{PSMA}} = \frac{\text{RMECF}}{1 - \text{HCT}}. \quad (3.2)$$

where RMBLR corresponds to the red-marrow-to-blood activity concentration ratio [11]. m denotes the bone marrow (BM) or whole-body (WB) masses ($m_{\text{BM/WB,phantom/patient}}$) of either the phantom or of the patient [11, 26].

For Lu-177-Octreotate therapy, it holds that:

$$D_{\text{BM} \leftarrow \text{blood}}^{\text{OCTREO}} = [\tilde{A}_{\text{blood}}] \cdot \text{RMBLR} \cdot m_{\text{BM,patient}} \cdot S_{\text{BM} \leftarrow \text{BM,phantom}} \cdot \left(\frac{m_{\text{BM,phantom}}}{m_{\text{BM,patient}}} \right)^a. \quad (3.3)$$

$$\text{RMBLR}^{\text{OCTREO}} = 1 \quad (3.4)$$

[11, 13]. To scale the male and female S values to the patient anatomy, an exponent of $a = 1.001$ and $a = 0.992$ was proposed for Lu-177-PSMA-617 and Lu-177-Octreotate therapy, respectively [26]. To derive the patient-specific blood TAC, 1 ml of blood of each sample was pipetted into a test tube and measured within a Cobra Gamma Counter (Packard Instrument Company, Inc., Meriden, CT), which has been previously calibrated via five 1-ml test samples of known activity concentration. For the calculation of the time-integrated blood activity concentration, a bi-exponential model was fitted to the time-activity data, followed by integration from zero to infinity according to Eq. (2).

Absorbed dose from the remainder of body and major organs

Via subtraction of the time-integrated activity in the extracellular fluid and the time-integrated activity of the main accumulating organs from the whole-body, the respective ROB time-integrated activity (\tilde{A}_{ROB}) was determined. The whole-body and organ time-integrated activities, \tilde{A}_{WB} and \tilde{A}_{organ} , were determined from a mono-exponential fit to the three measurement points at 24, 48, and 72 h post-injection.

All organ activities were derived from the sequential SPECT images, while for the determination of the whole-body activity, the sequential whole-body planar images were used. The kidneys were considered as main accumulating organs for both Lu-177-Octreotate and Lu-177-PSMA-617 therapy, according to the previous studies assessing dosimetric estimates [5, 7–9]. The patient-specific volumes of interest (VOIs) for the kidneys were defined based on a percent isocontour of the organ maximum and of the quantitative SPECT at 24 h p. i. (PMOD Version 3.609), since images taken at early time points offer a high signal-to-background ratio for organ delineation. We adjusted the isocontour level for each patient in the best way with the usage of the CT as guidance. For all patients, an isocontour level of 30–40% was found to be appropriate. All kidney VOIs were copied to the following SPECT scans 48 and 72 h p. i., which were co-registered onto the SPECT scan 24 h p. i. in advance. We manually re-positioned, i.e. shifted or rotated, the kidney VOIs in case of imperfect co-registration of the individual SPECT time points. For Lu-177-Octreotate therapy, the liver and spleen were additionally included in the bone marrow absorbed dose from the organs [5]. For the patient-wise delineation of the liver and spleen, a similar approach as for the kidney definition was chosen using a 10 to 15% isocontour for the liver and a 30 to 40% isocontour for the spleen. The lower isocontour for liver delineation can be explained by the fact that NET patients often exhibit liver metastases, which lead to a heterogeneous activity accumulation with multiple hot spots.

The bone marrow absorbed dose from the ROB is finally given by the following formula according to Hindorf et al. with adjusted exponents as proposed by Traino et al. [11, 26]:

$$\tilde{A}_{\text{ROB}} = \tilde{A}_{\text{WB}} - [\tilde{A}_{\text{blood}}] \cdot \text{RMBLR} \cdot m_{\text{BM},\text{patient}} - \sum_{\text{all organs}} \tilde{A}_{\text{organ}}, \quad (4.1)$$

$$D_{\text{BM} \leftarrow \text{ROB}} = \tilde{A}_{\text{ROB}} \cdot \left(S_{\text{BM} \leftarrow \text{WB},\text{phantom}} \cdot \left(\frac{m_{\text{WB},\text{phantom}}}{m_{\text{WB},\text{patient}}} \right)^b \cdot \left(\frac{m_{\text{BM},\text{phantom}}}{m_{\text{BM},\text{patient}}} \right)^c - S_{\text{BM} \leftarrow \text{BM},\text{phantom}} \cdot \left(\frac{m_{\text{BM},\text{phantom}}}{m_{\text{ROB},\text{patient}}} \cdot \frac{m_{\text{BM},\text{phantom}}}{m_{\text{BM},\text{patient}}} \right)^a - \sum_{\text{all organs}} S_{\text{BM} \leftarrow \text{organ},\text{phantom}} \cdot \frac{m_{\text{organ},\text{phantom}}}{m_{\text{ROB},\text{patient}}} \cdot \frac{m_{\text{BM},\text{phantom}}}{m_{\text{BM},\text{patient}}} \right). \quad (4.2)$$

Eq. (4.2) considered all phantom- and patient-specific whole-body, ROB, bone marrow, and organ masses

$m_{\text{WB}/\text{ROB}/\text{BM}/\text{organ},\text{phantom}/\text{patient}}$ for S value scaling. For male and female patients, $b = 0.896$ and $b = 0.894$ as well as $c = 0.963$ and $c = 0.970$ were used, as proposed by Traino et al. [26]. The bone marrow absorbed dose contribution of each individual organ is given by:

$$D_{\text{BM} \leftarrow \text{organ}} = \tilde{A}_{\text{organ}} \cdot S_{\text{BM} \leftarrow \text{organ},\text{phantom}} \cdot \frac{m_{\text{organ},\text{phantom}}}{m_{\text{organ},\text{patient}}} \cdot \frac{m_{\text{BM},\text{phantom}}}{m_{\text{BM},\text{patient}}}. \quad (5)$$

Due to the high tumour load, as it is frequently observed in Lu-177-PSMA-617 therapy and sometimes in Lu-177-Octreotate therapy, we included all tumour activities in the ROB activity and the ROB S value was applied. As all patients investigated for Lu-177-Octreotate therapy suffered from liver metastases, the tumour activities had to be removed from the healthy liver activity for each time point. Therefore, tumour VOIs were delineated on the SPECT 24 h p. i. based on a 40% isocontour and transferred to the following SPECT scans, as it was the case for the determination of the organ activities.

Hybrid imaging for determination of the ROB cross-absorbed dose to the bone marrow

Reference dosimetry protocol

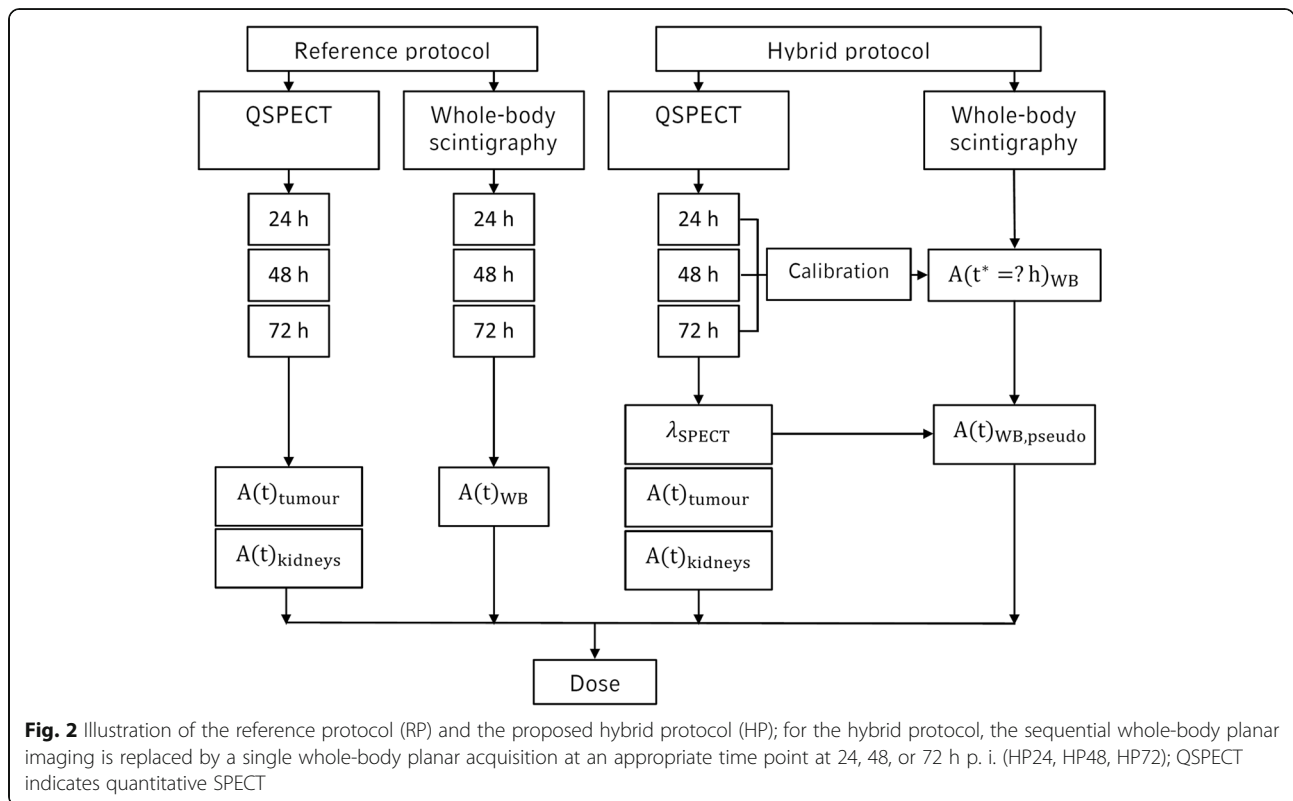
For the reference protocol (RP), the bone marrow absorbed dose from the ROB is determined from all three available whole-body planar scans (Fig. 2). For the total bone marrow absorbed dose, the absorbed dose from the three constituents, organs, blood, and ROB, was summed. For each dose constituent, the percentage contribution ($\text{PC}_{\text{constituent}}$) to the total bone marrow absorbed dose was calculated:

$$\text{PC}_{\text{constituent}} = \frac{D_{\text{BM} \leftarrow \text{constituent}}}{D_{\text{BM} \leftarrow \text{total}}} \cdot 100\%. \quad (6)$$

Hybrid dosimetry protocol

The proposed hybrid protocol (HP) uses a single whole-body image and sequential single-bed quantitative SPECT acquisitions of the abdomen to determine the ROB TAC, instead of deriving the ROB TAC from sequential whole-body planar imaging.

First, the abdominal effective decay constant λ_{SPECT} was derived via a mono-exponential fit to the total activity in the SPECT scans 24, 48, and 72 h post-therapy. Especially, all organs and all tumours were included in the fitting of the TAC, as it was the case for the determination of \tilde{A}_{WB} from the reference protocol. This effective decay constant λ_{SPECT} serves as a surrogate for the reference-protocol-based whole-body effective decay



constant (Fig. 2). The mono-exponential SPECT-based abdominal TAC was then scaled with a chosen base point. This base point is defined via the whole-body activity $A_{WB}(t^*)$ of a single whole-body planar image acquired at an arbitrary time point $t^* \in 24, 48, \text{ or } 72 \text{ h}$ post-therapy. The resulting pseudo-whole-body TAC $A_{WB, \text{pseudo}}(t)$ is intended to serve as an estimate of the reference-protocol-based whole-body TAC (Eq. (7.1)) and can be further used to determine a pseudo-whole-body time-integrated activity $\tilde{A}_{WB, \text{pseudo}}$ (Eq. (7.2)).

$$A_{WB, \text{pseudo}}(t) = A_{WB, \text{pseudo}}(t^*) \cdot \exp(-\lambda_{\text{SPECT}} \cdot (t - t^*)), \quad (7.1)$$

$$\begin{aligned} \tilde{A}_{WB, \text{pseudo}} &= \int_{t=0}^{\infty} A_{WB, \text{pseudo}}(t') dt' \\ &= \frac{A_{WB}(t^*) \cdot \exp(\lambda_{\text{SPECT}} \cdot t^*)}{\lambda_{\text{SPECT}}} \\ &= \frac{A_{WB}(t^*) \cdot \exp(\lambda_{\text{SPECT}} \cdot t^*) \cdot T_{1/2, \text{SPECT}}}{\ln(2)}. \end{aligned} \quad (7.2)$$

$T_{1/2, \text{SPECT}}$ denotes the SPECT-based effective half-life.

Comparison of reference and hybrid absorbed dose values

Based on the hybrid model given in Eqs. (7.1) and (7.2), the bone marrow absorbed dose from the ROB

can be estimated by Eqs. (4.1) and (4.2). In this work, we investigated a combination of the sequential abdominal SPECT with the whole-body planar images at 24, 48, or 72 h p. i., where each whole-body planar image was individually calibrated via the quantitative SPECT at the corresponding time point (Fig. 2). These different hybrid protocols were further denoted as HP24, HP48, and HP72. The agreement of the bone marrow absorbed doses from the ROB, as determined via the HP and the RP, was assessed. Therefore, the percentage deviation between absorbed dose estimates (PD_{dose} ; Eq. (8)) was calculated, and a statistical test for correlation was performed (MATLAB Pearson correlation analysis).

$$PD_{\text{dose}} = \left| \left(\frac{D_{\text{HP24/HP48/HP72}} - D_{\text{RP}}}{D_{\text{RP}}} \right) \right| \cdot 100\%. \quad (8)$$

Furthermore, the same analysis was performed regarding the total bone marrow absorbed dose estimates composed of all available constituents: the ROB (including tumours), the explicitly analysed organs, and the contribution of the blood activity. While the application of the hybrid protocol affects the bone marrow absorbed dose from the ROB, all other constituents were not altered.

Comparison of hybrid and reference ROB TAC parameters

For a mono-exponential TAC, the time-integrated activity is calculated as the product of the effective half-life $T_{1/2}$ and the y -axis intercept A_0 of the fit function:

$$\tilde{A} = \frac{A_0}{\ln(2)} \cdot T_{1/2}. \quad (9)$$

The proposed hybrid protocol assumes that ideally, the SPECT-based abdominal effective half-life is equal to the whole-body effective half-life. However, in reality, differences in both half-lives will lead to deviations in the area under the whole-body TACs derived from the reference protocol and hybrid protocol, and thus in the respective whole-body and ROB time-integrated activities. Simultaneously, these deviations in the course of the TACs may affect the y -axis intercepts of the reference-protocol-based and hybrid-protocol-based TACs. To address this issue, both fit function parameters, effective half-life and the y -axis intercept, were compared for the reference protocol, HP24, HP48, and HP72. For a perfect agreement between the reference-protocol-based and hybrid-protocol-based ROB time-integrated activities, \tilde{A}_{RP} and \tilde{A}_{HP} , the product of the ratio of reference-to-hybrid effective half-lives ($\frac{T_{1/2,RP}}{T_{1/2,HP}}$) and the ratio of reference-to-hybrid y -axis intercepts ($\frac{A_{0,RP}}{A_{0,HP}}$) has to yield 1:

$$\frac{\tilde{A}_{RP}}{\tilde{A}_{HP}} = \frac{A_{0,RP}}{A_{0,HP}} \cdot \frac{T_{1/2,RP}}{T_{1/2,HP}} = 1 \quad (10)$$

Results

Reference dosimetry protocol

Based on the reference protocol, median total bone marrow absorbed doses were calculated as 12.1 mGy/GBq (range 9.6–15.6 mGy/GBq) for Lu-177-Octreotate and 10.8 mGy/GBq (range 6.7–16.8 mGy/GBq) for Lu-177-PSMA-617 therapy (Table 3). The blood absorbed dose contribution was higher for Lu-177-Octreotate compared with Lu-177-PSMA-617 therapy, with a larger inter-patient variability for Lu-177-PSMA-617 therapy. The median values were found to be 59% (range 50–63%) for Lu-177-Octreotate therapy and 43% (range 13–63%) for Lu-177-PSMA-617, respectively (Table 3). The median ROB contribution was 34% (range 29–41%) for Lu-177-Octreotate and 45% (range 34–80%) for Lu-177-PSMA-617 therapy, again with a higher variance of the patient-specific percentage contributions for Lu-177-PSMA-617 therapy (Table 3). For Lu-177-PSMA-617 therapy, the higher percentage ROB contribution to the total bone marrow absorbed dose is on the one hand driven by the larger tumour load for the investigated mCRPC patients, as all tumours were included in the ROB compartment. On

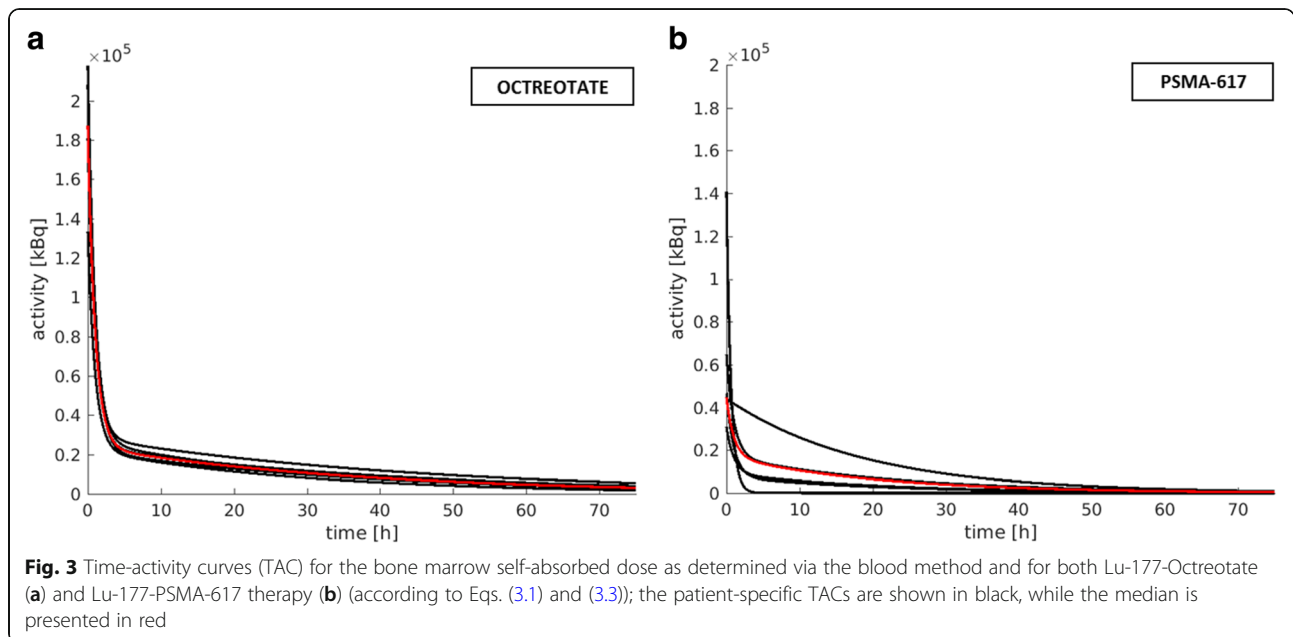
Table 3 Results from the reference protocol. Total bone marrow absorbed doses ($D_{BM \leftarrow total}$) and the percentage contribution of ROB, blood, and organs to the total bone marrow absorbed dose. All percentage contributions were calculated according to Eq. (6)

Patient	$D_{BM \leftarrow total}$ [mGy/GBq]	ROB [%]	Blood [%]	Organs [%]
Octreotate				
P1	12.1	29	63	8
P2	9.6	34	60	6
P3	15.6	34	59	7
P4	11.8	36	59	5
P5	12.7	41	50	9
Median	12.1	34	59	8
PSMA-617				
P6	10.2	36	56	8
P7	6.7	45	43	12
P8	16.8	80	13	7
P9	14.2	34	63	3
P10	8.3	60	28	12
Median	10.8	45	43	8

the other hand, the percentage contribution of the bone marrow absorbed dose from the blood is reduced for Lu-177-PSMA-617 therapy compared with Lu-177-Octreotate therapy due to the weighting of the blood activity with the patient haematocrit and the RMECFE, yielding an average weighting factor of 0.3. Furthermore, for the five mCRPC patients in this study, a lower median effective half-life for the slow phase of the bi-exponential fit to the blood time-activity measurements was observed, compared with the five NET patients (Lu-177-Octreotate, 25 h; Lu-177-PSMA-617, 14 h; Fig. 3). The major accumulating organs contributed at maximum 9% (median: all organs 8%, kidneys 4%, liver 2%, spleen 1%) for Lu-177-Octreotate therapy and 12% (median kidneys 8%) for Lu-177-PSMA-617 therapy (Table 3).

Hybrid protocol and comparison of reference and hybrid absorbed dose values

For Lu-177-Octreotate therapy, the median deviations of the bone marrow absorbed dose from the ROB were found to be 37% (range 29–42%), 23% (range 11–38%), and 3% (range 1–13%) for the HP24, HP48, and HP72, respectively, compared with the results obtained via the reference protocol (Fig. 4a). A very strong and significant ($p < 0.05$) correlation between the reference and hybrid protocol was confirmed for all base points 24, 48, 72 h p. i. with Pearson correlation coefficients of 0.98, 0.93, and 0.98. However, a tendency of overestimation of the bone marrow absorbed dose from the ROB, especially for the HP24 and the HP48, is noticed (Fig. 5a–c). The



respective deviations for Lu-177-PSMA-617 were found to be 29% (range 3–46%), 4% (range 1–17%), and 4% (range 1–18%) (Fig. 4c) with a very strong Pearson correlation of 0.98, 1.00, and 1.00, respectively (Fig. 5d–f). The tendency of overestimation of the bone marrow absorbed dose from the ROB was also evident for the HP24, but reduced for the HP48 and HP72 (Fig. 5d–f).

The deviations between the reference and hybrid protocol were lower for the total bone marrow absorbed dose estimates compared with those for the ROB alone (Fig. 4). For Lu-177-Octreotate therapy, median differences of the total bone marrow absorbed doses were 13% (range 9–17%), 8% (range 4–15%), and 1% (range 0–5%) using the HP24, HP48, and HP72, respectively, with a very strong and significant ($p < 0.05$) Pearson correlation of 0.98, 0.96, and 0.99 (Figs. 4b and 5a–c). As it was the case for the bone marrow absorbed dose from the ROB alone, especially the use of an early base point leads to overestimated absorbed dose values (Table 4 and Fig. 5a–c). For Lu-177-PSMA-617 therapy, the median deviations were found to be 10% (range 2–20%), 3% (range 0–6%), and 2% (range 0–6%) with a very strong correlation of 0.99, 1.00, and 1.00, respectively (Figs. 4d and 5d–f). The tendency of overestimated absorbed dose values was particularly evident for the base point 24 h p. i. (Table 4 and Fig. 5d–f).

To summarise, for Lu-177-Octreotate, the best agreement with respect to the reference protocol was obtained with the hybrid protocol based on 72 h p. i. for all patient cases, while for Lu-177-PSMA-617 therapy for 40% of the patients, the time point of 48 h p. i. and for 40% the acquisition of 72 h p. i. was best suited. For one mCRPC patient, both base points, 48 and 72 h p. i.,

provided the same absolute deviation from the reference (Table 4).

Comparison of hybrid and reference TAC parameters

For both Lu-177-Octreotate and Lu-177-PSMA-617 therapy, the whole-body effective half-life was shorter compared with the washout in the abdominal region, except for patient P9, who presented with pronounced and strongly accumulating bone metastasis in the right hip (Table 5). Median whole-body and abdominal effective half-lives were found to be 43 h (range 40–62 h) and 61 h (range 53–87 h) for Lu-177-Octreotate therapy and 31 h (range 22–65 h) and 42 h (range 31–67 h) for Lu-177-PSMA-617 therapy. Table 5 indicates a tendency to lower whole-body and abdominal effective half-lives for Lu-177-PSMA-617 compared with Lu-177-Octreotate therapy, except for patient P8, who showed the highest bone tumour load with strong and persistent retention of the radiopharmaceutical (Fig. 1). The deviation between the effective half-lives was similar for both therapies with 40% (range 30–42%) for Lu-177-Octreotate therapy and 46% (range 4–64%) for Lu-177-PSMA-617 therapy, however, with a larger observed variability for Lu-177-PSMA-617 therapy (Table 5).

Figure 6 shows examples of fitted reference-protocol-based whole-body and hybrid-protocol-based whole-body TACs for both Lu-177-Octreotate (patient P4) and Lu-177-PSMA-617 (patient P8) therapy. The use of the SPECT-based effective half-life for the hybrid protocol leads to an under- and overestimation of the reference-protocol-based TAC before and after the selected base point. This under- and overestimation is varying for the HP24, HP48, and HP72 and also affects

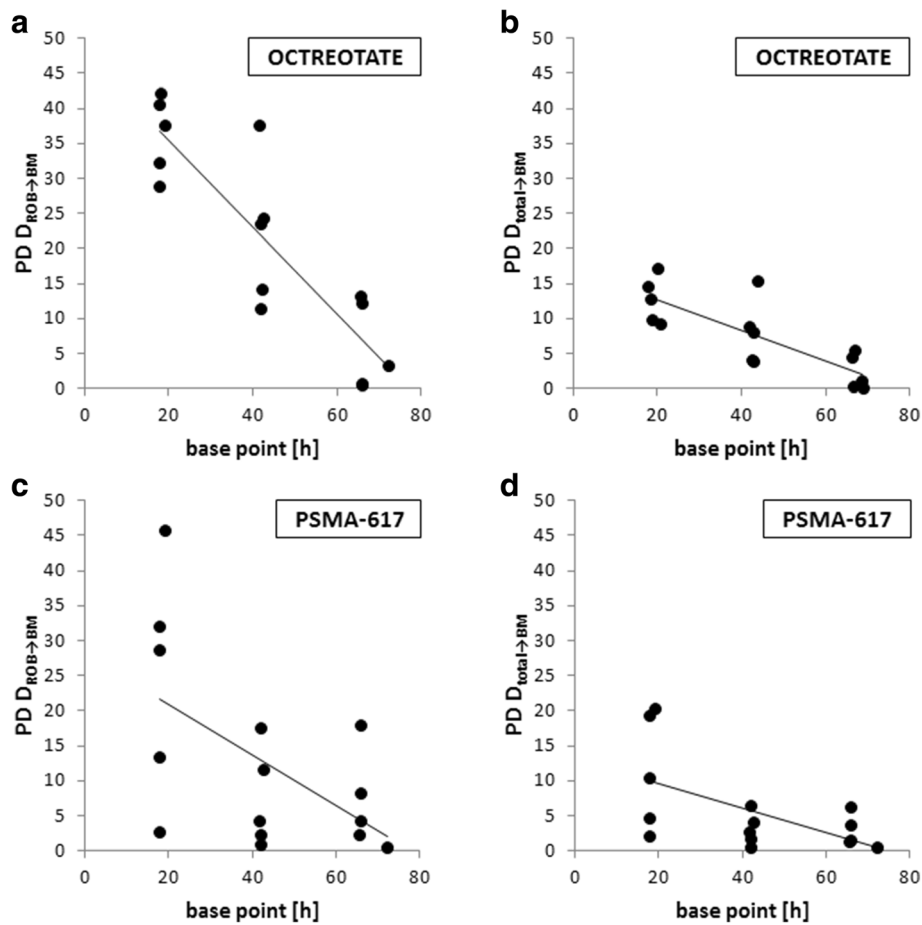


Fig. 4 Percentage deviation (PD) from the reference protocol for the bone marrow absorbed dose from the ROB and the total bone marrow absorbed dose depending on the base point used for the hybrid protocol (24, 48, or 72 h p. i.). All percentage deviations were calculated according to Eq. (8)

the y -axis intercept of the hybrid-protocol-based TACs in comparison to the reference protocol. Figure 7 summarises the patient-specific ratios of the reference-to-hybrid effective half-lives in comparison to the ratio of the corresponding y -axis intercepts. The black line indicates all combinations of effective half-life and y -axis intercept ratios, for which the reference-protocol-based and hybrid-protocol-based time-integrated activities are equal. For Lu-177-Octreotate therapy, the median ratio of the reference-to-hybrid effective half-lives was found to be 0.7 (range 0.7–0.8). Simultaneously, the reference-to-hybrid y -axis intercept ratios increase for the base points from 24 to 72 h post-therapy. For the HP72, the combination of effective half-life and y -axis intercept ratios yields to the closest agreement between the reference-protocol-based and hybrid-protocol-based time-integrated activities (Fig. 7a). For Lu-177-PSMA-617 therapy, the median ratio of the reference-to-hybrid effective half-lives was calculated as 0.7 (range 0.6–1.3). The larger variability in the reference-to-hybrid

effective half-life ratios is also evident in Fig. 7b. For Lu-177-PSMA-617 therapy, for the time points 48 and 72 h p. i., combinations of reference-to-hybrid effective half-life ratios and y -axis intercept ratios were found which result close to a ratio of 1 between the reference-protocol-based and hybrid-protocol-based ROB time-integrated activities.

Discussion

Although all bone marrow absorbed dose estimates are well below the typically applied critical threshold of 2 Gy [5] and no severe marrow toxicities have been observed for all investigated patients, bone marrow dosimetry is still a matter of interest. This is particularly true regarding the maximum absorbed dose that can be applied for patients with progressive cancer disease, who already underwent several pre-therapies. The absorbed dose estimates determined in this study are in good agreement with the findings of previous studies for both therapies [5, 7, 8, 31].

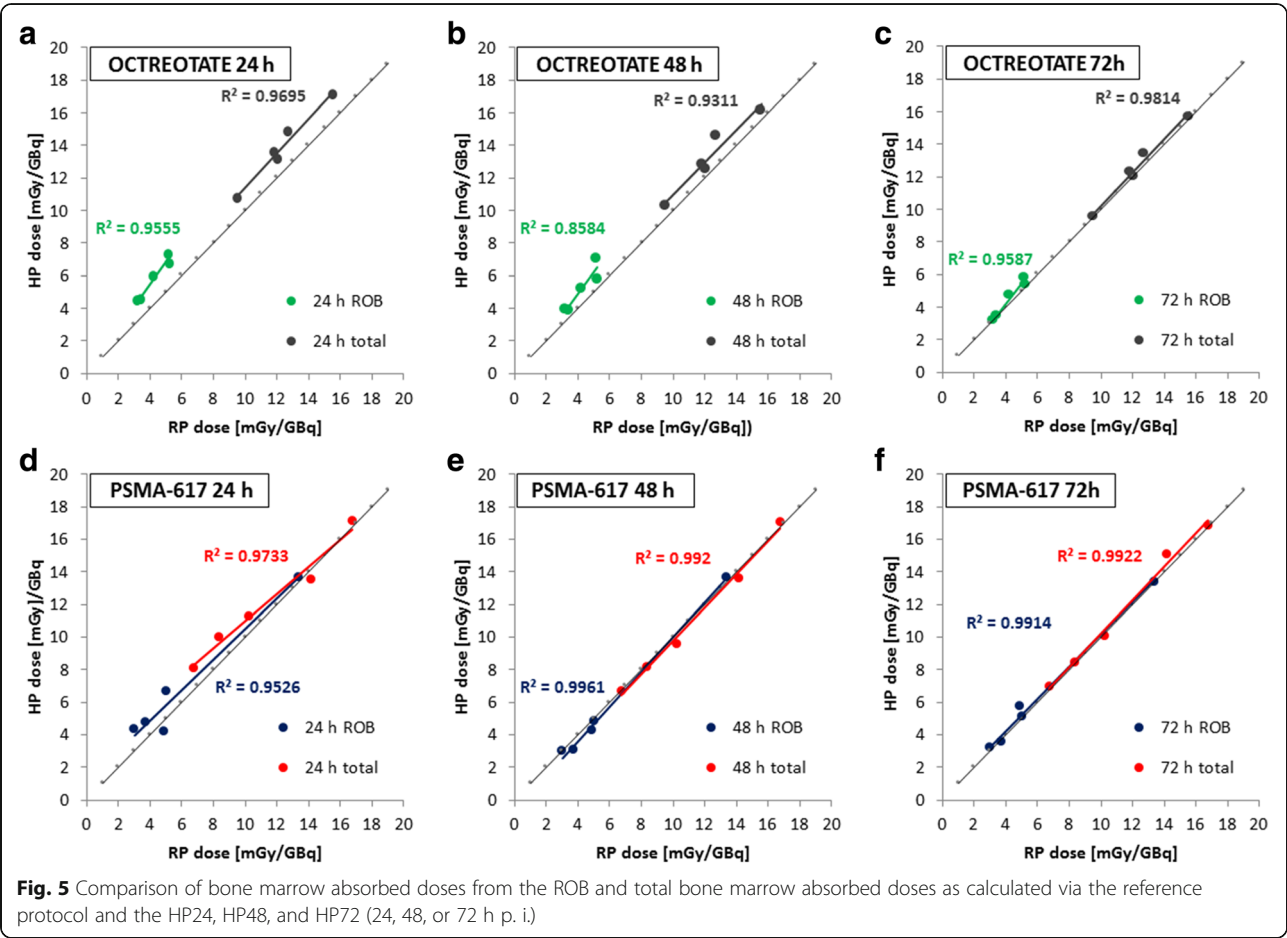


Table 4 Comparison of the reference and hybrid protocol for different time points of single whole-body planar image acquisition (24 h p. i.: HP24; 48 h p. i.: HP48; 72 h p. i.: HP72); all calculated total bone marrow absorbed doses ($D_{BM \leftarrow total}$) are provided

Patient	$D_{BM \leftarrow total}$ RP [mGy/GBq]	$D_{BM \leftarrow total}$ HP24 [mGy/GBq]	$D_{BM \leftarrow total}$ HP48 [mGy/GBq]	$D_{BM \leftarrow total}$ HP72 [mGy/GBq]
Octreotate				
P1	12.1	13.2	12.6	12.1
P2	9.6	10.8	10.3	9.6
P3	15.6	17.1	16.2	15.7
P4	11.8	13.5	12.8	12.3
P5	12.7	14.9	14.7	13.4
Median	12.1	13.5	12.8	12.3
PSMA-617				
P6	10.2	11.3	9.6	10.1
P7	6.7	8.1	6.7	7.0
P8	16.8	17.1	17.1	16.8
P9	14.2	13.5	13.6	15.1
P10	8.3	10.0	8.1	8.5
Median	10.2	11.3	9.6	10.1

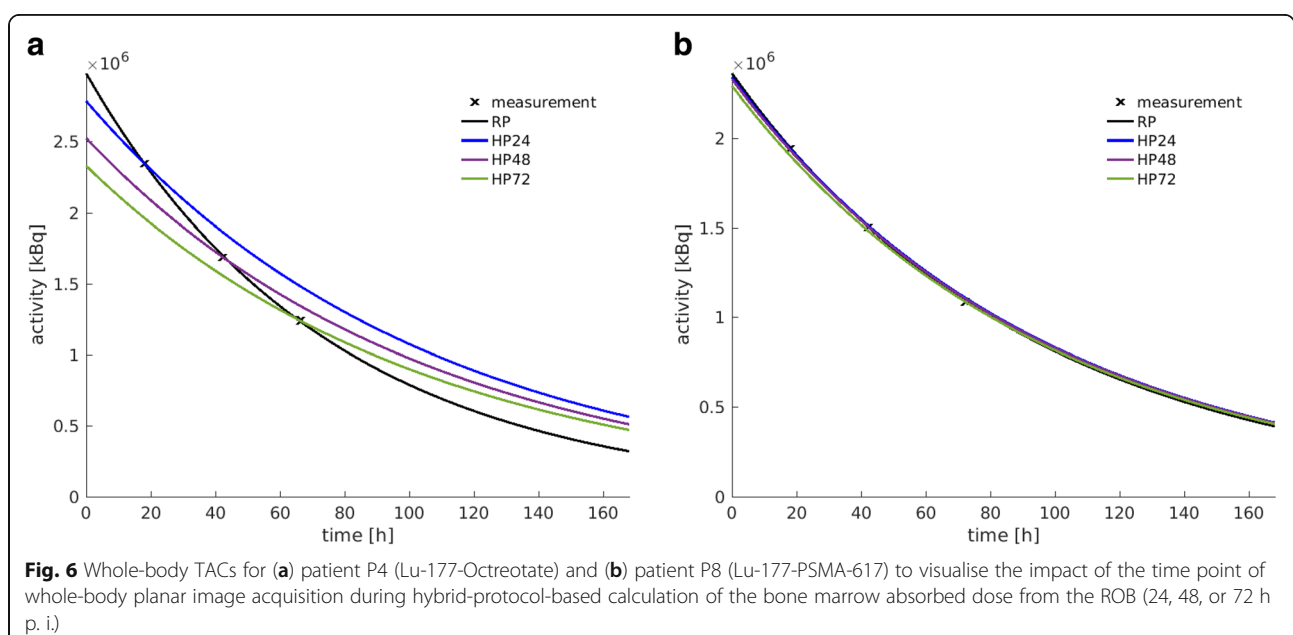
Table 5 Comparison of planar-based whole-body ($T_{1/2, WB}$) and SPECT-based abdominal effective half-lives ($T_{1/2, SPECT}$) for Lu-177-PSMA-617 and Lu-177-Octreotate therapy

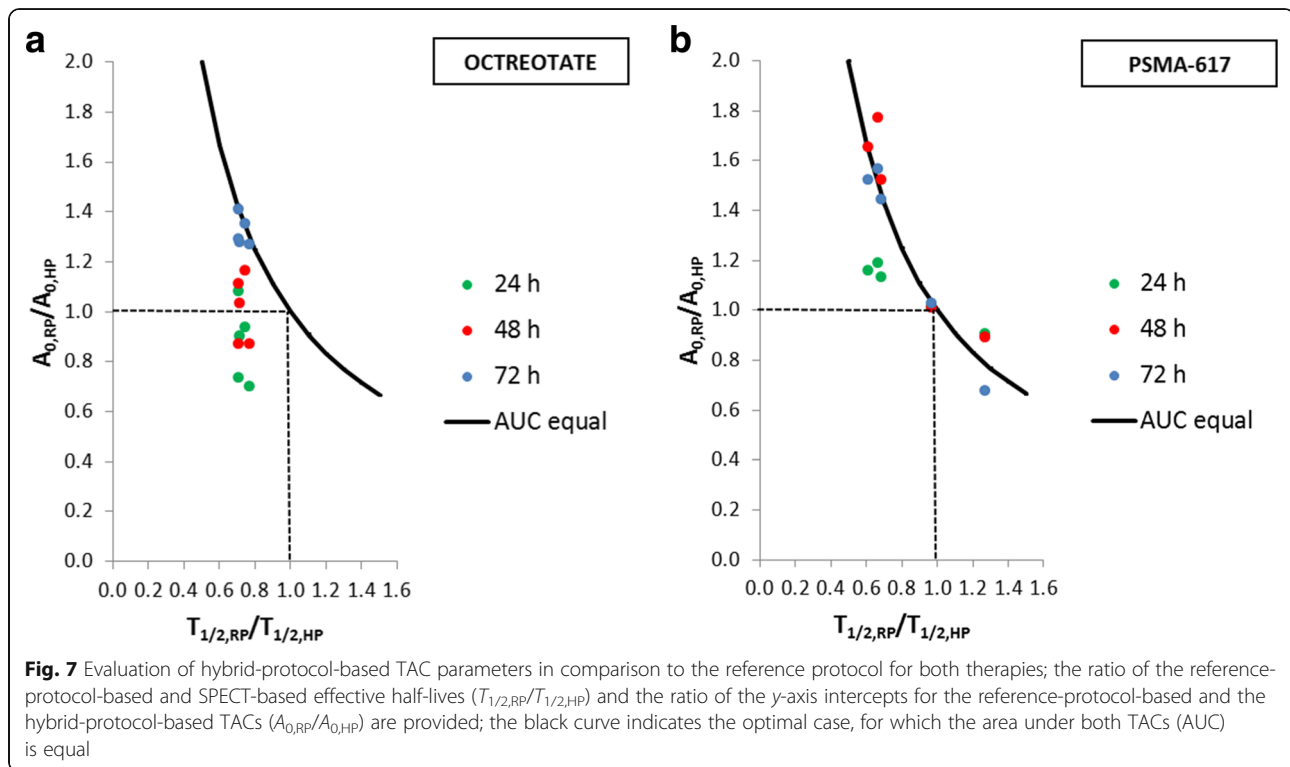
Patient	$T_{1/2, WB}$ [h]	$T_{1/2, SPECT}$ [h]
Octreotate		
P1	40	53
P2	43	61
P3	43	56
P4	52	73
P5	62	87
Median	43	61
PSMA-617		
P6	22	33
P7	31	50
P8	65	67
P9	39	31
P10	29	42
Median	31	42

According to the current clinical standard, an uncertainty of at least 10–20% has to be expected for the derived activity and absorbed dose values in case of quantitative Lu-177 SPECT imaging, and even greater values might be expected for planar imaging [15–17, 32, 33]. Thus, the results presented in this study suggest that the application of a hybrid SPECT planar dosimetry approach based on late whole-body planar images allows for bone marrow dosimetry which is sufficiently reliable and applicable in clinical routine. In the case of Lu-177-Octreotate therapy of patients bearing NET and

with regard to our institutional measurement protocol, the best time point for whole-body planar imaging was found to be approximately at 72 h p. i., with maximum deviations of the total bone marrow absorbed dose of 5% compared to the reference protocol. In patients with mCRPC receiving Lu-177-PSMA-617 therapy, the whole-body planar imaging time points 48 and 72 h p. i. provided comparable total bone marrow absorbed dose estimates with similar maximum differences of 6% to the reference-protocol-based full sequential whole-body planar approach. If five to ten Lu-177-PSMA-617 or Lu-177-Octreotate therapies are offered per week, the reduction of whole-body planar scans from three to one results in a reduction of examination time of 3.5 to 7 h per week. Simultaneously, the application of the proposed hybrid imaging protocol does not lead to an increased workload for the absorbed dose calculations.

The magnitude of deviations depends on the differences in the abdominal and whole-body washout and the positioning of the base point used for scaling of the mono-exponential pseudo-whole-body TAC. Analysis of the patient-specific reference-protocol-based and hybrid-protocol-based TAC parameters revealed that the use of a prolonged SPECT-based effective half-life is compensated by a lower y -axis intercept, if a later base point is selected. The use of a base point later than 72 h p. i. still has to be investigated; however, such a time point was unfortunately not available in our institutional measurement protocol. As expected, the deviations between the reference and hybrid protocol were larger for the bone marrow absorbed dose from the ROB compared with the total bone marrow absorbed dose, as the median ROB contribution to the total absorbed dose





was found to be only 34% for Lu-177-Octreotate therapy and 45% for Lu-177-PSMA-617 therapy.

The appropriate whole-body planar imaging time point may have to be determined separately for each type of therapy. The degree of the deviations between abdominal and whole-body effective decay constants is driven by the disease- or therapy-specific retention in the organs and tumours and the corresponding typical tumour distribution. The mCRPC patients included in this study typically showed a larger tumour load compared with the NET patients, which was additionally strongly varying over the whole patient body. For most of the mCRPC patients (except P9) included in this study, the main metastatic load was located in the torso, and consequently, the abdominal effective half-life was larger compared with the whole-body effective half-life. By contrast, patient P9 suffered from a strongly accumulating metastasis in the hip, leading to a comparatively larger whole-body effective half-life. The larger variability in the whole-body tumour distribution for mCRPC patients causes the observed larger spread in the differences between abdominal and whole-body effective half-lives. Consequently, a high tumour load outside the SPECT field of view might lead to an increased uncertainty of the proposed hybrid protocol, and this effect should be further investigated. As it was the case for most of the mCRPC patients, the investigated NET cases mainly presented with metastases in the torso, which lead to an increased retention of the radiopharmaceutical in

the abdomen. However, due to the lower tumour load, the inter-patient variability in the abdominal and whole-body effective half-lives was reduced for the NET patients under study.

The change from one-bed abdominal SPECT imaging to the imaging of two or more beds could principally improve the proposed hybrid protocol for bone marrow dosimetry, as an enlarged acquisition area will lead to a more realistic estimate of the whole-body effective half-life. Furthermore, the introduction of fast multi-bed SPECT imaging in the clinical routine would be beneficial for a robust tumour and organ dosimetry over a larger part of the patient body [15–18]. Attempts to introduce fast whole-body SPECT imaging into the clinic already exist [34]. However, the effect of a reduction of scan time on absorbed dose estimates for Lu-177 therapy still has to be evaluated.

The accuracy of dosimetry based on standardised organ-level S values is limited, as such S values are inherently not capable to fully consider the patient-specific full 3D functional and anatomical characteristics. The latter fact remains true, even if a scaling of the S values to the specific anatomical conditions is applied [6, 14, 35–37]. For Lu-177, the ROB cross-absorbed dose of the bone marrow is mainly driven by the long-range photon component, which is more sensitive to the anatomy than the locally deposited beta absorbed dose. In a previous study based on Monte Carlo simulations, deviations of the order of up to 100% were observed, if photon

cross-absorbed doses were calculated based on standardised S values [38]. Furthermore, S values are determined based on the assumption of homogeneous activity accumulation. However, the activity accumulation in the ROB with the inclusion of tumours is highly heterogeneous with the degree of heterogeneity being caused by both tumour load and distribution. With regard to both aspects the limited consideration of the patient-specific functional and anatomical characteristics, the reliability of the proposed hybrid protocol can be well accepted in the framework of organ-level S values. Moreover, it should also be noted that the exact bone marrow distribution of each patient is a priori unknown due to the heterogeneous micro-structure of the bone marrow and its pathologically highly variable distribution, which both lead to a highly unspecified target for bone marrow dosimetry [23]. Particularly, for mCRPC patients with a high bone tumour load, a displacement of active bone marrow from highly metastasised to tumour-free skeletal sites is possible [39].

Our decision to include all tumours in the ROB represents a simplified approach for clinical routine bone marrow dosimetry. On the one hand, this approach is more practical, as in case of a high bone tumour load, a manual determination of the time-integrated activity is not feasible for each tumour lesion in an acceptable time. On the other hand, even if a semi-automatic or automatic tumour segmentation is available, tumour-to-bone marrow S values for both individual tumours and the total tumour distribution are not available, as tumours are quite variable in shape, size, and position, and the pre-calculation of all possible S values is not possible. Thus, at this point, a more simplified approach was chosen, which considered all tumours at once within the ROB compartment. The approximation to use the S value of the compartment in which the tumours are located to estimate the bone marrow absorbed dose from lesions has also been applied in previous studies [5]. An alternative way, proposed by Svensson et al. for bone marrow dosimetry for Lu-177-Octreotate therapy, differentiates the activity distribution in the patient body in low- and high-activity regions (background vs. main accumulating organs and tumours) with separate S values applied to each of both compartments [31]. The resulting bone marrow absorbed doses correlated with the change of blood parameters and were found to be in a similar range compared to previously published results. Monte Carlo studies may help in further understanding the effect of such simplifying assumptions for bone marrow dosimetry.

Conclusions

For both Lu-177-PSMA-617 and Lu-177-Octreotate therapy, bone marrow dosimetry can be performed via a single whole-body planar image and a sequential SPECT (hybrid protocol), provided that this planar image is

acquired at a later time point. Regarding the three imaging time points 24, 48, and 72 h, which were available for this study, the time points of 48 or 72 h p. i. were found to be suitable for Lu-177-PSMA-617 therapy. For Lu-177-Octreotate therapy, a time point of 72 h p. i. was identified as appropriate. This hybrid protocol enables total bone marrow absorbed dose estimates with a maximum deviation of 5–6% compared to a dosimetry protocol using both sequential planar and SPECT imaging. These deviations can be considered acceptable with regard to the uncertainties which currently have to be expected for Lu-177 quantitative imaging and bone marrow dosimetry based on organ-level S values. However, the proposed hybrid protocol allows for a more patient-friendly and time-efficient bone marrow dosimetry in clinical routine due to the decreased examination times.

Availability of data and materials

Please contact the author for data requests.

Authors' contributions

AG, AD, ST, JB, LV, HI, AT, SZ, PB, and GB contributed to the concept and design of the study. AB supervised the collection of all clinical data for dosimetry and the related quality control. FJG was responsible for radiopharmaceutical production. AG, AD, ST, HI, AT, and GB carried out all data analysis. All authors contributed to the drafting of the manuscript, and all authors read and approved the manuscript.

Ethics approval and consent to participate

This study is based on retrospective and anonymised data, which was acquired for routine clinical dosimetry (Ethics Committee of LMU Munich).

Consent for publication

Not applicable.

Competing interests

The authors declare that they have no competing interests.

Publisher's Note

Springer Nature remains neutral with regard to jurisdictional claims in published maps and institutional affiliations.

Received: 13 April 2018 Accepted: 16 July 2018

Published online: 03 August 2018

References

1. Strosberg J, et al. Phase 3 trial of 177Lu-Dotatate for midgut neuroendocrine tumors. *N Engl J Med*. 2017;376(2):125–35.
2. Afshar-Oromieh A, et al. The theranostic PSMA ligand PSMA-617 in the diagnosis of prostate cancer by PET/CT: biodistribution in humans, radiation dosimetry, and first evaluation of tumor lesions. *J Nucl Med*. 2015;56(11):1697–705.
3. Emmett L, et al. Lutetium 177 PSMA radionuclide therapy for men with prostate cancer: a review of the current literature and discussion of practical aspects of therapy. *J Med Radiat Sci*. 2017;64(1):52–60.
4. Zaknun JJ, et al. The joint IAEA, EANM, and SNMMI practical guidance on peptide receptor radionuclide therapy (PRRT) in neuroendocrine tumours. *Eur J Nucl Med Mol Imaging*. 2013;40(5):800–16.
5. Sandström M, et al. Individualized dosimetry of kidney and bone marrow in patients undergoing 177Lu-DOTA-octreotate treatment. *J Nucl Med*. 2013; 54(1):33–41.
6. Cremonesi M, et al. Dosimetry in peptide radionuclide receptor therapy: a review. *J Nucl Med*. 2006;47(9):1467–75.

7. Baum RP, et al. Lutetium-177 PSMA radioligand therapy of metastatic castration-resistant prostate cancer: safety and efficacy. *J Nucl Med*. 2016; <https://doi.org/10.2967/jnumed.115.168443>.
8. Kabasakal L, et al. Lu-177-PSMA-617 prostate-specific membrane antigen inhibitor therapy in patients with castration-resistant prostate cancer: stability, bio-distribution and dosimetry. *Mol Imaging Radionucl Ther*. 2017; 26(2):62.
9. Delker A, et al. Dosimetry for 177Lu-DKFZ-PSMA-617: a new radiopharmaceutical for the treatment of metastatic prostate cancer. *Eur J Nucl Med Mol Imaging*. 2016;43(1):42–51.
10. Strigari L, et al. The evidence base for the use of internal dosimetry in the clinical practice of molecular radiotherapy. *Eur J Nucl Med Mol Imaging*. 2014;41(10):1976–88.
11. Hindorf C, et al. EANM dosimetry committee guidelines for bone marrow and whole-body dosimetry. *Eur J Nucl Med Mol Imaging*. 2010;37(6):1238–50.
12. Delker A, et al. The influence of early measurements onto the estimated kidney dose in [177Lu][DOTA0, Tyr3] octreotate peptide receptor radiotherapy of neuroendocrine tumors. *Mol Imaging Biol*. 2015;17(5):726–34.
13. Forrer F, et al. Bone marrow dosimetry in peptide receptor radionuclide therapy with [177Lu-DOTA0, Tyr3] octreotate. *Eur J Nucl Med Mol Imaging*. 2009;36(7):1138.
14. Stabin MG. Uncertainties in internal dose calculations for radiopharmaceuticals. *J Nucl Med*. 2008;49(5):853–60.
15. Dewaraja YK, et al. MIRD pamphlet no. 23: quantitative SPECT for patient-specific 3-dimensional dosimetry in internal radionuclide therapy. *J Nucl Med*. 2012;53(8):1310–25.
16. Garkavij M, et al. 177Lu-[DOTA0, Tyr3] octreotate therapy in patients with disseminated neuroendocrine tumors: analysis of dosimetry with impact on future therapeutic strategy. *Cancer*. 2010;116(5):1084–92.
17. He B, et al. Evaluation of quantitative imaging methods for organ activity and residence time estimation using a population of phantoms having realistic variations in anatomy and uptake. *Med Phys*. 2009;36(2):612–9.
18. Ljungberg M, Sjögren-Gleisner K. The accuracy of absorbed dose estimates in tumours determined by quantitative SPECT: a Monte Carlo study. *Acta Oncol*. 2011;50(6):981–9.
19. Beyer T, et al. The future of hybrid imaging—part 1: hybrid imaging technologies and SPECT/CT. *Insights Imaging*. 2011;2(2):161–9.
20. Ljungberg M, et al. MIRD pamphlet no. 26: joint EANM/MIRD guidelines for quantitative 177Lu SPECT applied for dosimetry of radiopharmaceutical therapy. *J Nucl Med*. 2016;57(1):151–62.
21. Siegel JA, et al. MIRD pamphlet no. 16: techniques for quantitative radiopharmaceutical biodistribution data acquisition and analysis for use in human radiation dose estimates. *J Nucl Med*. 1999;40(2):375.
22. Martinez L, Calzado A. Evaluation of a bilinear model for attenuation correction using CT numbers generated from a parametric method. *Appl Radiat Isot*. 2016;107:77–86.
23. Hough M, et al. An image-based skeletal dosimetry model for the ICRP reference adult male—internal electron sources. *Phys Med Biol*. 2011; 56(8):2309.
24. Bolch WE, et al. MIRD pamphlet no. 21: a generalized schema for radiopharmaceutical dosimetry—standardization of nomenclature. *J Nucl Med*. 2009;50(3):477–84.
25. Stabin MG, et al. RADAR reference adult, pediatric, and pregnant female phantom series for internal and external dosimetry. *J Nucl Med*. 2012; 53(11):1807–13.
26. Traino A, et al. Influence of total-body mass on the scaling of S-factors for patient-specific, blood-based red-marrow dosimetry. *Phys Med Biol*. 2007; 52(17):5231.
27. Trover JK, Beckett ML, Wright GL. Detection and characterization of the prostate-specific membrane antigen (PSMA) in tissue extracts and body fluids. *Int J Cancer*. 1995;62(5):552–8.
28. Silver DA, et al. Prostate-specific membrane antigen expression in normal and malignant human tissues. *Clin Cancer Res*. 1997;3(1):81–5.
29. Sgouros G. Bone marrow dosimetry for radioimmunotherapy: theoretical considerations. *J Nucl Med*. 1993;34(4):689–94.
30. Hermann K, et al. Biodistribution and radiation dosimetry for a probe targeting prostate-specific membrane antigen for imaging and therapy. *J Nucl Med*. 2015;56(6):855–61.
31. Svensson J, et al. A novel planar image-based method for bone marrow dosimetry in 177Lu-DOTATATE treatment correlates with haematological toxicity. *EJNMMI Phys*. 2016;3(1):21.
32. Gustafsson J, et al. Uncertainty propagation for SPECT/CT-based renal dosimetry in 177Lu peptide receptor radionuclide therapy. *Phys Med Biol*. 2015;60(21):8329.
33. Peterson M, Gustafsson J, Ljungberg M. Monte Carlo-based quantitative pinhole SPECT reconstruction using a ray-tracing back-projector. *EJNMMI Phys*. 2017;4(1):32.
34. Bandi P, Zsoter N, Wirth A, Luetzen U, Derlin T, Papp L. New workflows and algorithms of bone scintigraphy based on SPECT-CT. In *Engineering in Medicine and Biology Society (EMBC). Annual International Conference of the IEEE*. 2012;5971–4.
35. Stabin M, Flux G. Internal dosimetry as a tool for radiation protection of the patient in nuclear medicine. *Biomed Imaging Interv J*. 2007;3(2):e28.
36. Stabin MG, Brill AB. State of the art in nuclear medicine dose assessment. *Seminars in nuclear medicine*. 2008;38(5):308–20.
37. Bolch WE, et al. MIRD pamphlet no. 17: the dosimetry of nonuniform activity distributions—radionuclide S values at the voxel level. *J Nucl Med*. 1999;40(1):S11.
38. Grimes J, Celler A. Comparison of internal dose estimates obtained using organ-level, voxel S value, and Monte Carlo techniques. *Med Phys*. 2014; 41(9):092501.
39. Hensel J, Thalmann GN. Biology of bone metastases in prostate cancer. *Urology*. 2016;92:6–13.

Submit your manuscript to a SpringerOpen[®] journal and benefit from:

- Convenient online submission
- Rigorous peer review
- Open access: articles freely available online
- High visibility within the field
- Retaining the copyright to your article

Submit your next manuscript at ► [springeropen.com](https://www.springeropen.com)


6 | Original publication 2

ORIGINAL RESEARCH

Open Access



3D Monte Carlo bone marrow dosimetry for Lu-177-PSMA therapy with guidance of non-invasive 3D localization of active bone marrow via Tc-99m-anti-granulocyte antibody SPECT/CT

Astrid Gosewisch¹, Harun Ilhan¹, Sebastian Tattenberg¹, Andrea Mairani², Katia Parodi³, Julia Brosch¹, Lena Kaiser¹, Franz Josef Gildehaus¹, Andrei Todica¹, Sibylle Ziegler¹, Peter Bartenstein¹ and Guido Böning^{1*} 

Abstract

Background: The bone marrow (BM) is a main risk organ during Lu-177-PSMA ligand therapy of metastasized castration-resistant prostate cancer (mCRPC) patients. So far, BM dosimetry relies on *S* values, which are pre-computed for reference anatomies, simplified activity distributions, and a physiological BM distribution. However, mCRPC patients may show a considerable bone lesion load, which leads to a heterogeneous and patient-specific activity accumulation close to BM-bearing sites. Furthermore, the patient-specific BM distribution might be significantly altered in the presence of bone lesions. The aim was to perform BM absorbed dose calculations through Monte Carlo (MC) simulations and to investigate the potential value of image-based BM localization.

This study is based on 11 Lu-177-PSMA-617 therapy cycles of 10 patients (10 first cycles), who obtained a pre-therapeutic Ga-68-PSMA-11 PET/CT; quantitative Lu-177 SPECT acquisitions of the abdomen 24 (+CT), 48, and 72 h p.i.; and a Lu-177 whole-body planar acquisition at 24 h post-therapy. Patient-specific 3D volumes of interest were segmented from the Ga-68-PSMA-11 PET/CT, filled with activity information from the Lu-177 data, and imported into the FLUKA MC code together with the patient CT. MC simulations of the BM absorbed dose were performed assuming a physiological BM distribution according to the ICRP 110 reference male (MC1) or a displacement of active BM from the direct location of bone lesions (MC2). Results were compared with those from *S* values (SMIRD). BM absorbed doses were correlated with the decrease of lymphocytes, total white blood cells, hemoglobin level, and platelets. For two patients, an additional pre-therapeutic Tc-99m-anti-granulocyte antibody SPECT/CT was performed for BM localization.

Results: Median BM absorbed doses were 130, 37, and 11 mGy/GBq for MC1, MC2, and SMIRD, respectively. Significant strong correlation with the decrease of platelet counts was found, with highest correlation for MC2 (MC1: $r = -0.63$, $p = 0.04$; MC2: $r = -0.71$, $p = 0.01$; SMIRD: $r = -0.62$, $p = 0.04$). For both investigated patients, BM localization via Tc-99m-anti-granulocyte antibody SPECT/CT indicated a displacement of active BM from the direct location of lesions similar to model MC2 and led to a reduction in the BM absorbed dose of 40 and 41% compared to MC1.

(Continued on next page)

* Correspondence: guido.boening@med.uni-muenchen.de

¹Department of Nuclear Medicine, University Hospital, LMU Munich, Marchioninistrasse 15, 81377 Munich, Germany

Full list of author information is available at the end of the article

(Continued from previous page)

Conclusion: Higher BM absorbed doses were observed for MC-based models; however, for MC2, all absorbed doses were still below 2 Gy. MC1 resulted in critical values for some patients, but is suspected to yield strongly exaggerated absorbed doses by neglecting bone marrow displacement. Image-based BM localization might be beneficial, and future studies are recommended to support an improvement for the prediction of hematotoxicities.

Keywords: Radioligand therapy, Dosimetry, Monte Carlo, Bone marrow, mCRPC, Lutetium, PSMA, Tc-99m-anti-granulocyte antibody scintigraphy, Bone marrow localization

Introduction

In radioligand therapy, dosimetry is recommended for appropriate treatment planning and aims for maximizing the absorbed dose to malignant structures, while minimizing the absorbed dose to risk organs. A variety of strategies for the assessment of tissue absorbed doses exist, which can be distinguished depending on how detailed the patient-specific information is considered or depending on whether a 3D-absorbed dose model is used or absorbed dose factors (S values) are applied [1–5]. Monte Carlo techniques can be used to fully simulate all interactions of radioactive decay particles within the surrounding material in a step-by-step manner. Various Monte Carlo codes such as FLUKA or GEANT4 were extended to applications in nuclear medicine and are capable to consider the patient-specific 3D activity and anatomical characteristics via inclusion of the SPECT, PET, and CT data into the simulation [6–12]. Thus, 3D-absorbed dose distributions with resolution and accuracy depending on the input image data can be provided. However, the absorbed dose to risk organs or tumors during radioligand therapy is usually calculated via organ-level S values, which were pre-calculated based on standardized anthropomorphic phantoms and which estimate the mean absorbed dose to the whole target region based on the mean time-integrated activity in a specified source region.

The active bone marrow (BM) is a main organ at risk during Lu-177-PSMA ligand therapy, especially as patients with advanced mCRPC often present with a high bone tumor burden and a potentially reduced hematological function [13–15]. Typically, bone marrow dosimetry is performed by applying the aforementioned S values and accounts for the self-absorbed dose to the bone marrow from the blood, the cross-absorbed dose from the remainder of the body (ROB), and the cross-absorbed dose from major organs and tumors as specific source regions [15–19]. However, during bone marrow dosimetry using organ-level S values, simplifying assumptions have to be made to estimate the absorbed dose from the overall tumor distribution, as no pre-calculated S values exist that consider all lesions in their size, shape, number, and location. Thus, Monte Carlo simulations may lead to

improved bone marrow absorbed dose estimates, as they have the potential to fully account for the patient-specific 3D disease characteristics.

Another limitation of classical bone marrow dosimetry is that the actual localization of the active bone marrow is a priori unknown. Bone lesions might lead to a displacement of active bone marrow from the direct site of metastases and thus activity accumulation, which would drastically reduce the absorbed dose to the active bone marrow [20, 21]. However, bone marrow dosimetry using pre-calculated organ-level S values assumes a physiological bone marrow distribution [16]. Clinical imaging methods, such as magnetic resonance imaging or Tc-99m-anti-granulocyte antibody scintigraphy, can be used for non-invasive active bone marrow localization, within the spatial resolution of the corresponding imaging modality [22–25]. Thus, such techniques might overcome the limitation of an a priori unknown target region for bone marrow dosimetry.

In this study, we performed 3D simulations of the bone marrow absorbed dose for mCRPC patients, assuming either an active bone marrow distribution, which is not altered by the bone tumor load, or a displacement of active bone marrow from the location of bone metastasis. These results were compared to the respective bone marrow absorbed dose estimates derived via organ-level S values. Subsequently, all absorbed dose estimates were further correlated with the patient-specific changes in hematological parameters. For a subgroup of investigated patients, a Tc-99m-anti-granulocyte antibody SPECT/CT was acquired prior to therapy, which was further analyzed to investigate Monte-Carlo-based bone marrow dosimetry with and without knowledge of the patient-specific active bone marrow distribution.

If not indicated otherwise, the term bone marrow always refers to the active bone marrow, which represents the radio-sensitive part of the overall bone marrow mixture.

Material and methods

Patients and data acquisition

This study is based on the first cycle of 10 patients, who showed PSMA avid soft tissue and bone lesions on the

pre-therapeutic whole-body Ga-68-PSMA-11 PET/CT. Patients P1–P4 were treated with on average 3.7 GBq Lu-177-PSMA-617, while for all other patients, the dosing scheme was increased to 6 GBq, according to initial dosimetry results at our institution [15, 26] (Table 1). Patient P7 received a fifth therapy cycle at our institution with prior image-based active bone marrow localization and was included as patient P8 (Table 1), as this rare data allows for an exemplarily comparison of patient-specific bone marrow dosimetry without and with knowledge of the patient-specific bone marrow distribution. All patients received a 15-min abdominal Lu-177 SPECT/CT scan and a 20-min whole-body planar scintigraphy at 24 h p.i., as well as a 15-min abdominal SPECT at 48 h and 72 h p.i. on a dual-headed Symbia T2 SPECT/CT (Siemens Medical Solutions, Erlangen, Germany). The SPECT and planar whole-body acquisitions were based on a standard Lu-177 imaging protocol, using a medium-energy low-penetration collimator, the photopeak at 208 keV (width 15%), and two additional scatter windows at 170 keV (width 15%) and 240 keV (width 10%) [15, 26, 27]. For dosimetry purposes, five venous blood samples were drawn from each

patient 30 and at maximum 80 min post-start of infusion, and before each image acquisition. Blood parameters were further monitored as a part of clinical routine until the next therapy cycle [28]. Monitoring of blood element counts was performed at the morning prior to therapy (baseline), each morning during the following 3 days until discharge, and at 4 and 8 weeks until the next therapy cycle.

For patients P8 and P9, an additional Tc-99m-anti-granulocyte antibody SPECT/CT (Scintimun, GLYCO-TOPE Biotechnology GmbH, Heidelberg, Germany) was acquired prior to radioligand therapy for localization of the active bone marrow. A 25-min two-bed SPECT/CT scan of thorax and abdomen was performed at 3–4 h after the injection of approximately 400 MBq. Image acquisition followed a standard Tc-99m protocol using a low-energy high-resolution collimator, a photopeak window of 140 keV (width 15%), and an additional scatter window at 115 keV (width 20%).

All patients gave written consent to undergo radioligand therapy. The study protocol was approved by the local ethics committee of the Medical Faculty of the Ludwig-Maximilians-University Munich, which waived

Table 1 Characteristics of mCRPC patients included in this study

	P1	P2	P3	P4	P5	P6	P7	P8	P9	P10	P11
Age	66	68	47	61	73	63	82	83	79	67	88
Activity (GBq)	3.7	3.7	3.7	3.7	6.0	6.0	6.0	6.0	6.0	6.1	6.1
Cycle	1	1	1	1	1	1	1	5	1	1	1
Metastases (VIS = visceral, LYM = lymph, OSS = osseous)	OSS	Mainly VIS (liver), OSS, LYM	Mainly OSS, LYM	Mainly OSS, LYM	Mainly OSS, LYM	OSS, LYM	Mainly OSS, LYM, VIS	Mainly OSS, LYM, VIS	Mainly OSS, LYM	Mainly OSS, LYM	OSS
Initial TNM classification and Gleason score	pT4, N1, R1, G3, Gleason 8	pT3b, pN1, R0, G3, Gleason 9	pT3a, pN1, pR1, Gleason 9	pT3b, pN1, R1, Gleason 9	pT3b, pN1	T3a, N1	pT4, pN1, R1, G3, Gleason 9	pT4, pN1, R1, G3, Gleason 9	n.a.	pT3, pN0, R1, Gleason 7	n.a.
PSA (ng/ml) prior to RLT	1201	368	408	5436	2311	0.86	65.7	65.6	418	20.6	52.1
Pre-therapies (1, yes/0, no)											
▪ Surgery	1	0	1	1	1	1	1	1	1	1	0
▪ Radiotherapy	1	1	0	1	1	0	1	1	0	1	0
▪ Anti-hormonal therapy (including 2nd line anti-hormonal therapy with bicalutamide, enzalutamide, abiraterone acetate)	1	1	1	1	1	1	1	1	1	1	1
▪ Ra-223	1	0	1	0	0	0	0	0	0	1	0
▪ Chemotherapy (docetaxel, cabazitaxel)	1	1	1	1	1	1	0	0	1	1	0
Blood baseline											
▪ Leukocytes (G/l)	7.2	4.9	6	5.6	5.2	4.54	5.41	4.85	5.31	2.73	7.84
▪ Lymphocytes (G/l)	0.57	0.96	1.71	0.49	0.56	1.14	0.95	0.48	0.94	0.28	2.06
▪ Hemoglobin (g/dl)	14.1	12.3	12.8	9.6	10.9	13.3	10.5	8.4	10.5	8.3	12.1
▪ Thrombocytes (G/l)	195	307	323	291	235	227	450	305	223	89	281
▪ Erythrocytes (T/l)	4.79	4.31	4.36	4.08	3.86	4.11	3.96	3.25	3.55	3.2	3.64

the necessity for written consent for study entry, as the study is based on retrospective and irreversibly anonymized patient data.

Image reconstruction and quantification

Quantitative SPECT reconstruction was performed with an in-house maximum-a-posteriori reconstruction algorithm, which considers the correction for photon attenuation based on the co-registered low dose attenuation correction CT (AC-CT) (PMOD Version 3.609 rigid-body co-registration), correction for photon scattering based on the triple-energy-window (TEW) or dual-energy-window (DEW) method, and compensation of distance-dependent detector resolution using a Gaussian detector response model. Final quantification was realized by applying a system-specific calibration factor, which was determined from an identically imaged and reconstructed cylinder phantom of homogeneous and known activity concentration [15, 27, 29].

Quantitative reconstruction of Ga-68-PSMA-11 PET/CT scans was conducted as part of clinical routine using the TrueX algorithm with 3 iterations, 21 subsets, and a 3D post-reconstruction Gaussian filter with a full-width half maximum of 2 mm. The voxel volume in the PET data was $4.1 \times 4.1 \times 5.0 \text{ mm}^3$.

All Lu-177 planar whole-body images were corrected for photon attenuation and scattering pixel by pixel via an in-house MATLAB routine. Correction of photon attenuation was achieved via a patient-specific μ -map, which was generated from the whole-body CT of the pre-therapeutic Ga-68-PSMA-11 PET/CT acquisition, while the correction of photon scattering employed the TEW method. A patient-specific calibration factor was determined utilizing a cross-calibration with the corresponding quantitative SPECT at 24 h post-injection [28].

Reference bone marrow dosimetry using mass-scaled organ-level S values

Bone marrow dosimetry utilizing phantom-based organ-level S values was selected as reference method in this work. It considered the blood, both kidneys, and the remainder of body (ROB) as specific source regions [15–19, 28]. The respective S values of the RADAR standardized male anthropomorphic phantom were used [30]. All S values were scaled to the patient-specific anatomical conditions. The time-integrated activities for the blood and both kidneys were determined based on a bi-exponential and a mono-exponential fit to the available time-activity measurements, respectively. For determination of the blood-to-bone marrow absorbed dose, we employed a hematocrit-based red marrow-to-blood activity concentration ratio (RMBLR), as we assume no specific binding to bone marrow or blood cells [16, 28, 31]. This assumption results in a reduced

RMBLR compared to a RMBLR of one, which is typically employed for Lu-177 PRRT.

The derivation of the time-integrated activity of the ROB from a single planar whole-body scan was achieved by applying a suitable hybrid SPECT-planar model, which has been investigated in a previous study [28]. Briefly, a mono-exponential curve was fitted to the total SPECT activity over time, and this curve was scaled with the whole-body activity at 24 h p.i. afterwards to estimate the patient-specific whole-body time-activity curve. After integration over time, kidney and blood time-integrated activities were subtracted to obtain the number of decays within the ROB compartment [16]. As the patient-specific lesion distribution was highly variable for the patients investigated in this study, no pre-calculated S values were available, which consider all lesions in their size, shape, number, and location. Thus, the consideration of the metastases and their non-negligible activity uptake within the S value method was achieved by including the total lesion activity within the ROB compartment.

In a previous study, the contribution from the ROB including the lesion activities was found to be the dominating component of the total bone marrow absorbed dose [28]. However, the patient-specific lesion distribution is assumed to be only inadequately considered via classical S value dosimetry. To investigate differences between Monte-Carlo-based and classical S value bone marrow dosimetry, all bone marrow absorbed doses were correlated to the total bone lesion load, the time-integrated tumor uptake, and the time-integrated ROB retention (MATLAB Pearson's correlation). The total bone lesion load was obtained from the pre-therapeutic Ga-68-PSMA-11 PET via PMOD kmeans segmentation (PMOD Version 3.609), while time-integrated tumor uptake and ROB retention were derived by integrating both the mono-exponential ROB and lesion time-activity curves. To obtain a total-body lesion time-activity curve from the sequential abdominal SPECT, the assumption that the kinetics of all abdominal lesions is equivalent to that of all lesions throughout the patient body was made. The total-body lesion time-activity curve was then derived from all segmented tumors within the abdominal sequential SPECT (kmeans segmentation, PMOD Version 3.609), scaled with the ratio of total-to-abdominal lesion load.

Monte Carlo simulation of bone marrow absorbed dose

For each patient, the absorbed dose to the bone marrow was simulated using the FLUKA MC code, which has been extended and validated for applications in nuclear medicine, and which is capable to include the patient-specific 3D anatomical and activity imaging data [6, 11, 12, 32].

Anatomical and activity simulation data

The pre-therapeutic diagnostic CT from the Ga-68-PSMA-11 PET/CT scan served as patient-specific whole-body anatomical map during the Monte Carlo simulations. Therefore, the CT was converted to a voxel-wise map of density and anatomical composition as described by Botta et al. and as required by the MC code [6]. The patient-specific and time-dependent 3D whole-body Lu-177 activity distribution was described by combining the information contained in the sequential Lu-177 SPECT, the Lu-177 whole-body planar scintigraphy, and the whole-body PET/CT data. First, a patient-specific 3D whole-body volume of interest (VOI) map was generated by segmenting the kidneys, the tumors, and the ROB in the PET/CT volume. Using the sequential Lu-177 SPECT and the single Lu-177 whole-body planar scintigraphy, the activity in these compartments was assessed for each time point 24, 48, and 72 h post-injection. Therefore, kidney VOIs and the overall tumor load were semi-automatically segmented (kmeans segmentation, PMOD Version 3.609) from both the quantitative SPECT scan 24 h p.i. and the Ga-68-PSMA-11 PET. The segmented kidney VOIs were confirmed by visual comparison with the AC-CT and the diagnostic CT, respectively. Both, the 24-h-based SPECT kidney and tumor VOIs were then manually registered to the following imaging days 48 h and 72 h post-administration. The time-integrated activity per voxel was determined for both compartments, to directly assign a total number of decays per voxel to each VOI of the patient-specific activity template. Thereby, the abdominal lesion time-integrated activity was multiplied with the ratio of total-to-abdominal lesion volume to estimate the total lesion time-integrated activity from the sequential abdominal SPECT, as already described. The ROB time-integrated activity was defined via the mentioned hybrid SPECT-planar model [28], while the ROB VOI itself was derived from a VOI outlining the whole CT volume from the PET/CT data.

Absorbed dose to the bone marrow

For most of the skeletal sites, the bone marrow shows a heterogeneous microstructure composed of small marrow cavities containing a composition of active bone marrow (BM) and inactive bone marrow (iaBM), with these cavities being separated by the spongiosa, i.e., small ridges of hard bone (HB). This highly heterogeneous microstructure is not visible on routine clinical imaging modalities. Thus, for simulation and estimation of the bone marrow absorbed dose, we implemented a weighting factor-based model into the FLUKA code, similar to the two-factor mass-energy absorption coefficient method described by Lee et al. [33]. It estimates the absorbed dose to the active bone marrow from the

absorbed dose simulated within the total bone mixture, multiplied via a weighting factor w , which describes an effective interaction probability within the active bone marrow. This weighting factor can be calculated from the particle energy E of the dose-depositing photons or electrons; the fractions of active bone marrow, inactive bone marrow, and hard bone (f_{BM} , f_{iaBM} , and f_{HB} , respectively) present in the skeletal region of interest; the photon mass attenuation coefficients ($\frac{\mu}{\rho}$) or the electron mass stopping powers ($\frac{S}{\rho}$) of the skeletal constituents:

$$D_{BM} = D_{bone} \cdot w, \quad (1.1)$$

$$w = \frac{\frac{\mu_{BM}(E)}{\rho_{BM}}}{\frac{\mu_{bone}(E)}{\rho_{bone}}} \text{ or } w = \frac{\frac{S_{BM}(E)}{\rho_{BM}}}{\frac{S_{bone}(E)}{\rho_{bone}}}, \quad (1.2)$$

$$\begin{aligned} \mu_{bone}(E) &= f_{BM} \cdot \frac{\mu_{BM}}{\rho_{BM}} + f_{iaBM} \cdot \frac{\mu_{iaBM}(E)}{\rho_{iaBM}} + f_{HB} \cdot \frac{\mu_{HB}(E)}{\rho_{HB}} \text{ or} \\ S_{bone}(E) &= f_{BM} \cdot \frac{S_{BM}(E)}{\rho_{BM}} + f_{iaBM} \cdot \frac{S_{iaBM}(E)}{\rho_{iaBM}} + f_{HB} \cdot \frac{S_{HB}(E)}{\rho_{HB}}, \end{aligned} \quad (1.3)$$

$$\begin{aligned} f_{BM} &= \frac{m_{BM}}{m_{bone}} \text{ and in general } f_i \\ &= \frac{m_i}{m_{bone}}, \quad i \in \{BM, iaBM, HB\}, \end{aligned} \quad (1.4)$$

$$f_{BM} + f_{iaBM} + f_{HB} = 1. \quad (1.5)$$

f_{BM} , f_{iaBM} , and f_{HB} reference values were available for 13 active-marrow-bearing bone regions according to the ICRP 110 reference male [34]. For each patient, these 13 bone regions were segmented onto the patient-specific diagnostic CT from the Ga-68-PSMA-11 PET/CT, and the aforementioned reference fractions f_{BM} , f_{iaBM} , and f_{HB} were assigned to each voxel according to its region affiliation. To facilitate segmentation of these 13 regions for each patient, a bone region template was employed. Therefore, the whole skeleton of 5 patients was segmented via a HU threshold of 200 on the diagnostic CT from the Ga-68-PSMA-11 PET/CT, and the remaining holes in these skeletal VOIs were manually filled afterwards (PMOD Version 3.609). For template generation, the segmented bone VOIs from all five patients were co-registered onto each other using PMOD non-rigid co-registration. Finally, all 13 regions were manually segmented on this template. For each patient, the whole skeleton was segmented in the same manner as for template generation, and the region-specific template was non-rigidly co-registered onto each patient-specific skeletal VOI, to automatically define both the patient-specific bone region classification and the related

active bone marrow distribution containing reference values f_{BM} (Fig. 1).

This pre-defined active bone marrow distribution was used in two ways during Monte-Carlo-based bone marrow dosimetry. For model MC1, the active bone marrow distribution remained unchanged, assuming a co-localization of lesions and active bone marrow. For the second model MC2, all previously segmented lesion-containing voxels were removed from the active bone marrow distribution, to simulate the effect of a complete bone marrow displacement from the metastatic sites onto the absorbed dose estimates.

As for SMIRD, absorbed dose estimates were correlated to the bone lesion load, the time-integrated tumor uptake, and the time-integrated ROB retention (MATLAB Pearson's correlation).

Simulation

During simulation, photon production, and transport thresholds were set to 1 keV (mean range < 1 mm for all tissues [35]). The corresponding electron thresholds were chosen as 10 keV (mean range < 0.01 mm for all tissues). 10^9 decays were simulated for each simulation study.

Correlation with blood parameters

For the patients included in this study, all bone marrow absorbed doses were correlated (MATLAB Pearson's correlation) with the change of hematological parameters after the investigated therapy cycle (Table 1), i.e., the ratio of nadir-to-baseline values of platelet, lymphocyte, and leukocyte counts as well as of hemoglobin level. Particularly, the goal was to assess for the overall patient cohort whether patient-specific Monte-Carlo-based bone marrow dosimetry results in improved correlation with the hematological outcome compared to classical S value dosimetry.

Comparison of bone marrow absorbed doses

Bone marrow dosimetry estimates derived from the bone marrow models MC1, MC2, and SMIRD were compared among each other, and respective differences were further correlated with the bone lesion load, the time-

integrated tumor uptake, and the time-integrated ROB retention (MATLAB Pearson's correlation), to estimate which influencing factors of absorbed dose modeling define differences between the investigated models.

Bone marrow dosimetry using Tc-99m-anti-granulocyte antibody scintigraphy

Pre-therapeutic Ga-68-PSMA-11 PET and Tc-99m-anti-granulocyte antibody SPECT distributions were visually compared with respect to the overlap between tumor uptake and the accumulation in the Tc-99m-anti-granulocyte antibody scintigraphy. In a second step, the Tc-99m-anti-granulocyte antibody SPECT/CT was non-rigidly co-registered to the Ga-68-PSMA-11 PET/CT data (PMOD Version 3.609) and considered during the Monte Carlo absorbed dose calculation as active bone marrow VOI (gMC3). Respective absorbed dose estimates were compared with those from model MC1 for no bone marrow displacement from the direct location of metastasis, MC2 assuming full bone marrow displacement, and SMIRD.

Results

Reference bone marrow dosimetry using mass-scaled organ-level S values

Median bone marrow absorbed dose estimates as derived via S values (SMIRD) were found to be 11 mGy/GBq (6–25 mGy/GBq) (Table 2). Individual bone marrow absorbed doses showed a weak positive correlation with the bone lesion load ($r = 0.36$, $p = 0.27$, $R^2 = 0.13$). A strong positive correlation with the time-integrated ROB retention ($r = 0.87$, $p < 0.01$, $R^2 = 0.74$) and with the time-integrated tumor uptake ($r = 0.88$, $p < 0.01$, $R^2 = 0.75$) was found.

Analysis of blood parameters revealed a weak negative correlation of bone marrow absorbed dose estimates with the change of hemoglobin level ($r = -0.19$, $p = 0.60$, $R^2 = 0.04$). A moderate negative correlation was found for the change of lymphocyte counts ($r = -0.49$, $p = 0.15$, $R^2 = 0.24$) and total white blood cells ($r = -0.45$, $p = 0.20$, $R^2 = 0.20$), while the change of platelet counts showed a strong negative correlation ($r = -0.62$, $p = 0.04$, $R^2 = 0.38$) (Fig. 2).

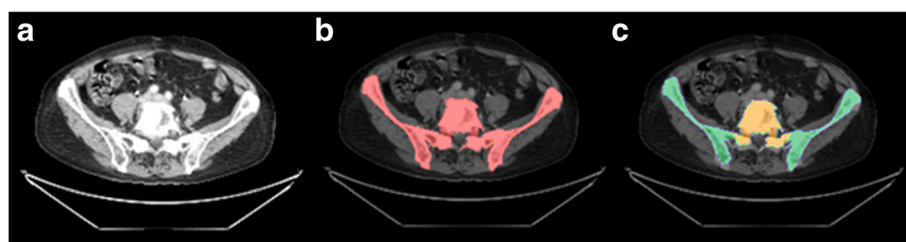
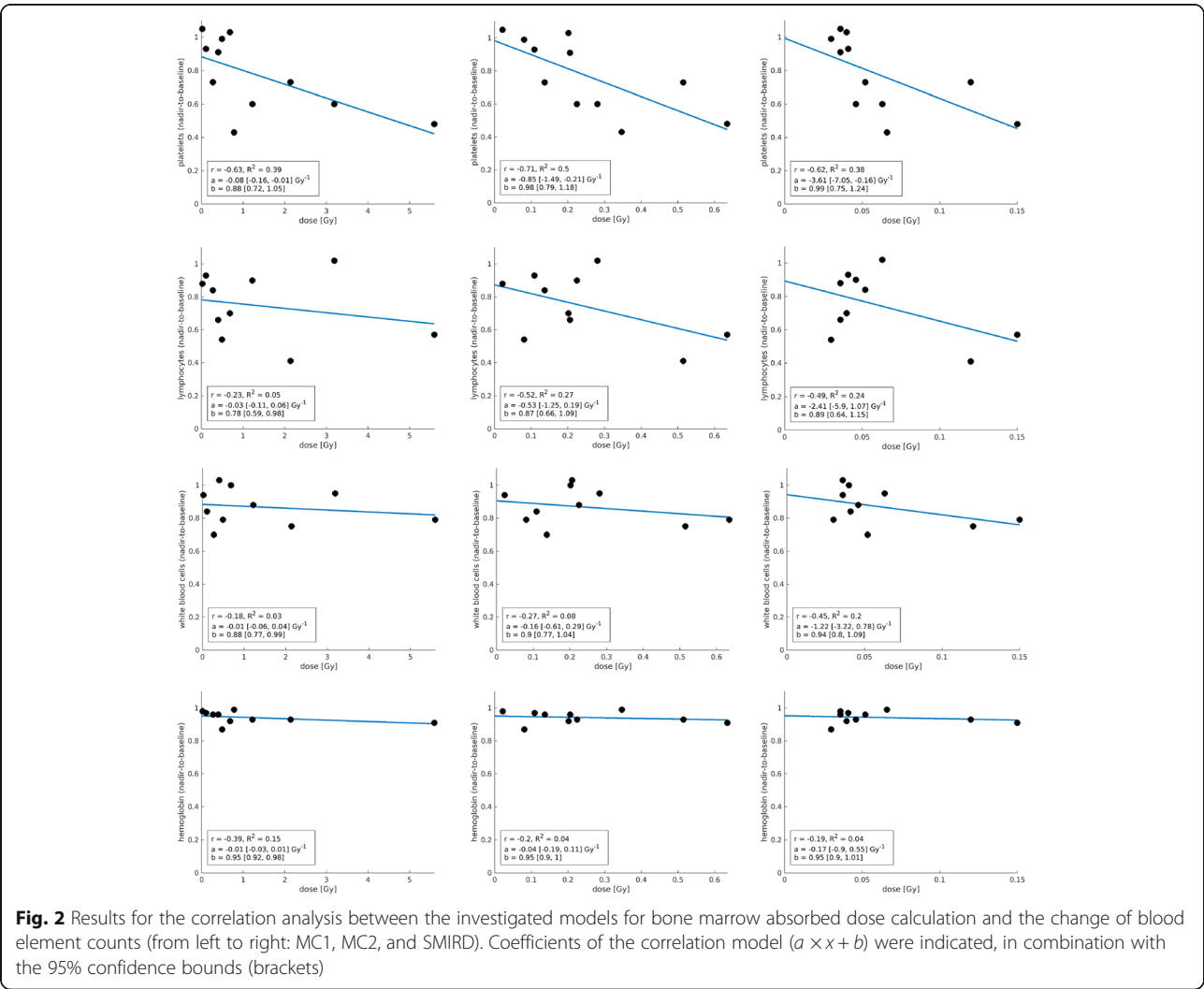


Fig. 1 Exemplary workflow for definition of skeletal compositions. **a** Exemplary patient CT. **b** Semi-automatic segmentation of patient-specific bone VOI. **c** Automatic definition of bone regions from non-rigidly co-registered template

Table 2 Bone marrow absorbed dose estimates as derived either using *S* values (SMIRD), Monte Carlo simulations under the assumption of a physiological active bone marrow distribution (MC1), or Monte Carlo simulations assuming no active bone marrow at the direct location of the bone lesions (MC2)

Patient (administered activity in GBq)	SMIRD (mGy)	MC1 (mGy)	MC2 (mGy)	Bone lesion load (ml)	Time-integrated tumor uptake (GBq × s/ml)	Time-integrated ROB retention (GBq × s/ml)
P1 (3.7)	30	493	81	402	141	3
P2 (3.7)	41	109	109	33	87	4
P3 (3.7)	52	274	137	448	59	5
P4 (3.7)	63	3192	281	1123	609	4
P5 (6.0)	120	2139	515	1124	523	17
P6 (6.0)	36	22	22	50	91	6
P7 (6.0)	150	5595	635	727	1130	26
P8 (6.0)	46	1123	225	1298	159	10
P9 (6.0)	40	684	202	836	128	9
P10 (6.1)	66	782	347	1383	84	17
P11 (6.1)	36	403	206	467	64	9

Additionally, bone lesion load, time-integrated tumor uptake, and ROB retention are provided for each patient



Monte Carlo simulation of bone marrow absorbed dose

Under the assumption of an unaltered and physiological active bone marrow distribution (MC1), median absorbed dose estimates were found to be 130 mGy/GBq (4–933 mGy/GBq) (Table 2). Further, for model MC1, a weak positive correlation with the bone lesion volume ($r = 0.38$, $p = 0.24$, $R^2 = 0.15$), while a strong up to very strong positive correlation with the time-integrated ROB retention ($r = 0.71$, $p = 0.01$, $R^2 = 0.50$) and time-integrated tumor uptake ($r = 0.98$, $p < 0.01$, $R^2 = 0.97$) was observed. Analysis of blood parameters revealed a weak negative correlation with the change of lymphocyte counts ($r = -0.23$, $p = 0.52$, $R^2 = 0.05$), total white blood cells ($r = -0.18$, $p = 0.61$, $R^2 = 0.03$), and hemoglobin level ($r = -0.39$, $p = 0.26$, $R^2 = 0.15$). A strong negative correlation for the change of platelet counts ($r = -0.63$, $p = 0.04$, $R^2 = 0.38$) was found (Fig. 2).

For model MC2, which assumes a full displacement of active bone marrow from the direct location of each lesion, median bone marrow absorbed dose estimates were 37 mGy/GBq (4–106 mGy/GBq) (Table 2). For MC2, a moderate positive correlation with the bone lesion volume was found ($r = 0.58$, $p = 0.06$, $R^2 = 0.33$), while a strong up to very strong positive correlation with the time-integrated tumor uptake and ROB retention was observed ($r = 0.82$, $p < 0.01$, $R^2 = 0.68$ and $r = 0.92$, $p < 0.01$, $R^2 = 0.84$). Concerning the blood parameters, a weak negative correlation was found for the change of hemoglobin level ($r = -0.20$,

$p = 0.59$, $R^2 = 0.04$) and total white blood cells ($r = -0.27$, $p = 0.44$, $R^2 = 0.08$), while lymphocyte counts ($r = -0.52$, $p = 0.13$, $R^2 = 0.27$) showed a moderate negative correlation. Analysis of the change of platelet counts showed a strong negative correlation ($r = -0.71$, $p = 0.01$, $R^2 = 0.50$) (Fig. 2).

Exemplary simulation results are provided in Fig. 3 for patients 3, 4, 8, and 9. Patients 4 and 8 present with a comparable bone lesion load; however, a clearly higher bone marrow absorbed dose was observed for patient 4 and particularly MC1, due to a fourfold higher time-integrated tumor uptake (Table 2).

Comparison of bone marrow absorbed doses

The median ratio between models MC1 and SMIRD was a factor of 17 (1–50) (Table 3). The highest differences were observed for patients 4, 7, and 8, who showed a combination of a comparatively high bone lesion volume, a high time-integrated tumor uptake, and a high ratio of time-integrated tumor uptake to ROB retention (Table 3). The lowest differences were found for patients 2, 3, and 6. Patients 2 and 6 showed the lowest bone lesion volume (< 50 ml), while for patient 3 both a comparatively low tumor uptake and ROB retention were observed (Table 3). In general, the differences between MC1 and SMIRD were mainly driven by the time-integrated tumor uptake and the bone lesion volume, respectively ($r = 0.77$, $p < 0.01$, $R^2 = 0.59$, and $r = 0.60$, $p = 0.05$, $R^2 = 0.36$).

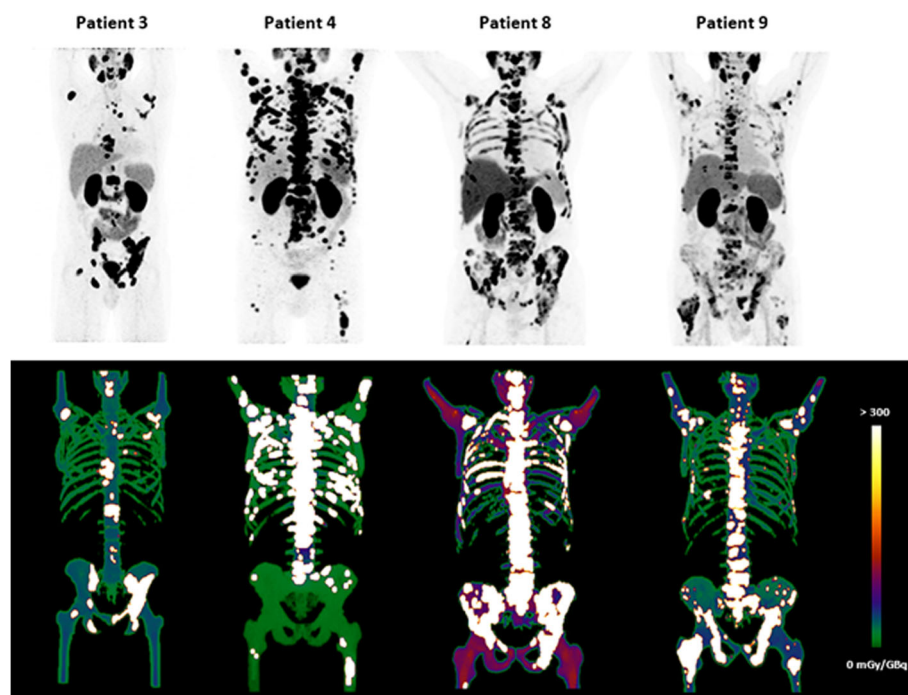


Fig. 3 Exemplary Monte Carlo simulation results for patients 3, 4, 8, and 9. Upper row: MIP from pre-therapeutic Ga-68-PSMA-11 PET/CT; lower row: MIP for simulated absorbed dose within the bone marrow

Table 3 Ratio of bone marrow absorbed dose estimates based on Monte Carlo simulations and *S* values

Patient	MC1/SMIRD	MC2/SMIRD	MC1/MC2
P1	17	3	6
P2	3	3	1
P3	5	3	2
P4	50	4	11
P5	18	4	4
P6	1	1	1
P7	37	4	9
P8	27	5	5
P9	17	5	3
P10	12	5	2
P11	11	6	2
Median	17	4	3

The comparison between model MC2 and SMIRD revealed a median ratio of 4 (1–6) (Table 3). The lowest difference was obtained again for patient 6, while all other patients showed a similar deviation by a factor of 3 to 6, whereupon the differences between MC2 and SMIRD mainly show a strong positive correlation with the bone lesion volume ($r = 0.63$, $p = 0.04$, $R^2 = 0.40$).

The median ratio of MC1 to MC2 was found to be 3 (1–11), with the highest differences being found for patients 4 and 7, which both show the highest time-integrated tumor uptake (Table 3). In addition, a strong positive correlation between the ratios MC1 to MC2 with the time-integrated tumor uptake was found ($r = 0.78$, $p < 0.01$, $R^2 = 0.61$).

Bone marrow dosimetry using Tc-99m-anti-granulocyte antibody scintigraphy

For patients 8 and 9, bone marrow absorbed dose estimates were re-analyzed using the Tc-99m-anti-granulocyte-based active bone marrow VOI (gMC3). For patient 8, MC1 and MC2 revealed a bone marrow absorbed dose of 1223 and 225 mGy, respectively, compared to 46 mGy for SMIRD. For the Tc-99m-anti-granulocyte-based VOI, an absorbed dose of 718 mGy was found, i.e., a reduction of approximately 41% compared to MC1. The ratio of model gMC3 compared to MC2 and SMIRD was found to be 3 and 17, respectively (Table 4). For patient 9, absorbed dose estimates for MC1, MC2, and SMIRD were found to be 684, 202, and 40 mGy, respectively. Applying the Tc-99m-anti-granulocyte-based

VOI yielded a bone marrow absorbed dose of 408 mGy. Thus, compared to MC1, the bone marrow absorbed dose decreased by 40%, while gMC3 produced two- and tenfold higher absorbed dose estimates compared to MC2 and SMIRD (Table 4).

Furthermore, visual interpretation of Ga-68-PSMA-11 PET and Tc-99m-anti-granulocyte antibody scintigraphy indicates a low overlap between accumulation patterns and a displacement of active bone marrow from metastatic lesions for both investigated patients (Figs. 4 and 5).

Discussion

The bone marrow is potentially the most critical organ and most limiting factor of the therapeutic window during Lu-177-PSMA therapy of mCRPC patients, as those patients are usually heavily pre-treated and often present with a considerable bone lesion load [14]. In a study of Rahbar et al. with 145 patients and an average administered activity of 5.9 GBq per cycle, hematotoxicity showed the highest incidence for all grades as well as for grade 3–4 events [36]. Thus, bone marrow dosimetry is highly recommended in those patients. However, for bone marrow dosimetry to become predictive for hematotoxicity, all relevant patient-specific parameters must be considered. These include the patient-specific activity accumulation over time, the anatomical characteristics, an appropriate localization of the bone marrow target region, and, not least, pre-therapies and the patient-specific disease and hematological baseline status.

This study focuses on three relevant issues: First, we developed an approach for Monte-Carlo-based absorbed dose calculations, which can fully consider the patient-specific 3D activity and anatomical characteristics in contrast to the classical *S* value dosimetry. Second, we compared the effect of different models for active bone marrow localization during Monte-Carlo-based bone marrow dosimetry. The latter aspect is especially linked to the question whether patient-specific active bone marrow localization, e.g., via Tc-99m-anti-granulocyte scintigraphy, might be beneficial to avoid bone marrow toxicity. Third, we investigated whether for the patient cohort under study, Monte-Carlo-based absorbed dose calculation shows an improved correlation with the change of hematological parameters, and whether fully patient-specific bone marrow dosimetry can potentially provide an improved prediction for hematotoxicities.

Table 4 Comparison of bone marrow absorbed dose estimates based on Monte Carlo simulations for patients 8 and 9

Patient	MC1 (mGy)	MC2 (mGy)	gMC3 (mGy)	SMIRD (mGy)
P8	1223	225	718	46
P9	684	202	408	40

gMC3 uses the patient-specific Tc-99m-anti-granulocyte-based active bone marrow VOI. MC1 assumes a physiological active bone marrow distribution, while MC2 assumes a physiological distribution, however with displacement of active bone marrow from the direct site of metastases

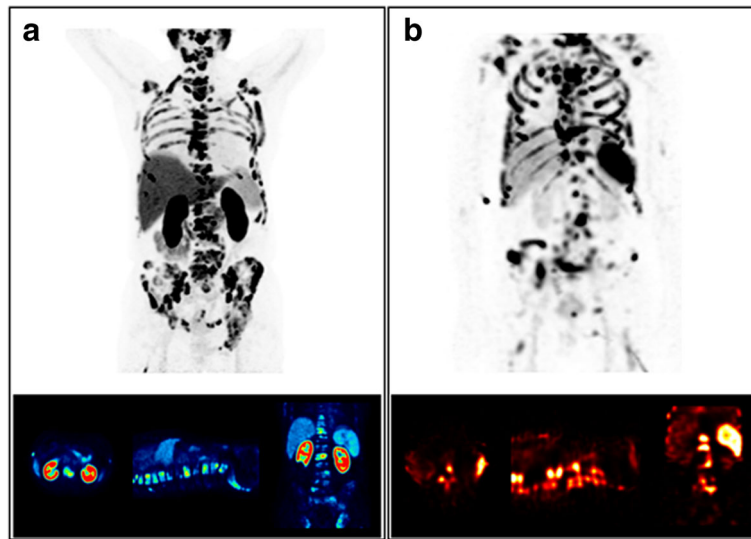


Fig. 4 Results from Tc-99m-anti-granulocyte antibody SPECT/CT (**b**) in comparison to the Ga-68-PSMA-11 PET/CT (**a**) for patient 8

Although the number of patients investigated in this study is low, our preliminary results already indicate a large range between bone marrow absorbed dose estimates for Monte Carlo and *S* value calculations. The model-specific correlation of bone marrow absorbed dose estimates with segmented bone lesion volume, time-integrated tumor uptake, and ROB retention, as performed during this study, supports that multiple patient-specific factors should be taken into consideration to reduce the uncertainty of bone marrow dosimetry. SMIRD-based bone marrow dosimetry mainly accounts for the time-integrated ROB and lesion uptake characteristics; however, respective absorbed doses

revealed only a weak correlation with the patient-specific and highly heterogeneous 3D bone lesion distribution. For MC2-based absorbed dose estimates, a strong and significant correlation with tumor uptake, ROB retention, and bone lesion volume was found, while bone marrow absorbed dose calculations during model MC1 are clearly dominated by the time-integrated tumor uptake. Results from correlation analysis support that also for 3D-based absorbed dose calculation, the total bone lesion volume is not the only influencing factor of the bone marrow absorbed dose, and risk patients should be stratified according to multiple parameters.

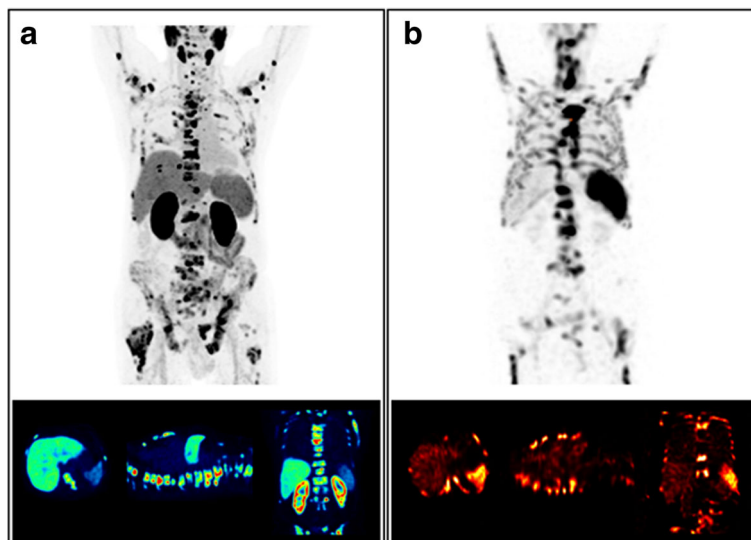


Fig. 5 Results from Tc-99m-anti-granulocyte antibody SPECT/CT (**b**) in comparison to the Ga-68-PSMA-11 PET/CT (**a**) for patient 9

With respect to the absolute values, patient-specific Monte-Carlo-based calculations resulted in higher bone marrow absorbed doses than the classical S value approach. For both models, MC2 and SMIRD, bone marrow absorbed dose estimates were well below the typically applied threshold of 2 Gy [19]. Although for MC2 the absorbed dose estimates were on median four-fold higher than those achieved with the reference model SMIRD, the deduction that multiple therapy cycles are applicable for these patients without the risk of severe marrow toxicities seems reasonable, at least with regard to the current dose limit. However, the assumption of full displacement of active bone marrow, as included in model MC2, might not be *a priori* justified in each patient and might lead to an underestimation of the bone marrow absorbed dose. For model MC1, assuming a physiological and unaltered active bone marrow distribution, median absorbed doses of 130 mGy/GBq were found with on median 17-fold and 3-fold higher absorbed dose estimates compared to SMIRD and MC2, respectively. According to dosimetry using model MC1, patients 4, 5, 7, and 8 would have received a bone marrow absorbed dose close to or in some cases even strongly exceeding the 2 Gy limit, with the consequent risk for severe marrow toxicities in these patients. However, none of the patients presented severe marrow damage, even after multiple therapy cycles. This observation questions the general applicability and significance of models like MC1, which do not account for bone marrow displacement by tumor lesions, especially in the presence of a heavy skeletal tumor burden.

Visual analysis of Tc-99m-anti-granulocyte antibody SPECT scans supports this thesis, as it indicates a displacement of active bone marrow from the direct location of bone lesions for both exemplarily investigated patients. In these patients, the re-analysis of bone marrow absorbed dose estimates using the individual Tc-99m-anti-granulocyte-based active bone marrow VOIs resulted in a clear absorbed dose reduction of approximately 40% compared to MC1, although the absorbed dose values were still higher than those from MC2. However, both the Ga-68-PSMA-11 PET and the Tc-99m-anti-granulocyte antibody SPECT have a finite resolution, which intrinsically results in a certain artificial overlap of both activity distributions and thus in an increased absorbed dose estimate compared to MC2. Furthermore, co-registration between both modalities is in general not perfect, particularly for challenging regions such as the ribs or the sternum, which might additionally cause a local overlap between tumor and bone marrow accumulation. Both finite spatial resolution and imperfect co-registration interfere with a potential incomplete active bone marrow displacement. Despite the additional complexity introduced by the

finite resolution of the involved imaging systems and by the imperfect co-registration, the utilization of the additional image data from the Tc-99m-anti-granulocyte antibody scintigraphy may improve individualized bone marrow dosimetry by providing a realistic upper limit for the bone marrow absorbed dose. For patient 8, the usage of a Tc-99m-anti-granulocyte-based VOI resulted in a reduction of a total bone marrow absorbed dose from 1.1 Gy (MC1) to an expected maximum dose of 0.7 Gy. It may be hypothesized that the typically applied upper limit for the bone marrow absorbed dose of 2 Gy is too high for patients with advanced cancer disease, extensive skeletal tumor burden, and potentially decreased hematological function due to various pre-therapies. Despite the relatively small additional bone marrow absorbed dose (approx. 10 mSv for 400 MBq), Tc-99m-anti-granulocyte antibody scintigraphy might be justified in such patients. Studies based on a larger patient cohort are needed to identify, whether image-based active bone marrow localization in combination with Monte-Carlo-based absorbed dose calculation really improves the correlation between bone marrow dosimetry and hematotoxicities, and may therefore be suitable to guide therapy planning in future workflows. Still, the comparison between models MC1 and MC2 demonstrates that the *a priori* unknown patient-specific active bone marrow distribution results in a large uncertainty of the bone marrow absorbed doses, even if Monte Carlo techniques are applied for absorbed dose modeling. Further, future studies should be performed to find an appropriate threshold for the bone marrow absorbed dose for Lu-177-PSMA therapy [14].

The resolution of non-invasive active bone marrow localization could be further improved by MRI bone marrow localization, which would also be beneficial if even small additional contributions to the bone marrow absorbed dose must be avoided [24, 25]. However, in clinical daily routine, the localization of active bone marrow in a large part of the patient body should be feasible with acceptable measurement and processing time, and it should be available for several patients per week. Further, a reduction of processing complexity and effort accompanied by a potential enhancement of the accuracy of the derived information is desirable. This could be achieved, for instance, by employing a standardized method for patient positioning over multiple scans at the same or at different imaging modalities via patient-adaptable storage mattresses, which facilitates image co-registration [37].

To derive a patient-specific activity template from the Ga-68-PSMA-11 PET instead from the Lu-177-SPECT reduces issues of spatial resolution during absorbed dose calculation. Further, for the patients considered in this study, only SPECT acquisitions of the abdomen were

available, while for bone marrow dosimetry, the lesion distribution in the overall body is important. Using the Ga-68-PSMA-11 PET to model the 3D activity accumulation during therapy is an approximation and only applicable if the delay between PET acquisition and therapy is small (on average 2.5 weeks in this study) and if there is no change in the overall lesion load. To switch to a fully Lu-177-based activity template, further investigations are desired to improve the spatial resolution of the Lu-177 imaging and to enable a fast whole-body Lu-177-SPECT acquisition. Filling a fixed patient-specific activity VOI template with the respective segmented VOI activities from sequential Lu-177 imaging reduces co-registration errors, which could otherwise lead to an artificially increased bone marrow absorbed dose.

The analysis of blood parameters revealed a significant ($p < 0.05$) and strong negative correlation only for the change of platelet counts, irrespective of the exact bone marrow model used. The highest correlation was obtained with model MC2, which includes the assumption of full displacement of active bone marrow from the direct site of the bone lesions. To exploit the potential and impact of bone marrow dosimetry for therapy planning, a more comprehensive investigation of the correlation of the change of blood element counts with bone marrow absorbed dose estimates is desired. For this purpose, blood analysis should consider a higher number of patients and a prolonged time period. Both the baseline hematological status and its course after therapy are known to be affected by various parameters, such as pretherapies or total lesion volume [17, 38–40]. Thus, a patient stratification as for example proposed by Walrand et al. is mandatory, if the correlation between bone marrow absorbed doses and hematological response to therapy shall be analyzed [40]. So far, the correlation of bone marrow absorbed doses and blood parameters for different Lu-177-based radioligand therapies was assessed using *S* value-based methods. Svensson et al. observed moderate and significant correlations for the decrease of hemoglobin level, total white blood cells, and platelet counts for Lu-177 PRRT and for 46 investigated patients [17]. By contrast, Forrer et al. found no correlation between the decrease of platelet counts and bone marrow absorbed dose estimates for Lu-177 PRRT based on 15 patients and monitoring of hematological function until 6 weeks after treatment [18].

In clinical routine, the application of Monte Carlo simulations for dose calculations may be too time-consuming, especially if the simulation has to consider a large part of the patient body and small voxels (e.g., 0.05–0.001 ccm). However, Monte Carlo simulations can be made feasible with computing clusters. In this way, results with a high statistical validity could be obtained in 1 day, which is acceptable with respect to the time

gap between successive cycles of radioligand therapy. An intermediate method for fast 3D dosimetry within minutes, which compromises the consideration of Monte Carlo techniques and computational effectiveness, is the application of Monte-Carlo-based dose kernels [41, 42]. Further investigations of this approach may be advisable to prospectively facilitate improved clinical dosimetry for monitoring and planning of radioligand therapies.

In this work, we introduced a weighting-based model to represent the different compartments of active and inactive bone marrow and hard bone. This model represents a reasonable simplification for the application to clinical routine imaging data, which have a spatial resolution above the characteristic size of the bone marrow microstructure. Hybrid Monte-Carlo-based models that alternate between macroscopic models of the overall patient anatomy and detailed microscopic models of the skeletal system are time-consuming but might further improve bone marrow absorbed dose estimates, at least for the understanding of important mechanisms to assess risk factors for marrow toxicities [34, 43].

Conclusion

Monte-Carlo-based bone marrow absorbed doses were found to be significantly increased compared to those derived from classical *S* value dosimetry. Particularly, a large spread between Monte-Carlo-based and *S* value bone marrow absorbed doses was observed, which implies a large uncertainty, especially for *S* value dosimetry due to the lack of an appropriate consideration of the patient-specific highly heterogeneous 3D lesion distribution. However, even for Monte-Carlo-based bone marrow dosimetry, the a priori unknown patient-specific active bone marrow distribution produces a large uncertainty of bone marrow absorbed doses. Assuming a colocalization between active bone marrow and all lesions (MC1) is hypothesized to lead to too exaggerated absorbed dose values (> 2 Gy per cycle for 27% of investigated cycles), as these values were not in concordance with the observation of severe hematological toxicities. Simultaneously, the a priori assumption of a full displacement of active bone marrow for each patient (MC2) might underestimate the patient-specific absorbed dose. Patient-specific image-based active marrow localization, as performed for a small subgroup of patients, yielded to intermediate bone marrow absorbed doses compared to MC1 and MC2, although issues of co-registration and finite image resolution might interfere with incomplete active bone marrow displacement. Future studies based on a larger patient cohort are recommended, to particularly determine whether patient-specific active bone marrow localization in combination with Monte-Carlo-based absorbed dose modeling can improve the prediction of hematotoxicities and thus

enables to exploit the full therapeutic window of Lu-177-PSMA therapy. Preliminary results showed a significant and strong correlation between platelet decrease and bone marrow absorbed doses, irrespective of the exact dosimetry model; however, highest correlation was observed for MC2.

Abbreviations

AC-CT: Low dose attenuation correction CT; BM: Bone marrow; CT: Computed tomography; ICRP: Internal Commission on Radiological Protection; MC: Monte Carlo; mCRPC: Metastasized castration-resistant prostate cancer; MIRD: Medical Internal Radiation Dose (Committee); PET: Positron emission tomography; PRRT: Peptide receptor radionuclide therapy; PSMA: Prostate-specific membrane antigen; RADAR: Radiation Dose Assessment Resource; ROB: Remainder of the body; SPECT: Single-photon emission computed tomography; VOI: Volume of interest

Acknowledgements

Not applicable.

Authors' contributions

AG, HI, AT, PB, SZ, and GB contributed to the concept and design of the study. AG, HI, ST, JB, and LK carried out all the data analysis. AM and KP provided the FLUKA MC code. FJG was responsible for the radiopharmaceutical production. All authors contributed to the draft of the manuscript. All authors read and approved the manuscript.

Funding

This work was partly funded by the German Research Foundation (DFG) within the Research Training 381 Group GRK 2274.

Availability of data and materials

Please contact the corresponding author for data request.

Ethics approval and consent to participate

This study is based on retrospective and anonymized data, which was acquired for routine clinical dosimetry (Ethics Committee of LMU Munich).

Consent for publication

Not applicable.

Competing interests

The authors declare that they have no competing interests.

Author details

¹Department of Nuclear Medicine, University Hospital, LMU Munich, Marchioninistrasse 15, 81377 Munich, Germany. ²Heidelberg Ion Beam Therapy Center, University Hospital Heidelberg, Heidelberg, Germany. ³Department of Medical Physics, Ludwig-Maximilians-Universität München, Garching b. München, Germany.

Received: 14 May 2019 Accepted: 30 July 2019

Published online: 14 August 2019

References

1. Stabin M, Flux G. Internal dosimetry as a tool for radiation protection of the patient in nuclear medicine. *Biomedical Imaging and Intervention Journal*. 2007;**3**(2):e28.
2. Ljungberg M, Sjögreen-Gleisner K. The accuracy of absorbed dose estimates in tumours determined by quantitative SPECT: a Monte Carlo study. *Acta oncologica*. 2011;**50**(6):981–9.
3. Grimes J, Celler A. Comparison of internal dose estimates obtained using organ-level, voxel S value, and Monte Carlo techniques. *Medical physics*. 2014;**41**(9):092501.
4. Cremonesi M, et al. Dosimetry in peptide radionuclide receptor therapy: a review. *Journal of nuclear medicine*. 2006;**47**(9):1467–75.
5. Bolch WE, et al. MIRD pamphlet no. 21: a generalized schema for radiopharmaceutical dosimetry—standardization of nomenclature. *Journal of Nuclear Medicine*. 2009;**50**(3):477–84.
6. Botta F, et al. Use of the FLUKA Monte Carlo code for 3D patient-specific dosimetry on PET-CT and SPECT-CT images. *Physics in Medicine & Biology*. 2013;**58**(22):8099.
7. Kost SD, et al. VIDA: a voxel-based dosimetry method for targeted radionuclide therapy using Geant4. *Cancer Biotherapy and Radiopharmaceuticals*. 2015;**30**(1):16–26.
8. Ljungberg M, et al. 3D absorbed dose calculations based on SPECT: evaluation for ¹¹¹In-90Y therapy using Monte Carlo simulations. *Cancer Biotherapy and Radiopharmaceuticals*. 2003;**18**(1):99–107.
9. Ljungberg M, et al. A 3-dimensional absorbed dose calculation method based on quantitative SPECT for radionuclide therapy: evaluation for ¹³¹I using Monte Carlo simulation. *Journal of Nuclear Medicine*. 2002;**43**(8):1101–9.
10. Chiavassa S, et al. OEDIPE: a personalized dosimetric tool associating voxel-based models with MCNPX. *Cancer biotherapy & radiopharmaceuticals*. 2005;**20**(3):325–32.
11. Fasso, A., et al. FLUKA: a multi-particle transport code. 2005, CERN-2005-10.
12. Böhlen T, et al. The FLUKA code: developments and challenges for high energy and medical applications. *Nuclear data sheets*. 2014;**120**:211–4.
13. Baum RP, et al. Lutetium-177 PSMA radioligand therapy of metastatic castration-resistant prostate cancer: safety and efficacy. *Journal of Nuclear Medicine*. 2016. jnumed. 115.168443.
14. Kabasakal L, et al. Lu-177-PSMA-617 prostate-specific membrane antigen inhibitor therapy in patients with castration-resistant prostate cancer: stability, bio-distribution and dosimetry. *Molecular imaging and radionuclide therapy*. 2017;**26**(2):62.
15. Delker A, et al. Dosimetry for 177 Lu-DKFZ-PSMA-617: a new radiopharmaceutical for the treatment of metastatic prostate cancer. *European journal of nuclear medicine and molecular imaging*. 2016;**43**(1): 42–51.
16. Hindorf C, et al. EANM Dosimetry Committee guidelines for bone marrow and whole-body dosimetry. *European journal of nuclear medicine and molecular imaging*. 2010;**37**(6):1238–50.
17. Svensson J, et al. A novel planar image-based method for bone marrow dosimetry in 177 Lu-DOTATATE treatment correlates with haematological toxicity. *EJNMMI physics*. 2016;**3**(1):21.
18. Forrer F, et al. Bone marrow dosimetry in peptide receptor radionuclide therapy with [¹⁷⁷Lu-DOTA 0, Tyr 3] octreotate. *European journal of nuclear medicine and molecular imaging*. 2009;**36**(7):1138.
19. Sandström M, et al. Individualized dosimetry of kidney and bone marrow in patients undergoing 177Lu-DOTA-octreotate treatment. *Journal of Nuclear Medicine*. 2013;**54**(1):33–41.
20. Logothetis CJ, Lin S-H. Osteoblasts in prostate cancer metastasis to bone. *Nature Reviews Cancer*. 2005;**5**(1):21.
21. Morrissey C, Vessella RL. The role of tumor microenvironment in prostate cancer bone metastasis. *Journal of cellular biochemistry*. 2007;**101**(4):873–86.
22. Agool A, et al. Radionuclide imaging of bone marrow disorders. *European journal of nuclear medicine and molecular imaging*. 2011;**38**(1):166–78.
23. Berg BCV, et al. Magnetic resonance imaging of the normal bone marrow. *Skeletal radiology*. 1998;**27**(9):471–83.
24. Mouloupos LA, Dimopoulos MA. Magnetic resonance imaging of the bone marrow in hematologic malignancies. *Blood*. 1997;**90**(6):2127–47.
25. Pichardo JC, Milner RJ, Bolch WE. MRI measurement of bone marrow cellularity for radiation dosimetry. *Journal of Nuclear Medicine*. 2011;**52**(9):1482–9.
26. Fendler WP, et al. Preliminary experience with dosimetry, response and patient reported outcome after 177Lu-PSMA-617 therapy for metastatic castration-resistant prostate cancer. *Oncotarget*. 2017;**8**(2):3581.
27. Ljungberg M, et al. MIRD pamphlet no. 26: joint EANM/MIRD guidelines for quantitative 177Lu SPECT applied for dosimetry of radiopharmaceutical therapy. *Journal of nuclear medicine*. 2016;**57**(1):151–62.
28. Gosewisch A, et al. Patient-specific image-based bone marrow dosimetry in Lu-177-[DOTA 0, Tyr 3]-Octreotate and Lu-177-DKFZ-PSMA-617 therapy: investigation of a new hybrid image approach. *EJNMMI research*. 2018;**8**(1):76.
29. Dewaraja YK, et al. MIRD pamphlet no. 23: quantitative SPECT for patient-specific 3-dimensional dosimetry in internal radionuclide therapy. *Journal of Nuclear Medicine*. 2012;**53**(8):1310–25.
30. Stabin MG, et al. RADAR reference adult, pediatric, and pregnant female phantom series for internal and external dosimetry. *Journal of Nuclear Medicine*. 2012;**53**(11):1807–13.
31. Herrmann K, et al. Biodistribution and radiation dosimetry for a probe targeting prostate-specific membrane antigen for imaging and therapy. *Journal of Nuclear Medicine*. 2015;**56**(6):855–61.

32. Parodi K, et al. Clinical CT-based calculations of dose and positron emitter distributions in proton therapy using the FLUKA Monte Carlo code. *Physics in Medicine & Biology*. 2007;**52**(12):3369.
33. Lee C, et al. An assessment of bone marrow and bone endosteum dosimetry methods for photon sources. *Physics in Medicine & Biology*. 2006;**51**(21):5391.
34. Hough M, et al. An image-based skeletal dosimetry model for the ICRP reference adult male—internal electron sources. *Physics in Medicine & Biology*. 2011;**56**(8):2309.
35. <https://www.nist.gov/pml/stopping-power-range-tables-electrons-protons-and-helium-ions>.
36. Rahbar K, et al. German multicenter study investigating ¹⁷⁷Lu-PSMA-617 radioligand therapy in advanced prostate cancer patients. *Journal of Nuclear Medicine*. 2017;**58**(1):85–90.
37. Förster GJ, et al. SPET/CT image co-registration in the abdomen with a simple and cost-effective tool. *European journal of nuclear medicine and molecular imaging*. 2003;**30**(1):32–9.
38. Bodei L, et al. Long-term tolerability of PRRT in 807 patients with neuroendocrine tumours: the value and limitations of clinical factors. *European journal of nuclear medicine and molecular imaging*. 2015;**42**(1):5–19.
39. Bergsma H, et al. Subacute haematotoxicity after PRRT with ¹⁷⁷Lu-DOTA-octreotate: prognostic factors, incidence and course. *European journal of nuclear medicine and molecular imaging*. 2016;**43**(3):453–63.
40. Walrand S, et al. Experimental facts supporting a red marrow uptake due to radiometal transchelation in ⁹⁰Y-DOTATOC therapy and relationship to the decrease of platelet counts. *European journal of nuclear medicine and molecular imaging*. 2011;**38**(7):1270–80.
41. Sanchez-Garcia M, et al. Implementation and validation of collapsed cone superposition for radiopharmaceutical dosimetry of photon emitters. *Physics in Medicine & Biology*. 2015;**60**(20):7861.
42. Sanchez-Garcia M, et al. A new approach for dose calculation in targeted radionuclide therapy (TRT) based on collapsed cone superposition: validation with ⁹⁰Y. *Physics in Medicine & Biology*. 2014;**59**(17):4769.
43. Shah AP, et al. A paired-image radiation transport model for skeletal dosimetry. *Journal of Nuclear Medicine*. 2005;**46**(2):344–53.

Publisher's Note

Springer Nature remains neutral with regard to jurisdictional claims in published maps and institutional affiliations.

Submit your manuscript to a SpringerOpen[®] journal and benefit from:

- Convenient online submission
- Rigorous peer review
- Open access: articles freely available online
- High visibility within the field
- Retaining the copyright to your article

Submit your next manuscript at ► [springeropen.com](https://www.springeropen.com)

Danksagung

Zuallererst möchte ich mich bei meinem Doktorvater Priv. Doz. Dr. Guido Böning bedanken, für seine fortwährende Förderung und sein entgegengebrachtes Vertrauen. Guido hat mich stets dabei unterstützt eigene Forschungsansätze zu verfolgen, und stand mir mit seiner Erfahrung bei Fragen und Anliegen aller Art immer zur Seite. In vielen anregenden Diskussionen - mit oder ohne Weißwurst-Verpflegung - haben wir zusammen Lösungen gesucht, um die Dosimetrie ein Stück weiter voran zu bringen. Die Zeit der Promotion hat mich sehr geprägt und wird mir stets in sehr positiver Erinnerung bleiben.

Bei Prof. Dr. Bartenstein bedanke ich mich für die Möglichkeit in der Klinik und Poliklinik für Nuklearmedizin zu promovieren und die Ausbildung als Medizinphysikexpertin zu absolvieren, sowie für die Möglichkeit an vielzähligen nationalen und internationalen Konferenzen teilzunehmen. Ebenfalls bedanken möchte ich mich für seine eingebrachte umfassende Erfahrung bei der Knochenmarksbildgebung.

Ein großer Dank gilt meinen Kollegen, die mich bei meinen Studien und beim Entwurf der Publikationen unterstützt haben. Im speziellen möchte ich mich bei Prof. Dr. Katia Parodi und Priv. Doz. Dr. Andrea Mairani für die Bereitstellung des FLUKA Codes bedanken, bei Priv. Doz. Dr. Harun Ilhan und Priv. Doz. Dr. Andrei Todica für die Unterstützung bei medizinischen Fragen, bei Prof. Dr. Sibylle Ziegler für ihre eingebrachte Erfahrung bei der Erstellung der Publikationen, sowie bei Dr. Lena Kaiser für Ihre Mithilfe bei der Auswahl der passenden Segmentierungsmöglichkeiten für die Dosimetrie. Des Weiteren möchte ich im Besonderen Sebastian Tattenberg danken, der in seiner Zeit als Bachelorstudent mit unermüdlichem Eifer zu den Vorarbeiten dieser Arbeit beigetragen hat. Ein weiteres großes Dankeschön geht auch an Henrike von Zimmermann und Mirjam Veen, die dabei mitwirkten die SPECT-Bildgebung für die Dosimetrie zu verbessern.

Des Weiteren möchte ich von ganzem Herzen allen Kollegen und Kolleginnen der Klinik und Poliklinik für Nuklearmedizin danken, die mich immer unterstützt haben, mit denen ich viele schöne und bereichernde Momente erlebt habe, die aber auch immer ein offenes Ohr oder aufmunterndes Wort parat hatten, wenn die Dinge mal nicht so ganz wie geplant liefen. Im speziellen möchte ich besonders Georg „Joe“ Stark, Dr. Franz Josef „Uffi“ Gildehaus und Dr. Christian Zach erwähnen, die mir jederzeit mit Rat und Tat bei allen Problemen zur Seite standen, und mit denen ich auch abseits der Arbeit eine sehr lustige Zeit hatte. Ich hoffe sehr, dass noch viele gemeinsame Momente folgen werden! Ebenso möchte ich Dr. Markus Strigl erwähnen, der ebenfalls jederzeit bei Fragen und Problemen ein offenes Ohr hatte.

Ein ganz besonderer Dank geht auch an Dr. Magdalena „Xuxu“ Lindner, die inzwischen ein unverzichtbarer Bestandteil meines Lebens geworden ist, und das nicht nur beim sportlichen Ausgleich im „Gym“ oder beim Karneval feiern. „Xuxu“ hat während meiner Promotion keinerlei Aufwand gescheut, um mir beiseite zu stehen und mich zu unterstützen, sowie um während meiner Schreibphasen für ausrei-

chend Ruhe im Büro zu sorgen. Gleiches gilt für Dr. Luise „Groot“ Fiedler, mit der im Laufe unserer gemeinsamen Zeit als Doktorandinnen eine tiefe Freundschaft und Verbundenheit entstanden ist, die sich manchmal auch - zu Ungunsten von „Xuxu“ - in vehementen Bekundungen im gemeinsamen WhatsApp-Chat äußert. Max „Groschi“ Grosch ist mittlerweile ebenfalls ein fester Bestandteil unserer Truppe geworden, und auch mit Marcel Simmet, Julia Brosch und Larissa Ermoschkin hoffe ich noch auf viele gemeinsame, lustige und schöne Erlebnisse.

Mein größter Dank gilt meiner Familie und ganz besonders Andreas, der in mir nicht nur die Begeisterung für die Dosimetrie und die Nuklearmedizin geweckt und mich in meinem ganzen Tun als Wissenschaftlerin geprägt hat, sondern in dem ich über die Zeit auch meinen Seelenverwandten gefunden habe.